

國立交通大學

物理研究所

博士論文

氫與氯在矽晶面上的交互作用與競爭

**Interactions and Competition of Hydrogen and Chlorine
on a Silicon Surface**



研究生：謝明峰

指導教授：江進福 教授

林登松 教授

Karina Morgenstern

中華民國九十八年六月

氫與氯在矽晶面上的交互作用與競爭

**Interactions and Competition of Hydrogen and Chlorine
on a Silicon Surface**

研究生：謝明峰

Student : Ming-Feng Hsieh

指導教授：江進福

Advisor : Tsin-Fu Jiang

林登松

Deng-Sung Lin

Karina Morgenstern

Karina Morgenstern

國立交通大學

物理研究所

博士論文

A Thesis

Submitted to Institute of Physics

College of Science

National Chiao Tung University

in partial Fulfillment of the Requirements

for the Degree of

Doctor

in

Physics

June 2009

Hsinchu, Taiwan, Republic of China

中華民國九十八年六月

氫與氯在矽晶面上的交互作用與競爭

學生：謝明峰

指導教授：江進福 教授
林登松 教授
Karina Morgenstern

國立交通大學物理研究所博士班

摘 要

本論文在研究氫原子與氯原子在矽(100)表面所發生的各種交互反應，涵蓋課題包括氣體-表面交互作用、吸附原子的擴散以及雙原子分子的化學吸附。實驗方法主要利用變溫掃描穿隧顯微術 (variable-temperature scanning tunneling microscopy, VT-STM)、核心層光電子激發術 (core-level photoemission spectroscopy) 及電腦模擬。STM 提供原子解析影像，可分辨表面上不同的吸附原子，也可看出表面反應發生的位置。核心層光電子激發術則利用核心層電子束縛能的位移，來判斷表面原子鍵結型態以及吸附原子的種類與比例。結合此兩種顯微術及光譜學的技術，便可更進一步解析表面的各種反應。

本論文大致編排如下：第一章簡介研究動機與文獻，概述矽(100)重構後之表面結構與單純的氫或氯飽和吸附後的矽(100)表面，並介紹關聯性函數 (correlation function) 的分析方法。第二章則簡介實驗儀器與操作原理，以及樣品與探針的製備方法。第三章到第五章則分別針對三個主要專題進行研究、分析與討論。

第三章主要探討氣體-表面交互作用：當表面已經飽和吸附原子時，入射的氣體原子會否與表面的吸附原子反應？我們利用氫原子碰撞飽和吸附氯原子後的矽(100)表面，發現當入射的氫原子碰撞到表面的氯原子，會與氯原子形成氯化氫分子脫離矽表面。從核心層光電子光譜可看出，這種反應除了會抽離吸附的氯原子外，尚有其他反應發生，且氫原子最後會取代氯吸附於矽表面。由關連性函數來分析 STM 影像，可發現氯原子被抽離的反應位置並非隨機分佈，隨著氯抽離量越多而反應位置明顯有聚集現象，故此反應並非直接、而是有選擇性發生。此結果可驗證氫原子是以熱原子 (hot atom) 狀態在表面游移，直到適當位置才會與氯原子結合、形成氯化氫分子從矽(100)表面脫附。

第四章討論吸附原子的擴散。當表面飽和吸附兩種原子時，吸附原子會是怎樣的擴散行為？我們經由變溫 STM 觀測不同溫度的矽(100)表面，發現當加熱樣品至一定溫度時，氫原子會與鄰近的氯原子會互換吸附位置。由連續的 STM 影像可看出，氫原子像是在雙原子單體排內進行布朗運動。氫原子會與同一雙原子單體 (intra-dimer) 內之氯原子直接交換、或是與同一雙原子單體排中最鄰近任兩個雙原子單體 (intra-row) 其中之一的氯原子互換。經由實驗結果所計算得的原子交換能量比理論計算來得低，這是因為在直接交換擴散的過程中，可能存在有短暫的氯化氫分子中間態使然。

第五章在探討雙原子分子吸附行為。雙原子分子是以解離吸附或是抽離吸附表面？我們觀察氯化氫分子在不同溫度 (110、300 及 450 K) 的矽(100)表面上所進行的化學吸附。由 STM 實驗結果發現矽(100)表面會完全飽和吸附氯原子與氫原子，且氫原子的吸附覆蓋率比氯原子要多出百分之十。此結果表示氯化氫分子除了解離吸附外，仍會有許多抽離吸附發生，且氫要比氯容易吸附於表面。由 STM 影像顯示氯原子的吸附位置在低溫 110 K 下呈現區域的 2×2 結構，而其有序排列的程度會隨著溫度增高而減弱。透過電腦模擬雙原子分子吸附的結果，驗證了當雙原子分子隨機吸附於表面時，分子解離後的原子與已吸附之原子是存在有交互作用的。

第六章則總結第三章至第五章的實驗結果。本論文之研究應用真實空間及原子解析度的 STM，結合核心層光電子激發術，詳盡地解析矽(100)表面上氫與氯原子的各種化學反應，根據研究提供的許多新數據，本人提出的一些表面科學現象的新見解與新發現。本文之外，附錄收錄氧分子在銀(100)金屬表面之解離吸附的研究報告，此為作者在博士班期間參加 2007 年德國三明治計畫，於德國 Leibniz University of Hannover 參與 Karina Morgenstern 教授的低溫 STM 團隊，進行研究所得到的實驗成果。

Interactions and Competition of Hydrogen and Chlorine on a Silicon Surface

Student: Ming-Feng Hsieh

Adviser: Dr. Tsin-Fu Jiang

Dr. Deng-Sung Lin

Dr. Karina Morgenstern

Institute of Physics

National Chiao Tung University

Abstract

This study investigates interactions and competition of hydrogen (H) and chlorine (Cl) atoms on the Si(100) surface. Several fundamental issues in the field of surface science are examined experimentally, including the gas-surface reaction, the diffusion mechanism of adsorbates and the detailed adsorption processes of diatomic molecules. The measurements were carried out by utilizing a variable-temperature scanning tunneling microscopy (VT-STM), synchrotron radiation core-level photoemission spectroscopy and Monte Carlo simulation. STM images provide images of the surface with atomic-scale resolution, allowing direct viewing of adsorbates and the reaction sites after interactions. The core-level spectra are used to distinguish atoms in different chemical bonding configurations by the chemical shift of binding energies. The combination of these complimentary techniques yields much new and exceptional detailed information and understanding of the interactions of adsorbates on the surface.

This dissertation is organized into six chapters. In Chapter 1, the background and motivations of this research and a review of literatures are introduced. The sample systems and the concept of correlation function are also presented. Chapter 2 describes the sample preparation procedures and the principles and operations of the experimental apparatus. The following three chapters present the three major experiments with detailed results and discussions.

In Chapter 3, I discuss the issue of gas-surface reactions. The main question I ask is that whether the gaseous atoms react with the adsorbate on the surface randomly or not. Specifically, I use an H atomic beam to bombard the Cl-saturated Si(100)-2×1 surface and

examine if any correlation exists between the reaction sites. The results show that the incident H atoms collide on Cl adatoms and form HCl molecules, which are desorbed from the silicon surface. Core-level measurements indicate that some additional reactions occur besides the removal of Cl and that H atoms eventually terminate the Si(100) surface. The correlation function calculated from STM images show that the Cl-extracted sites disperse randomly in the initial phase of the reaction, but form small clusters as more Cl is removed, indicating a correlation between Cl-extracted sites. These results suggest that the hot-atom process may occur during the atom-adatom collision.

Chapter 4 describes a newly-found mechanism of surface diffusion. Specifically, the diffusion behavior of H substitutional sites on the Cl-terminated Si(100) surface was investigated at variant temperatures. STM movies show that each H atom undergoes Brownian motion within a monochloride dimer row. The position of an H substitutional site is exchanged directly with that of an immediate neighboring Cl atom in either the same dimer or in one of the two adjacent dimers in the same row. Accordingly, conceptual direct exchange diffusion in a two-dimensional lattice was experimentally observed. Analysis of STM movies at various temperatures yielded rather low attempt frequencies and energy barriers, leading to the suggestion that the diffusion mechanism involves an intermediate low-energy molecular state.

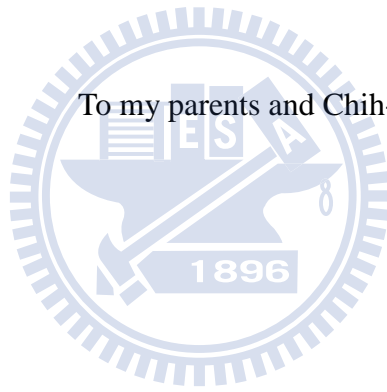
In Chapter 5, I examine the atomic process of the chemisorption of diatomic molecule. Are diatomic molecules chemisorbed on the surface dissociatively or through an abstractive reaction? To answer this question, the Si(100) surface was exposed to gas-phase HCl molecules at various substrate temperatures. Experimental results show that saturation exposure to HCl causes all surface dangling bonds to be terminated by the two fragment H and Cl atoms and that the number of H-termination sites exceeds that of Cl-termination ones by >10 %. This finding suggests that, in addition to the dominant dissociative chemisorption, many abstraction reactions occur. STM images reveal that Cl-termination sites form local 2×2 structure at 110 K and that the degree of ordering is reduced as the substrate temperature increases. Simulation results demonstrate the importance of including dissociative fragment-adsorbates interactions during the random adsorption of diatomic molecules.

Finally, in Chapter 6, research results are summarized and the conclusions are made. The experimental works in this thesis produce much atomic-scale information of several

surface reactions and processes during the coadsorption of two mixed adsorbates on the Si(100) surface. Appended at the end of this dissertation is the study of the dissociative adsorption of oxygen on the Ag(100) surface. This research was conducted when the author was supported by the Sandwich Program supported by Germany and Taiwan in 2007. The experiments were carried out in the low-temperature STM group of Professor Karina Morgenstern in Leibniz University of Hannover.



To my parents and Chih-Yu



Acknowledgement

感謝指導教授林登松老師在我碩、博士生研究期間的教導與照顧，這段日子著實讓我獲益良多，真的非常謝謝老師。感謝共同指導教授江進福老師及學位口試委員簡紋濱教授、林聖迪教授、蘇雲良教授，謝謝各位老師對我論文的指教與建議，讓我的論文能更加充實。感謝實驗室研究夥伴：鎧銘學長及同學世鑫、昌廷、俊緯、仁陽，還有展源、中庭、欣樺、曉穎、靈櫻、宏道、盈秀以及歷屆畢業的學弟妹人黃、祺雄、君黛、閔光、乾庭、依亭、曉婷、靖勛，謝謝你們這些年來的幫助與陪伴，讓我能如此順利、開心地度過研究生生活。

感謝我的父親謝財讓先生、母親謝吳黨女士這些年來無私的關愛與支持，讓我能無後顧之憂、專注在我的實驗研究上。感謝家人培真、之駿、蘆菡的陪伴，與我一同成長。感謝我的妻子至瑜這一路上的鼓勵與陪伴，因為有妳在身邊、生活更加多采多姿。感謝岳父徐文祥先生與岳母陳美蓉這幾年的關懷與照顧。感謝周遭曾經幫助過我的朋友。最後，也要將此獻給我即將出世的小女兒，希望妳永遠健康與快樂。

I would like to thank Professor Karina, Heiko, Fatih, Xin, Jörg, Christopher, Carsten and Ali for all your assistance and guidance during my research in Germany.

Contents

摘 要	i
Abstract	iii
Acknowledgement	vii
List of Figures	xi
Chapter 1 Introduction	1
1.1 Motivation	1
1.2 The Reconstructed Si(100) Surface	5
1.3 Literature Review	10
1.3.1 The Hydrogen-Saturated Si(100) Surface	10
1.3.2 The Chlorine-Saturated Si(100) Surface	12
1.3.3 Chlorine Adsorption on Hydrogen-Terminated Si(100) Surface ..	14
1.3.4 Analysis of Correlation Function	16
Chapter 2 Experimental Apparatus and Methods	20
2.1 The Vacuum System	20
2.2 Scanning Tunneling Microscopy (STM)	23
2.3 Core Level Photoemission	27
2.4 Sample Preparation and Temperature Measurement	29
2.5 Tip Preparation	31
Chapter 3 Correlation of Reaction Sites during the Chlorine Extraction by Hydrogen Atom from Cl/Si(100)-2×1	33
3.1 Introduction	33
3.2 Experiment Details	36
3.3 Results	37
3.3.1 Photoemission results	37
3.3.2 STM results	40

3.4	Discussion.....	44
3.5	Conclusion.....	49
Chapter 4	Possibility of direct exchange diffusion of hydrogen on the Cl/Si(100)-2×1 surface.....	50
4.1	Introduction	50
4.2	Experiment Details	52
4.3	Results and Discussion	54
4.3.1	STM results.....	54
4.3.2	Model of DED mechanism and NEB calculations	59
4.4	Conclusion.....	62
Chapter 5	Repulsive interactions of adsorbed Cl atoms in HCl dissociative adsorption of Si(100)-2×1.....	63
5.1	Introduction	63
5.2	Experiment Details	65
5.3	Results	66
5.3.1	Photoemission results	66
5.3.2	STM results.....	68
5.4	Discussion.....	71
5.4.1	H-abstraction reaction.....	71
5.4.2	Correlation of Cl-occupancy between two adsorption sites	71
5.4.3	Simulations of ordered structure of adsorbates and fragment-adsorbate interactions.....	73
5.5	Conclusion.....	81
Chapter 6	Conclusions	82
Appendix A	Hard repulsive barrier in hot adatom motion after dissociative adsorption of oxygen on Ag(001)	84
A.1	Introduction.....	84

A.2	Experiment Details	86
A.3	Results.....	88
A.4	Discussion.....	94
A.5	Conclusion	96
References		97
Curriculum vitae		103



List of Figures

Figure 1.1 Schematic illustrations of the three types of gas-surface reaction.	2
Figure 1.2 Schematic illustrations of vacancy diffusion.	3
Figure 1.3 Schematic illustrations of direct exchange diffusion (DED).	3
Figure 1.4 Schematic illustrations of three adsorption mechanisms.	4
Figure 1.5 Tetrahedral bond arrangement of diamond structure.	5
Figure 1.6 The oblique view of the ideal Si(100) surface.	7
Figure 1.7 The top view and the side view of the ideal Si(100)- 1×1 surface.....	7
Figure 1.8 The oblique view of the Si (100)-2×1 first layer surface structure.....	8
Figure 1.9 Top view and side view of the Si(100)-2×1 structure	8
Figure 1.10 Step structures on Si(100)-2×1 surface.....	9
Figure 1.11 Model for the 1×1, 2×1, and 3×1 reconstructions on the H-saturated Si(100) surfaces.[7].....	11
Figure 1.12 Schematic diagram of the five geometrically distinguishable configurations of the neighboring pairs of Cl atoms on the Si(100)-2×1 surface.....	13
Figure 1.13 The relative probabilities each geometrically distinctive configuration for Cl atom pairs on the Si(100)-2×1 surface.[9].....	13
Figure 1.14 Three surface species, monohydride dimer H-Si-Si-H, mixed dimer H-Si-Si-Cl and monochloride dimer Cl-Si-Si-Cl, on Si(100) surface with mixed H- and Cl-termination.....	15
Figure 1.15 STM topograph of the Ru(0001) surface after exposure of 1.5 L of NO at room temperature.....	18
Figure 1.16 Hexagonal lattice of cells corresponding to a hcp sites..	18
Figure 1.17 Pair distribution function g vs neighbor site j and Monte Carlo calculation for hard spheres that block the first- and second-neighbor site.....	19
Figure 1.18 Potential of mean force V_{eff} obtained from Fig. 1.14.	19

Figure 2.1	The UHV system of VT-STM.....	21
Figure 2.2	The vacuum system for core-level-photoemission spectroscopy...	22
Figure 2.3	Schematic diagram displays the essential elements of STM.	23
Figure 2.4	Wave function $\Psi(z)$ for an electron with kinetic energy $E = U/2$ penetrating a potential barrier U	24
Figure 2.5	STM images of the Si-Si dimers, imaged with (a) $V_s = -2.2$ V and (b) $V_s = +2.6$ V.....	26
Figure 2.6	Schematic for the energy levels in the core-level photoemission.....	28
Figure 2.7	A chart of the sample current vs. corresponding temperature.....	30
Figure 2.8	The sketch of the etching procedure for the tungsten tip.	32
Figure 3.1	The Cl $2p$ and Si $2p$ core level photoemission spectra (circles) for the Cl-Si(100)- 2×1 surface and the same surface after various apparent H-atom dosages as labeled.....	39
Figure 3.2	Cl coverage calculated from the integrated intensities of the Cl $2p$ core level spectra in Fig. 3.1(a) and from those counting from the STM images.....	41
Figure 3.3	STM images of the Cl/Si(100)- 2×1 surface after 0, 36, and 90 L apparent dosages of H atoms.....	42
Figure 3.4	STM images of the Cl/Si(100)- 2×1 surface after 12 L apparent dosages of H atoms at a sample temperature of 600 K.....	43
Figure 3.5	Distribution of Cl-extracted sites obtained from simulation and STM.....	46
Figure 3.6	The Cl-terminated Cl-Si(100) surface and the unnormalized pair distribution function of Cl-extracted sites vs the neighboring site s obtained from a set of the STM images and the simulation, and the completely random distribution calculation.....	47
Figure 3.7	The ratio of the population density obtained from a set of STM images P_{STM} to that from simulated images P_{Sim} vs site category.	48

Figure 4.1	Ball and stick model of Cl-terminated Si(100) surface. The top-layer Cl atoms are green and a substitute H atom is red. Cl atoms each terminate a dangling bond on the Si surface with dimer reconstruction.	56
Figure 4.2	Four consecutive STM images from movie (20 s/frame).....	57
Figure 4.3	Arrhenius plots for intra-dimer and intra-row H-Cl exchange diffusion.....	58
Figure 4.4	Calculated barriers of three direct exchange diffusion channels as labeled.....	61
Figure 5.1	The Cl 2 <i>p</i> and Si 2 <i>p</i> core level photoemission spectra for the Cl, HCl and H passivated Si(100)-2×1 surface.....	67
Figure 5.2	STM images of Si(100) after saturation dosage of HCl is applied at sample temperature of 110 K, 300 K and 450 K.....	70
Figure 5.3	Unnormalized pair correlation function <i>g'</i> obtained from simulation (a) Program I (squares) and Program II (diamonds) with a zero fragment-adsorbate energy of interaction; (b-d) simulations with fragment-adsorbate energy of interaction and STM images (filled circles) of the samples in Figs. 5.2(a-c).....	77
Figure 5. 4	Simulated distributions of coadsorbed H and Cl sites on Si(100)-2×1 at 110 K and 300 K.....	78
Figure 5.5	Contour representation of standard deviation σ between the simulation and STM result (110 K) as functions of repulsive interacting energies V_{intra} and V_{inter}	79
Figure 5.6	Unnormalized pair correlation function <i>g'</i> obtained by Program I.	80
Figure A.1	STM images of Ag(001) surface with an O coverage of 0.6 % ML.....	89
Figure A.2	STM image of the Ag(001) surface with 1.7 % ML coverage.	91
Figure A.3	Standard deviations σ of nearest-neighbor distances of RP simulation to STM results for different pairing distances.....	93

Chapter 1 Introduction

The surface behavior of materials is pivotal to our lives. One of the most important surfaces is silicon in semiconductor. In modern applications, silicon has been used in metal-oxide-conductor, bipolar transistor, radio frequency integrated circuit, bluetooth, cell phone, multi-junction solar cells and etc. Therefore, to understand the interactions of atoms or molecules on silicon surface is indeed important to chemical industry and semiconductor device processing. Before the invention of scanning tunneling microscopy (STM) in 1982, extensive experimental studies by spectroscopic techniques for this adatom-surface issue have been carried over the half-century. However, these indirect measurements can not reflect real dynamics of adsorbates on surface. In recent years, STM has become an important tool for elucidating the fundamental surface reaction. STM provides a direct view of the surface atomic structure, and past investigations have already yielded a wealth of information. STM and photoemission spectroscopy form a powerful combination of surface probes and are the main methods chosen for the present studies.

1.1 Motivation

The chemisorption and interaction of chlorine- and hydrogen- containing molecule on the Group IV semiconductor surfaces is of both fundamental and great technological importance in semiconductor industry. H adsorption on and desorption from silicon surfaces are of great technological relevance on the etching and passivation of Si surfaces or the growth of Si crystals.[1] The chemisorptions of Cl on silicon surface is also of technological importance since the potential application of chlorine as etching agents in the manufacture of patterned silicon substrates for very-large-scale integrated circuits. HCl gas has been practically applied as a reduced-pressure chemical vapor deposition (CVD) tool in the growth of silicon, germanium, GeSi ally.[2, 3] Besides being important in the growth, HCl chemistry is also important in the etching of silicon.[4, 5] Therefore, understanding the interactions of H and Cl and the chemisorptions of HCl molecule on the Si surface is indeed an important issue to the chemical industry and semiconductor device processing.

For long, there has been much interest about the early stages of the epitaxial growth on Si(100)-2×1 surface. It was not only because of its technological importance, but also due to its relatively simple structure. The properties of the Si(100) surface have been under extensive studies recently, more about its equilibrium structures and surface kinetic processes

has been investigated. It is known that the top-layer atoms of the Si(100) surface dimerize (as two surface atoms binding together to form a dimer) to reduce the number of dangling bonds. Therefore, the interactions of the adsorbates on the surface lead to interesting issues. In our studies, we expose Si(100)-2×1 surface to H, Cl and HCl respectively and focus on the interactions of H and Cl atoms on silicon surface in real time via atomic scale imaging by using VT-STM. The purpose of our study is to obtain a better understanding and further insight in the microscopic dynamical behavior of surface interactions.

The extraction of adsorbates on both metal and semiconductor by impinging atoms has attracted much attention for dynamical understanding of the fundamental gas-surface reaction. Incident A-atom flux would react with B atoms adsorbed on the surface and produce gaseous AB molecule: $A_{(g)} + B_{(ad)} \rightarrow AB_{(g)}$. There are three possible pathways achieving this gas-surface reaction, as shown in Fig. 1.1. These different mechanisms are proposed as the desorption mechanism of AB molecules; (a) Eley-Rideal (direct abstraction) type, (b) Langmuir-Hinshelwood (thermal desorption) type, and (c) Hot Atom type in which A abstracts B before they are in thermal equilibrium with surface. (a) and (c) are nonthermal processes, while (b) is thermal.

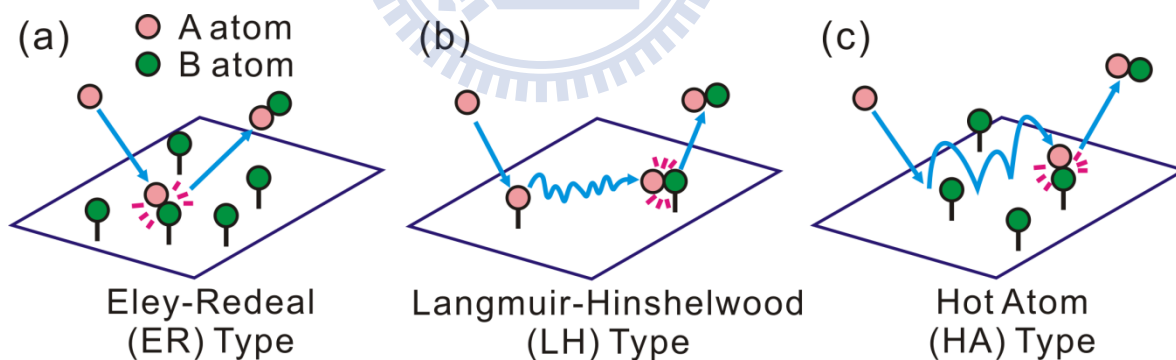


Figure 1.1 Schematic illustrations of the three types of gas-surface reaction. (a) Eley-Rideal type, (b) Langmuir-Hinshelwood type, and (c) Hot Atom type.

The important issue is that the gaseous atoms react with the adsorbate on the surface randomly or not. Specifically, I use an H atomic beam to bombard the Cl-saturated Si(100)-2×1 surface and examine if any correlation exists between the reaction sites.

The diffusion of atoms, molecules and small clusters is one of the fundamental processes that occur on surfaces. A thorough comprehensive understanding of the surface diffusion mechanisms at an atomic level is extremely important to the technological development of surface catalysis and several nanofabrication processes such as thin film growth and etching. An atom can diffuse by exchange of position with that of a neighbor, either directly or by rotation. Such diffusion does not involve defects and commonly requires high energy, so the probability of its occurrence is expected to be very low and most diffusion processes proceed by the exchange of an atom with a neighboring vacancy defect, as shown in Fig. 1.2.

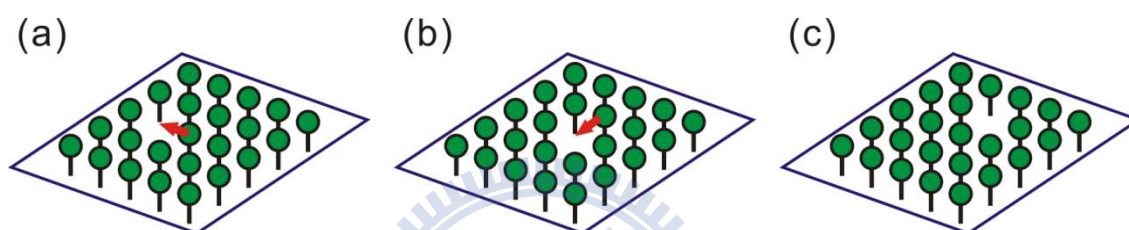


Figure 1.2 Schematic illustrations of vacancy diffusion.

This work describes a newly observed diffusion phenomenon on the Cl-terminated Si(100) surface. STM movies reveal that hydrogen substitutional defects migrate within the top chlorine layer. Hydrogen substitutional sites diffuse at moderate temperature without the participation of vacancies. In the simplest model — direct exchange diffusion (DED), as shown in Fig. 1.3, an H-site and a neighboring Cl-site in the surface lattice swap positions directly. This investigation proposes a model of this diffusion process and performs *ab initio* energy calculations.

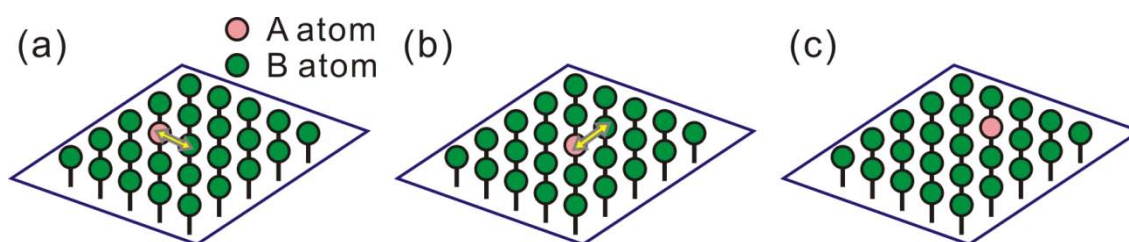


Figure 1.3 Schematic illustrations of direct exchange diffusion (DED). A atom diffuses on the B-atom-saturated surface.

The adsorption mechanisms are commonly classified into three categories: dissociative adsorption, abstractive adsorption or hot atom process, as shown in Fig. 1.4. The dissociative adsorption means the molecular bond broken as two atom-substrate bonds are created. The hot atom process means the adsorbed atoms land at a distance in between. In the other words, two atoms migrate a short distance before they settle down. In an abstractive adsorption, one atom of the molecule is adsorbed on the surface, while the other atom leaves the surface.

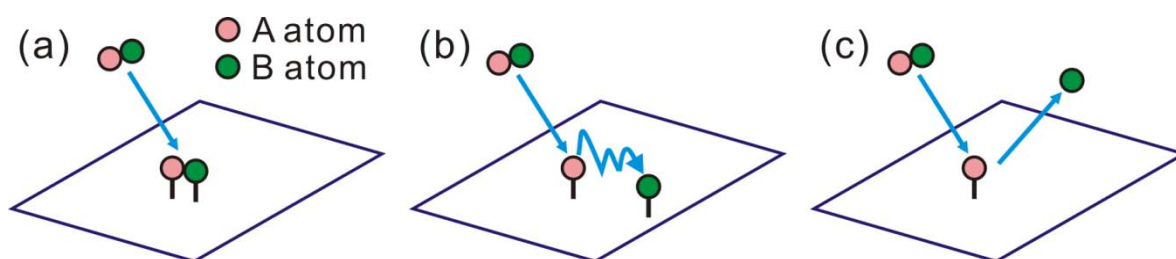


Figure 1.4 Schematic illustrations of three adsorption mechanisms: (a) dissociative, (b) hot atom process, and (c) abstractive adsorption.

In this work, I examine the atomic process of the chemisorption of diatomic molecule, HCl, on Si(100) surface. The main issue is that are HCl molecules chemisorbed on the surface dissociatively or through an abstractive reaction? The Si(100) surface was exposed to gas-phase HCl molecules at various substrate temperatures. Experimental results show that saturation exposure to HCl causes all surface dangling bonds to be terminated by the two fragment H and Cl atoms and that the number of H-termination sites exceeds that of Cl-termination ones. This finding suggests that, in addition to the dominant dissociative chemisorption, many abstraction reactions occur. STM images reveal that Cl-termination sites form local 2×2 structure at 110 K and that the degree of ordering is reduced as the substrate temperature increases. Simulation results also demonstrate the importance of including dissociative fragment-adsorbates interactions during the random adsorption of diatomic molecules

1.2 The Reconstructed Si(100) Surface

Because the Si(100) surface is the substrate used for measurement, its atomic structure of surface will be introduced first as following. Silicon is a group IV element with four electrons in its outer orbit and crystallize in the diamond structure with lattice constant $a = 5.43 \text{ \AA}$, as shown in Fig. 1.5. In a silicon crystal, each silicon atom has four valence bonds bonded to four neighboring silicon atoms in tetrahedral form.

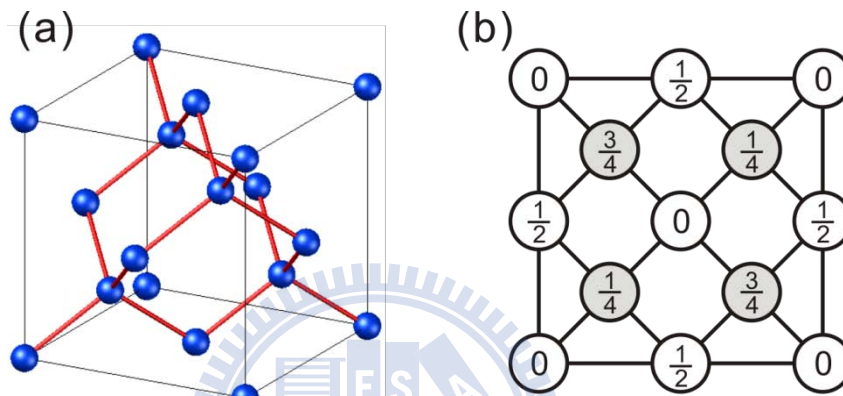


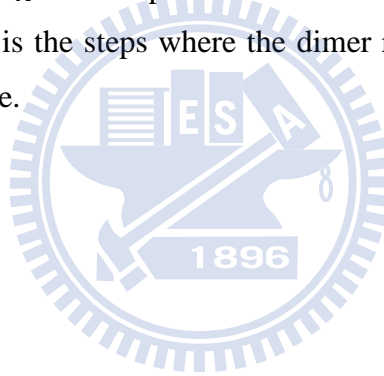
Figure 1.5 (a) Tetrahedral bond arrangement of diamond structure. (b) The down view of diamond structure, the fractions denoted the height of the atoms in units of a cubic edge.

When the Si crystal is cleaved along a different crystal orientation, the new surface will reconstruct into different surface atomic structure. For example, if the crystal is cleaved along the (100) direction, the exposure surfaces will reconstruct into 2×1 structure. If the crystal is cleaved along the direction normal (111) direction, the new surface will reconstruct into 7×7 structure. In this section, we will discuss the detail of the Si(100)- 2×1 structure.

If one cleaves the silicon crystal along the (100) direction, two valence bonds of each Si atom at the exposed surface will be broken and transform into dangling bonds. Therefore, every silicon atom in the surface has two dangling bonds and two valence bonds, as shown in Fig. 1.6. Figure 1.7 displays the top view of this unreconstructed Si(100) surface with 1×1 structure. In this 1×1 structure, the surface energy is high since the density of the dangling bonds is high (two dangling bonds per atoms), and then the 1×1 structure is unstable. To reduce the numbers of the dangling bonds, the first layer atoms in the surface will reconstruct. By this way, the surface energy will be lower and the surface structure will be more stable.

Upon reconstruction, two neighboring atoms form a strong sigma (σ) bond by combined one of the two dangling bonds. The top-layer atoms of the Si(100) surface dimerize (as two surface atoms binding together to form a dimer) to reduce the number of dangling bonds. These bonded pairs of Si atoms are called dimers. The amount of dangling bonds is reduced by 50 %. This establishes two characteristic directions on the surface, along the dimer row and perpendicular to the dimer. The parallel rows of the dimer bonds also reduce the overall surface energy. These remaining dangling bonds can further form a weak pi (π) bond, as shown in Fig. 1.8. Then the 1×1 structure of the surface have transformed into 2×1 structure, as shown in Fig. 1.9, to be a stable surface.

When preparing the Si(100) surface, the step structure formed by the cleavage along the (100) direction, as shown in Fig. 1.10. The height of the step is about 1.36 \AA . The dimer rows on the neighboring terraces are perpendicular, so steps of the terraces divide into two types. S_A is the steps where the dimer rows direction on the upper terrace parallel the step edge. S_B is the steps where the dimer rows direction on the upper terrace perpendicular the step edge.



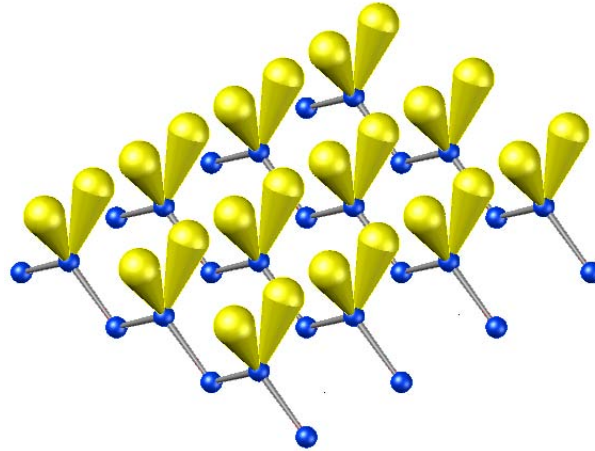


Figure 1.6 The oblique view of the ideal Si(100) surface. Spheres are Si atoms and conoid sticks are dangling bonds. Each silicon atom has two valence bonds and two dangling bonds.

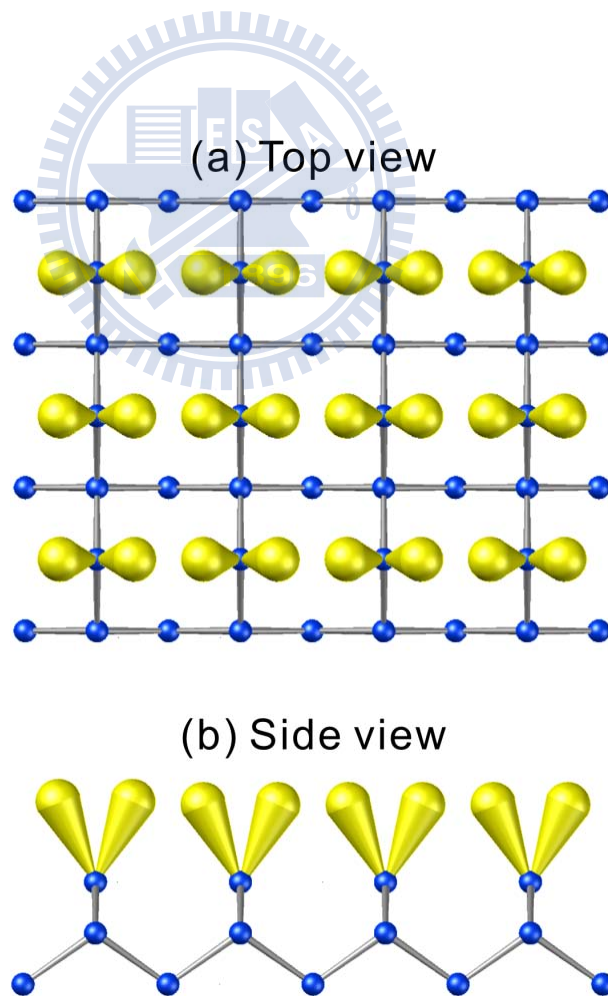


Figure 1.7 (a) The top view and (b) the side view of the ideal Si(100)- 1×1 surface.

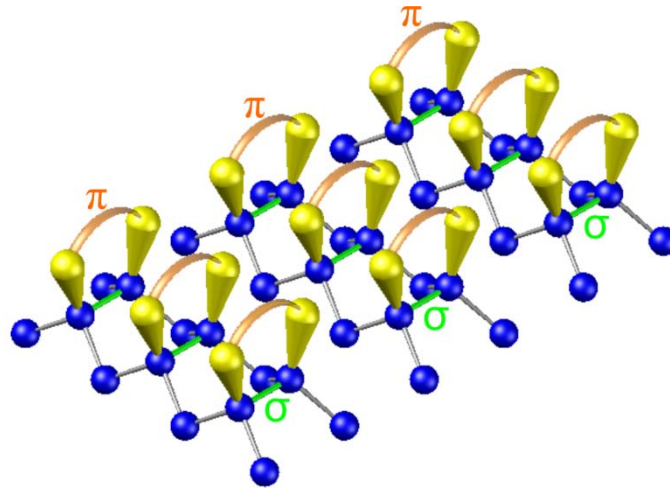


Figure 1.8 The oblique view of the Si (100)-2×1 first layer surface structure.

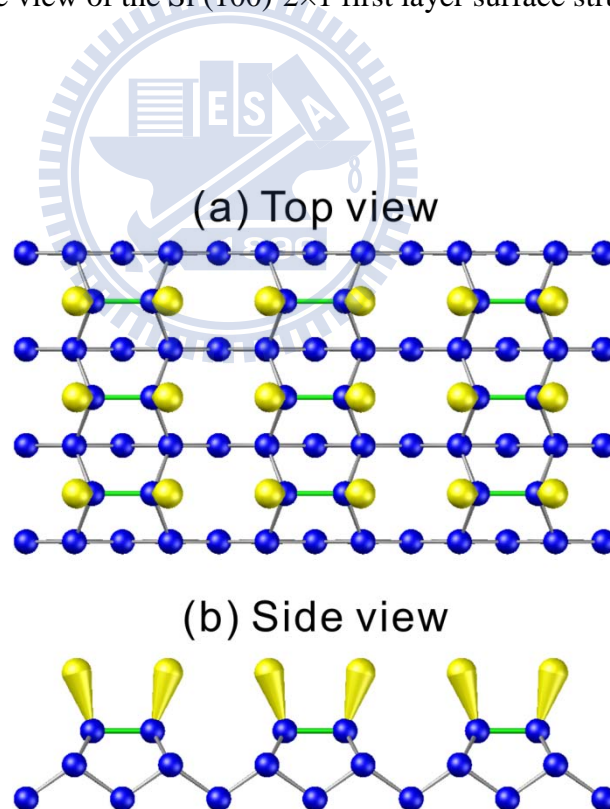


Figure 1.9 Top view (a) and side view (b) of the Si(100)-2×1 structure .

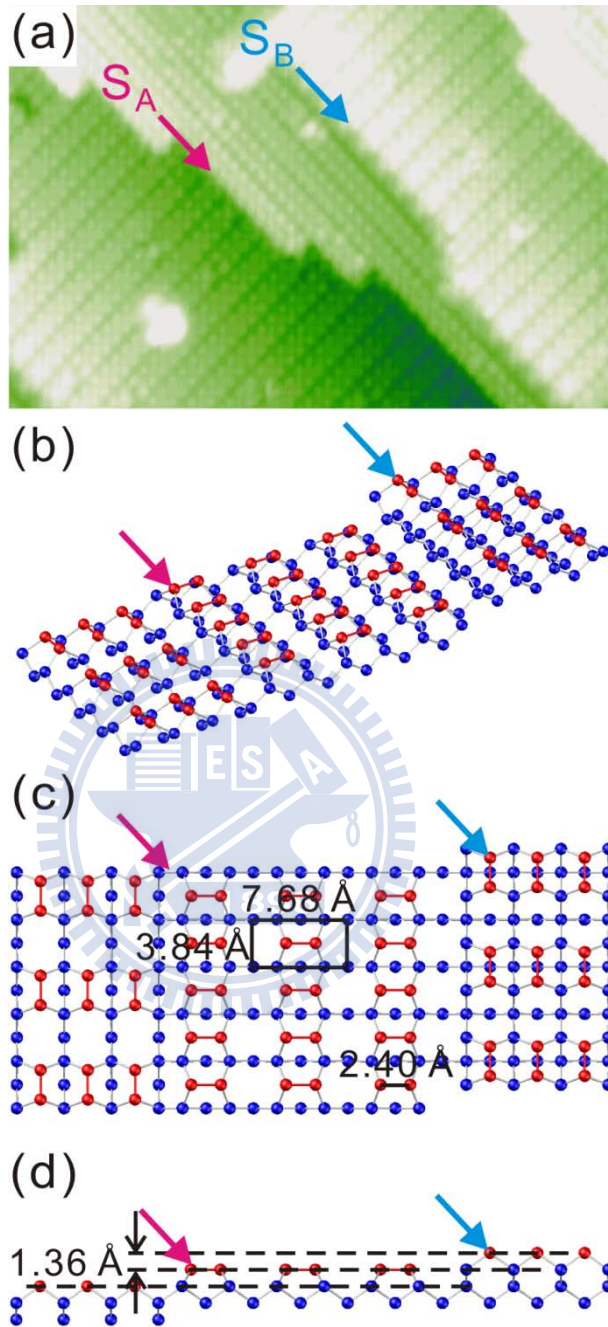


Figure 1.10 Step structures on Si(100)-2 \times 1 surface. (a) STM image of Si(100)-2 \times 1 surface. The size is 15 \times 10 nm² and $V_s = 2$ V. (b) Oblique, (c) top and (d) side views of step structures. S_A is the steps where the dimer rows direction on the upper terrace parallel the step edge. S_B is the steps where the dimer rows direction on the upper terrace perpendicular the step edge.

1.3 Literature Review

1.3.1 The Hydrogen-Saturated Si(100) Surface

Chemical vapor desorption (CVD) of hydrogen on the surface of semiconductors has received much attention because hydrogen can readily react with the surface dangling bonds and forms stable hydrides. In addition, hydrogen is one of the simplest adsorbates to study adsorption, reaction, and desorption processes on the semiconductors and serve as prototype. Therefore, we must understand the H-saturated Si(100) surfaces first. Atomic hydrogen causes a strong interaction with surface states and becomes a powerful tool to assist us with identifying different surface states. Hydrogen is known to induce the reconstructions, 1×1 , 2×1 , and 3×1 structures, on the Si(100) surfaces as shown in Fig. 1.7. [6-8]

Boland *et al.* indicated that, a monohydride phase would form a dimer structure on the surface when exposing H atoms on the Si(100)- 2×1 surface on a typical condition at RT.[6] After further adsorption of hydrogen at RT, the dimer bonds break and form the dihydride phase. The dihydride phase finally reconstructs the 1×1 structure. When exposing H on the Si(100) surface at about 370 K, the monohydride and dihydride phases compose the 3×1 structure. The dihydride and monohydride phases can be easily identified by STM as reported by Boland *et al.* When we expose H on the Si(100) surface at about 650 K, the surface exhibits a 2×1 dimer structure. The hydrogen-adsorption temperature in our work is about 600 K, in other words, the surface should mainly exhibit a monohydride phase as introduced.

Figure 1.7 shows a model for the three reconstructions 1×1 , 2×1 , and 3×1 structures on the H-saturated Si(100) surfaces.[6, 7] Irradiation of atomic H beam on the initially monohydride surface leads to the formation of dihydrides and repulsive stress between them. At $T_s < 310$ K, inhomogeneous 1×1 structure is formed, and reconfiguration to dimers with molecular hydrogen emission does not proceed. At 360 K $< T_s < 480$ K, the surface has 3×1 structure with mono-hydride and dihydride next to each other, and the desorption of hydrogen molecules is less efficient. At $T_s > 480$ K, reconfiguration to monohydride dimers proceed via emitting hydrogen molecules. The STM images in Fig. 1.11 are obtained from J. J. Boland, 1990.[6] In our study, we focus only on the hydrogen-terminated Si(100)- 2×1 surface.

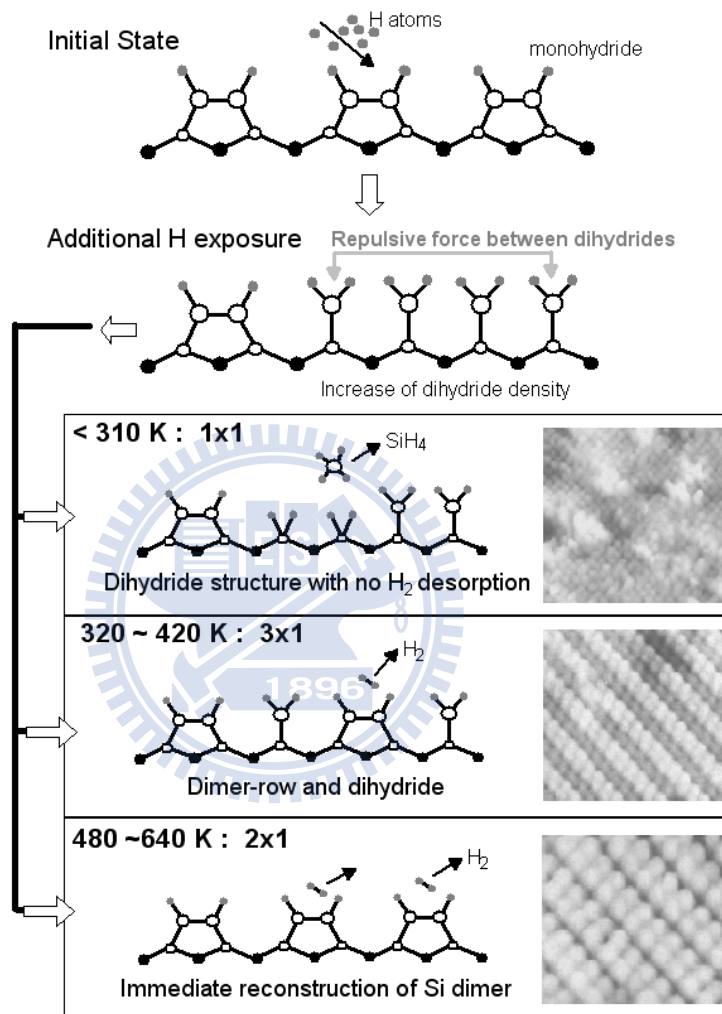


Figure 1.11 Model for the 1×1 , 2×1 , and 3×1 reconstructions on the H-saturated Si(100) surfaces.[7]

1.3.2 The Chlorine-Saturated Si(100) Surface

The main properties of the Si(100)-2×1 surface obtained from STM has been widely studied. It is known that the top layer atoms of the Si(100) surface reconstruct to form parallel rows of dimers, which establish two well-differentiated directions, in parallel and perpendicular to these rows. By exposing Si(100)-2×1 surface to chlorine molecules at room temperature, chlorine atoms tends to saturate at the dangling bond sites of the surface. There are five geometrically distinguishable configurations of the arrangement of neighboring pairs of Cl atoms on the Si surface,[9, 10] as shown in Fig. 1.12. Liu *et al.* calculated the total energy of different adsorption configurations.[10] The energy ordering is Type I < Type IIa < Type IIIa < Type IIIb < Type IIb, as shown in Fig. 1.12. Type I is the most stable because it only breaks one weak π bond between the dimer silicon atoms, while the other configurations break two. Figure 1.13 shows the population of geometrically configurations for Cl atom pairs on the Si(100)-2×1 surface.[9] The most probable like arrangement is the chemisorption of two Cl atoms on the Si dimer sites in adjacent rows, as shown in Fig. 1.13, labeled type III a + III b. The probability of this configuration is 0.52. For type II a and II b, where Cl atoms bonded to the adjacent dimers in the same dimer row, as shown in the same figure, the probability is 0.33. For two Cl atoms to be present on the same Si dimer is the least likely with a probability of 0.15, as labeled type I.

If we increase the exposure of the chlorine gas, the density of the fully Cl-terminated dimers increases. In the end, all the dimers with dangling bonds on the surface will be terminated with chlorine atoms. The adsorption of Cl molecules does not disrupt the sigma bonds, but breaks the weak pi bonds existed o the clean Si(100)-2×1 surface. Therefore, each dimer has terminated with two Cl atoms, as one Cl per Si, in the Cl-saturated Si(100)-2×1 surface, now covered with one monolayer of chlorine atoms.

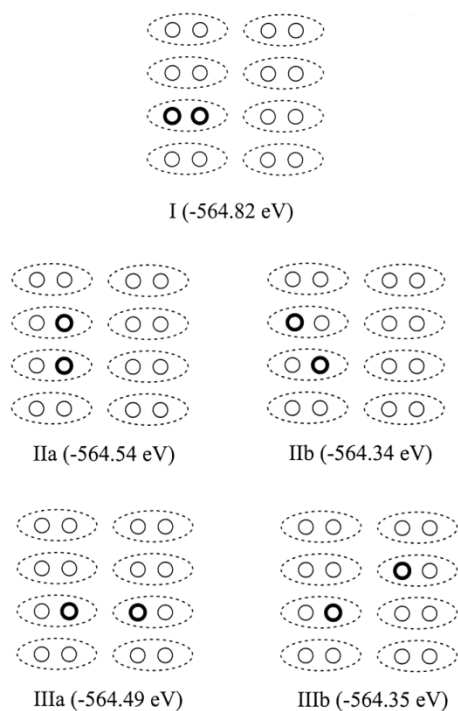


Figure 1.12 Schematic diagram of the five geometrically distinguishable configurations of the neighboring pairs of Cl atoms on the Si(100)-2×1 surface. The broken line encircle a Si-Si dimer, while the dark circles indicate the adsorption sites of Cl atoms, which could be on the same dimer as in Type I, or across the same dimer row as in Type IIa and IIb, or across two dimer rows as in Type IIIa and IIIb. Each type of structure is put in a 4×4 surface lattice, which is the lattice used in our calculation. The number in parentheses is the calculated total energy for each structure.[10]

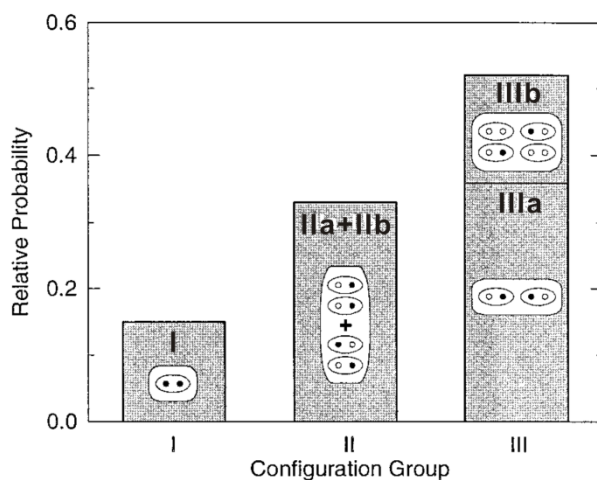


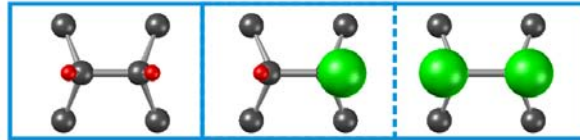
Figure 1.13 The relative probabilities each geometrically distinctive configuration for Cl atom pairs on the Si(100)-2×1 surface.[9]

1.3.3 Chlorine Adsorption on Hydrogen-Terminated Si(100) Surface

The clean Si(100) surface consists of rows of dimers, where the two dangling bonds from the two Si atoms in a dimer form a weak π bond. When H (or Cl) atoms saturate a clean Si(100) surface, the surface will preserve the basic 2×1 dimer structure without buckling.[6, 9] The building blocks of the Si(100)- 2×1 :H surface and the Si(100)- 2×1 :Cl surface are a monohydride dimer (H-Si-Si-H) and a monochloride dimer (Cl-Si-Si-Cl), respectively, as shown in Fig. 1.14(a). Accordingly, the co-existence of H and Cl on the clean Si(100) surface, following either co-adsorption or sequential adsorption of the two atoms, can yield mixed H-Si-Si-Cl surface species, in addition to H-Si-Si-H and Cl-Si-Si-Cl.

Upon co-adsorption of both H and Cl atoms on Si(100), Cl-terminated sites (Cl-Si species or Cl-sites) appear noticeably brighter than H-terminated sites (H-sites) in both filled and empty-state STM images, as shown in Fig. 1.14(b). In Fig. 1.14(b), the 0.18 ML Cl-sites were produced by exposing to Cl_2 a mostly H-terminated Si(100) surface, in which a portion of dangling bonds were created by mild thermal annealing of the Si(100)- 2×1 :H sample at ~ 715 K for 50 s.[11, 12] The adsorption of Cl_2 on an isolated dangling bond or a dangling bond pair of Si(100) has been demonstrated to be mostly abstractive and to be able to cause chain reactions:[11, 13] the Si dangling bond abstracts one atom of the incident Cl_2 molecule while the complementary Cl atom is scattered away from the initial abstraction site. The complementary fragment Cl atom may be captured by a second dangling bond and adsorbed there, or may react with a nearby H atom to form HCl that is scattered away from the surface, leaving a new dangling bond for subsequent Cl_2 adsorption. The complex adsorption processes of Cl_2 produces large amounts of mixed Cl-Si-Si-H species even though brief thermal annealing yields more paired dangling bonds (-Si-Si-) than unpaired dangling bonds (-Si-Si-H).

(a) Top View



Side View

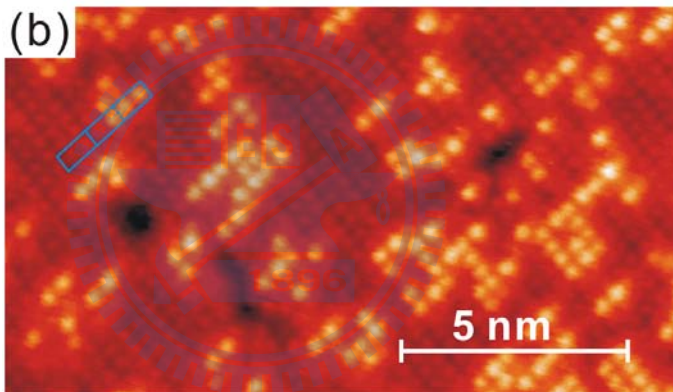
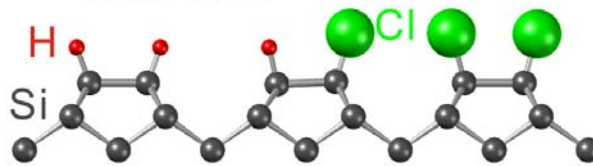


Figure 1.14 (a) Three surface species, monohydride dimer H-Si-Si-H, mixed dimer H-Si-Si-Cl and monochloride dimer Cl-Si-Si-Cl, on Si(100) surface with mixed H- and Cl-termination. The smallest (red) and largest (green) spheres in the topmost layer are H and Cl atoms, respectively. (b) $15.4 \times 12 \text{ nm}^2$ STM image of the mostly H-terminated Si(100)- 2×1 surface with 0.18 ML Cl termination (bright protrusions), captured at a sample bias $V_s = 2.28 \text{ V}$ and tunneling current $I_t = 0.21 \text{ nA}$. The three neighboring rectangles enclose the three surface species described in (a). The size of a 1×1 unit cell in the image is $3.84 \times 3.84 \text{ \AA}^2$.

1.3.4 Analysis of Correlation Function

Interactions between adsorbed particles on solid surfaces play a principal role in surface science. Along with the adsorbate-substrate potential they determine the formation of surface phases that is of ordered structures of atoms or molecules, and the mechanisms and activation energies of chemical reactions between adsorbed particles. Knowledge of these interactions is therefore of fundamental importance for the understanding of catalytic reactions. For a particular system the relative importance of the different contributions is mostly unknown. The main problem is that for the majority of systems no quantitative experimental data are available.

Trost *et al.* presented an investigation based on a STM determination of interactions between adparticles.[14] The method is based on an evaluation of the pair distribution function $g(j)$ (j is the j th-nearest-neighbor site) from STM images, which provides the potential of mean force $V_{eff}(j)$. Trost *et al.* report that N atoms adsorbed on Ru(0001) surface and conclude that there are repulsive interactions at nearest- and next-nearest-neighbor sites and an attraction at third-nearestneighbor sites, and they also give quantitative estimates about the underlying energies.

Figure 1.15 shows the Ru(0001) surface after exposure to 1.5 L of NO. Two different species can be identified by the imaging depth: The deeper features (black) are O atoms, the others (gray) are N atoms. Additionally, oxygen is known to form 2×2 islands, in contrast to nitrogen. This 2×2 structure is seen in Fig. 1.15 as an ordered, hexagonal pattern, however, with some nitrogen atoms incorporated. Between the 2×2 covered areas additional, individual nitrogen atoms are located. Since the positions of the dark, i.e., oxygen, atoms in the 2×2 areas define the lattice of hcp sites, the positions of the N atoms are obtained by extrapolating the lattice to the area between the 2×2 patches. This is demonstrated in Fig. 1.15 by the point lattice. It turns out that all of the N atoms, those within the islands and the single ones, occupy the same sites as the O atoms. The N adsorption site is thus identified as the hcp site. This conclusion is in agreement with the results of a recent LEED analysis and density-functional calculations. This justifies the lattice-gas model underlying the following analysis.

The hexagonal lattice of cells on Ru(0001) is illustrated in Fig. 1.16, where each cell represents a hcp site around an atom located in the center. For such a two-dimensional

lattice-gas system the pair distribution function at the j th-nearest-neighbor site can be defined as

$$g(j) = \frac{1}{N \cdot \Theta} \sum_{i=1}^N \frac{n_i(j)}{m(j)} \dots\dots\dots(1.1)$$

where $n_i(j)$ is the number of j th-nearest-neighbor particles around the i th particle, Θ the coverage, and $m(j)$ the number of j th-neighbor sites. The normalization, by division of Θ , makes $g(j)$ unity when j approach infinity. The meaning of the pair distribution function is that deviations from a random particle distribution manifest themselves in deviations from $g = 1$. From the definition Eq. (1.1) the pair distribution function at a certain site j can be interpreted as the ratio of two probabilities, the probability to find a particle at that site divided by the average occupation probability. At equilibrium a ratio of occupation probabilities should be Boltzmann distributed, viz.,

$$g(j) = e^{-V_{eff}(j)/kT} \dots\dots\dots(1.2)$$

The effective interaction potential $V_{eff}(j)$ is the so-called *potential of mean force*, which describes the interaction within an ensemble of particles. Crucial for the validity of Eq. (1.2) is that the system is in thermodynamic equilibrium.

After normalization according to Eq. (1.1) this yields the pair distribution function $g(j)$. The result for 1344 atoms, corresponding to coverage of $\Theta = 0.095$, is reproduced in Fig. 1.17 as black dots. The deviations from $g(j) = 1$ corresponding to a random distribution. Figure 1.18 shows the potential of mean force that was evaluated using Eq. (1.2). Because of the complete absence of $j = 1$ separations (the nonzero value in Fig. 1.17 is caused by the experimental error) no value for $V_{eff}(1)$ can be given in Fig. 1.18. From an STM image that contains 1344 N atoms but not a single nearest-neighbor distance, it is estimated that $g(1) < 2.5 \times 10^{-4}$ and hence $V_{eff}(1) > 0.2$ eV. At the secondneighbor site the potential is still repulsive, with $V_{eff}(2) = +13$ meV. Attractions are observed at the thirdand sixth-neighbor sites, with $V_{eff}(3) = -18$ meV and $V_{eff}(6) = -10$ meV, respectively. This corresponds to the formation of local 2×2 order, as visible in Fig. 1.15. The fourth- and fifth-neighbor sites are occupied with nearly statistical probability.

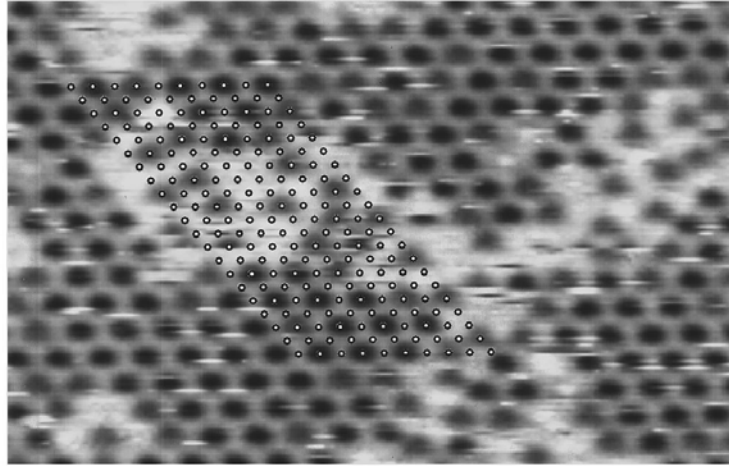


Figure 1.15 STM topograph of the Ru(0001) surface after exposure of 1.5 L of NO at room temperature. O atoms are imaged deeper (black) than N atoms (gray). Small dots indicate the lattice of hcp sites, using the O atoms in the 2×2 areas as fix points. Tunneling parameters are $89 \times 80 \text{ \AA}^2$, -0.3 V , and 33 nA . [14]

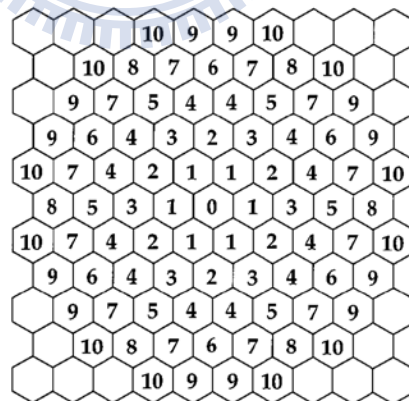
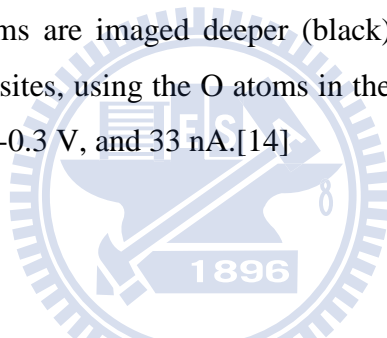


Figure 1.16 Hexagonal lattice of cells corresponding to a hcp sites. Numbers mark the index j of the distance between an atom in the center and an atom in the respective cell. [14]

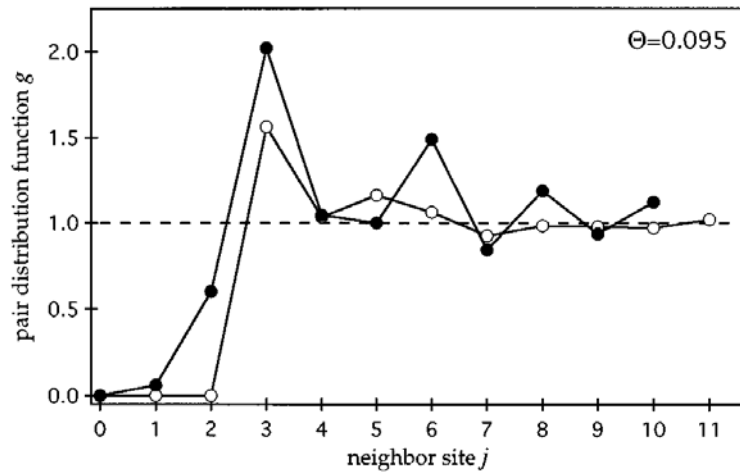


Figure 1.17 Pair distribution function g vs neighbor site j (black dots) and Monte Carlo calculation for hard spheres that block the first- and second-neighbor site (white dots).[14]

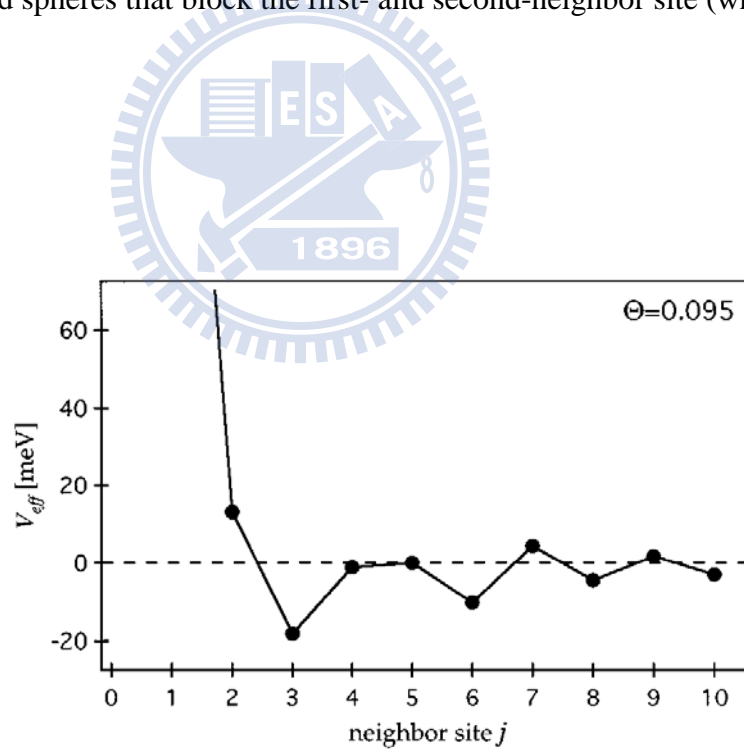


Figure 1.18 Potential of mean force V_{eff} obtained from Fig. 1.14. Note the repulsion up to the second-neighbor site and the attractions at the third- and sixth-neighbor sites.[14]

Chapter 2 Experimental Apparatus and Methods

2.1 The Vacuum System

The STM experiment was conducted in an ultrahigh-vacuum (UHV) system. The main chamber is equipped with a variable-temperature scanning tunneling microscopy (VT-STM, Omicron), a manipulator, a pumping system, gas sources including H₂, Cl₂ and HCl, as shown in Fig. 2.1. The pumping system is consisting of a dry pump, a turbo pump, a titanium sublimation pump (TSP), and an ion pump. The base pressure of this vacuum system is 1×10^{-10} torr.

The dry pump is used first to lower pressure in the vacuum chamber to $\sim 10^{-3}$ torr. Then the turbo pump automatically starts to lower the pressure to the 10^{-6} torr range. At this lower pressure, the ion pump turns on. As the pressure drops to $\sim 10^{-7}$, we start to bake the chamber at about 120 °C for over 24 hours. After the chamber cools down to RT, we gain the ultra-high vacuum about 1×10^{-10} torr.

The core-level-photoemission experiment is carried out at the National Synchrotron Radiation Research Center (NSRRC) located in the Hsin-chu Science-based Industrial Park, Taiwan. Light from the 1.5-GeV storage ring was dispersed by a Dragon-type 6-m wide range spherical grating monochromator (SGM). This beamline has two energy range, *i.e.* 10-175 eV from a low energy branch and 120-1500 eV from a high energy branch. In our experiment, we use the high energy branch since the main photon energies used are 140, and 240 eV. All the adsorptions of H, Cl and HCl were prepared *in situ* in the ultra-high vacuum system, as shown in Fig. 2.2. In the photoemission experiment, the procedure to obtain the ultra-high vacuum is the same as the STM experiment.

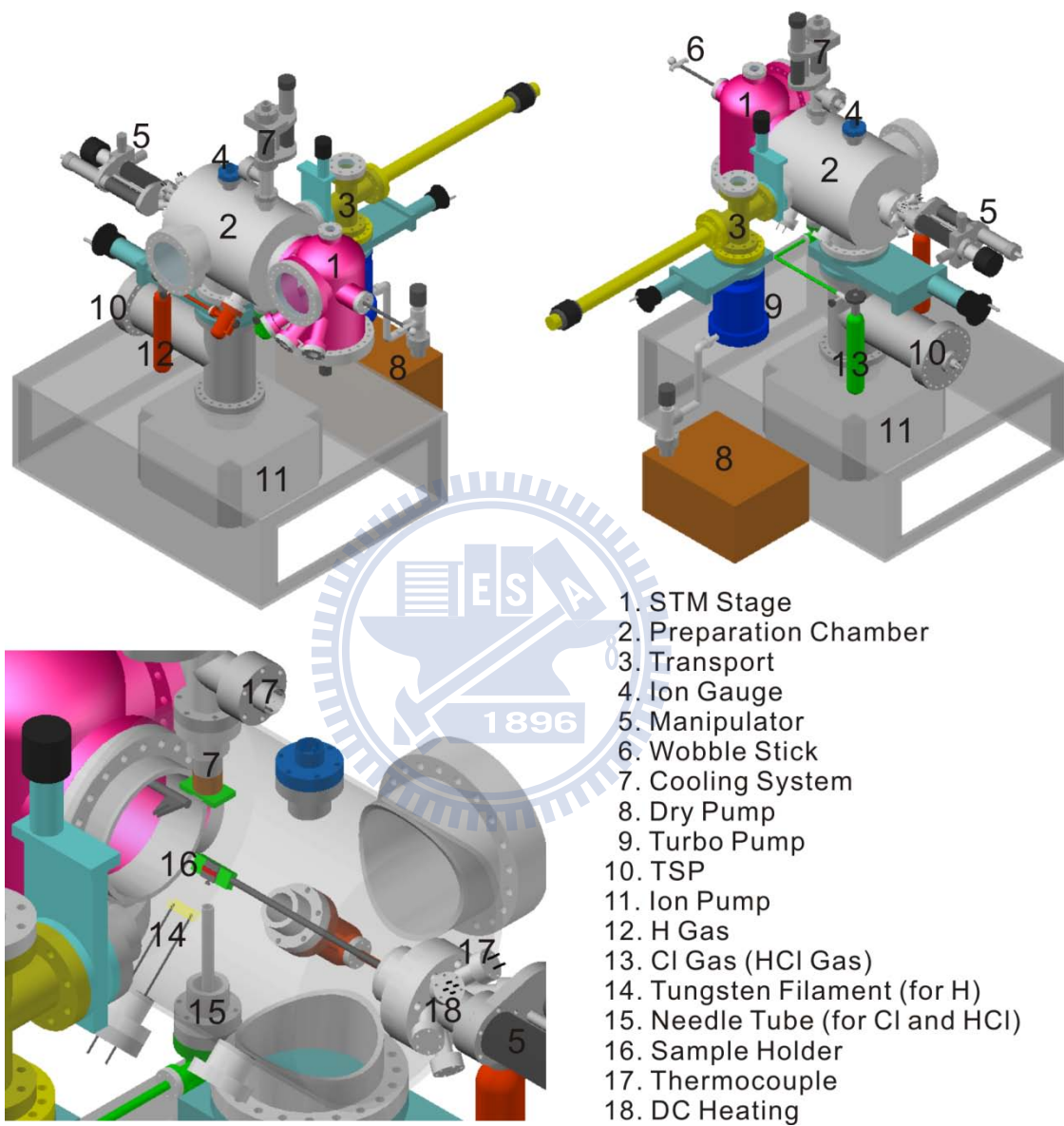


Figure 2.1 The UHV system of VT-STM.

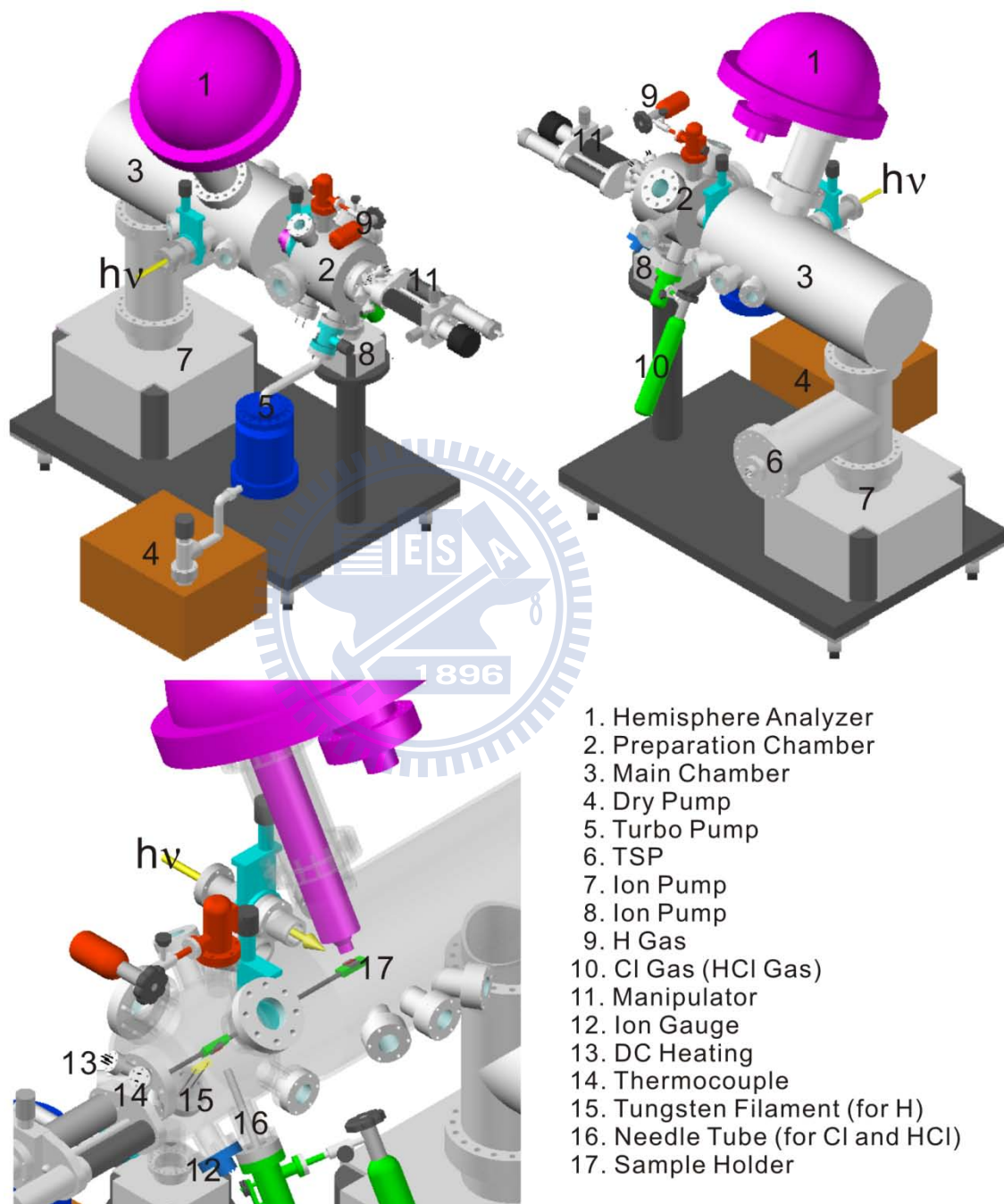


Figure 2.2 The vacuum system for core-level-photoemission spectroscopy.

2.2 Scanning Tunneling Microscopy (STM)

Since Binnig *et al.* invented the Scanning Tunneling Microscopy (STM) and obtain the atomic resolution in 1982, the STM technique has been widely used in various fields, like condensed-matter physics, chemical, biology physics and etc. Especially, after resolving the structure of the Si(111)-7×7 in real space using STM, this instrument has proved to be an extremely powerful tool.

Figure 2.3. displays its essential elements. A probe tip, usually made of tungsten (W) or Pt-Ir alloy, is attached to a piezoelectric scanner. Using the coarse positioner and the z piezo, the tip and the sample are brought to within a few angstroms of each other. A bias voltage, applied between the tip and the sample, causes an electrical current to flow. This is a quantum-mechanical phenomenon, tunneling, which is the principle theory of the scanning tunneling microscopy. To achieve atomic resolution, vibration isolation is essential. A commonly used vibration isolation system consists of a set of suspension springs and a damping mechanism.

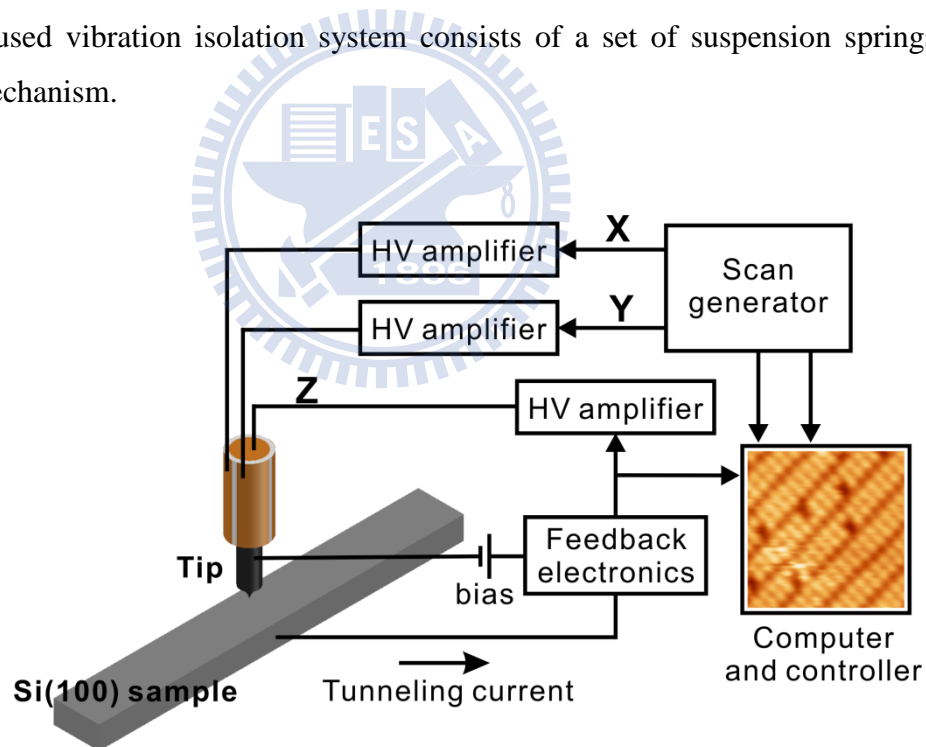


Figure 2.3 Schematic diagram displays the essential elements of STM.

The operating principle of the STM is based on the quantum mechanical phenomenon of tunneling. In this section, we discuss the concept of the tunneling through one-dimensional model. First we consider the classical situation. In the classical mechanics, an electron with energy E moving in a potential $U(z)$ is described by

$$\frac{p_z^2}{2m} + U(z) = E \quad \dots\dots\dots(2.1)$$

In the regions where $E > U(z)$, the electron has a nonzero momentum P_z . It means that the electron has the ability to be in those regions. Otherwise, in the regions where $E < U(z)$, the electron can not penetrate into those regions. In other words, the electron with energy E has no possibility to be find in the regions with $U(z) > E$. Now we discuss the quantum effect. In the quantum mechanics, the motion of the same electron is described by the Schrödinger's equation,

$$-\frac{\hbar^2}{2m} \frac{d^2}{dz^2} \Psi(z) + U(z)\Psi(z) = E\Psi(z) \quad \dots\dots\dots(2.2)$$

$\Psi(z)$ is the wavefunction of the electron.

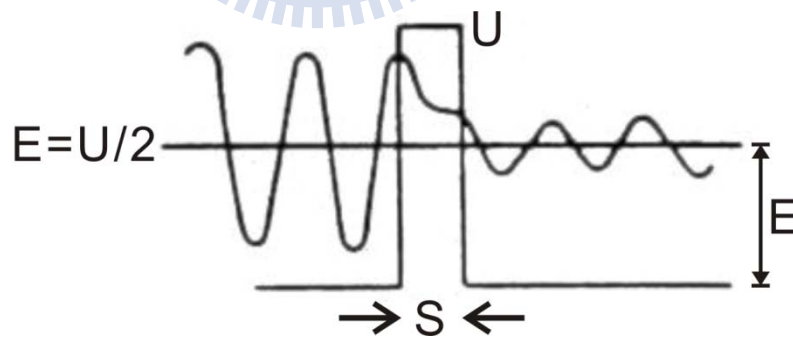


Figure 2.4 Wave function $\Psi(z)$ for an electron with kinetic energy $E = U/2$ penetrating a potential barrier U .

For an electron with $E = U/2$ incident on a square barrier from the left, as shown in Fig. 2.4. The Schrödinger's equation of this electron

$$-\frac{\hbar^2}{2m} \frac{d^2}{dz^2} \Psi(z) + \frac{1}{2} U \Psi(z) = 0 \dots\dots\dots(2.3)$$

has the solution:

$$\begin{aligned} \Psi(z) &= Ae^{ikz} + Be^{-ikz} \dots\dots\dots(z < 0) \\ \Psi(z) &= Ce^{Kz} + De^{-Kz} \dots\dots\dots(0 < z < s) \\ \Psi(z) &= Fe^{ikz} \dots\dots\dots(z > s) \end{aligned} \dots\dots\dots(2.4)$$

where $k = \frac{(2mU)^{1/2}}{\hbar}$; $K = \frac{(mU)^{1/2}}{\hbar}$

Eq. (2.4) can be solved for the transmission coefficient $T = |F/A|^2$ by matching of the boundary conditions on Ψ and $d\Psi/dz$ at $x = 0$ and $x = s$. That is

$$T = \frac{1}{1 + \left(\frac{k^2 + K^2}{2Kk}\right)^2 \sinh^2 Ks} \dots\dots\dots(2.5)$$

Because a barrier of width s that is much thicker than the wave function decay length of $1/K$, $Ks \gg 1$, the transmission coefficient can be approximated as

$$T \approx \frac{16k^2 K^2}{(k^2 + K^2)} e^{-2ks} \dots\dots\dots(2.6)$$

It is this exponential dependence of the transmission coefficient T on the barrier width s that enables atomic resolution images in tunneling microscopy. It provides a sufficient signal, the tunneling current, for atomic scale feedback control of the gap width s along the z direction.

Interestingly, use of 1° miscut Si(100) single-crystal wafers allows for highly rotationally oriented samples in which all the Si-Si dimers are pointed in the same direction, yielding anisotropic surfaces on a centimeter length scale. The high ordering of the dimers, showing both the filled and empty states, is shown in the stunning STM images of Fig. 2.5; the filled and empty states were imaged by changing the tip bias.

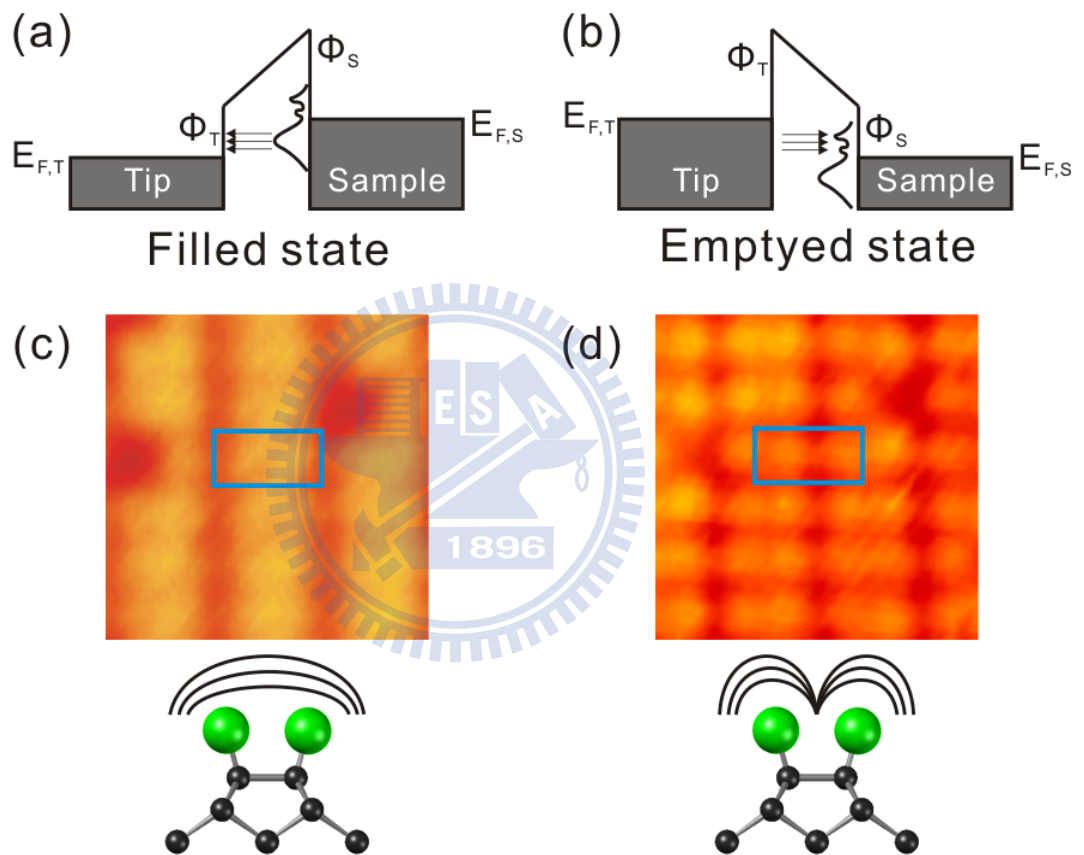


Figure 2.5 STM images of the Si-Si dimers, imaged with (a) $V_s = -2.2$ V and (b) $V_s = +2.6$ V. The filled and empty states of these highly ordered dimmers can be probed by biasing the surface in the opposite directions. The dimensions of the figure are $2.3 \text{ nm} \times 2.3 \text{ nm}$.

2.3 Core Level Photoemission

The core level photoemission experiment is to collect the photoelectrons excited from core level near nucleus. Photoelectrons were collected and analyzed by a large hemispherical analyzer. By measuring the variation of the photoelectron kinetic energy, we can observe the species of the passivated atoms and chemical bonding etc.

The photoelectrons are excited from inner energy levels (binding energy >20 eV), of which the orbital radius is less than 0.3 \AA . In solid state, the core level wave functions are independent such that the binding energies of the atoms in bulk are the same. However, the potential of the atoms near surface becomes different because the local atomic environment changes. The potential difference of surface atoms results in chemical shift of the core level binding energy.

We can explain the relationship between the kinetic energy (KE) of excited photoelectrons and energy of incident photons by the energy conservation law as Eq. 2.7. The relation of the energies is shown in Fig. 2.6.

$$KE = hv - B - \Phi \quad \dots\dots\dots(2.7)$$

KE : kinetic energy of excited photoelectron

hv: photon energy

B: binding energy

Φ : work function.

In this formula, the binding energy B is the difference between the core level and Fermi level. The work function Φ is the difference between the Fermi level and vacuum level. This formula is based on the ideal situations; however, we have to consider other factors like secondary electrons and escape depth etc. The escape depth of the excited photoelectron is dependent on the kinetic energy, in other word, the higher kinetic energy, the larger escape depth. Therefore, the escape depth of photoelectrons of kinetic energy $20 \text{ eV} \sim 110 \text{ eV}$ is less than 10 \AA . The spectra obtained by analyzing these photoelectrons provide us the message of the surface.

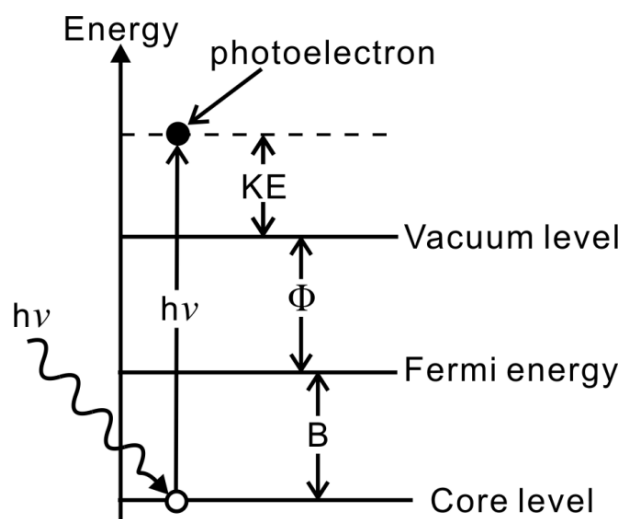


Figure 2.6 Schematic for the energy levels in the core-level photoemission.

After electrons excited from core level, left holes will be occupied by other electrons. The reaction of occupation can occur in two processes. First, the electrons in the higher energy level occupy the left holes and release the photons of energy equivalent to the difference between two levels. Next, the electrons in the higher energy level occupy the electron holes and release energy. The released energy is not carried by photons but directly excites electrons to leave surface. The excited electrons in the second process are so-called Auger electrons. The Si $2p$ and Ge $3d$ core level photoemission is mainly contributed from Auger electrons.

The lifetime of the electron holes yields Lorentzian broadening. The other factor to result in broadening spectra is the resolution of the analyzer, which produces a Gaussian width of the spectra. The convolution of the Lorentzian width and Gaussian width yields a Voigt lineshape for the spectra.

2.4 Sample Preparation and Temperature Measurement

Various sample treatments will be conducted depending upon the type of the sample that will be required for the experiment. The Si(100) samples used in our experiment were sliced up into pieces of size $1 \times 8 \text{ mm}^2$ from a antimony (Sb) doped wafers with a dopant concentration of approximately $1.5 \times 10^{15} \text{ cm}^{-3}$. The misalignment of the wafer is about 0.1 degrees. Before loading the samples into the vacuum chamber, we blow off the dust on the surface of the samples with pure nitrogen gas so we don't have unwanted particles on the surface of the samples which could affect our measurements. After loading the samples to the UHV chamber, the samples are then being degassed for over 12 hours at $\sim 900 \text{ K}$ using a small AC current. After degassing, the sample was flashed at $\sim 1450 \text{ K}$ for a few seconds in order to remove the oxide layer on the surface and form a dimerized clean Si(100)- 2×1 surface.

The substrate was heated by passing a controlled dc current directly through the sample. The sample temperature that corresponds to each current was obtained using an infrared optical pyrometer and calibrated by gluing a tiny type-K thermocouple to the center of the sample following the final last STM run, as shown in Fig. 2.7. The uncertainty in the temperature measurement was estimated to be approximately $\pm 5 \text{ K}$.

After the direct heating, chlorine (or hydrogen chloride) molecules were introduced through a leak valve and a stainless steel tube to the sample surface at room temperature to form the desired Cl-terminated Si(100)- 2×1 structure. A hot tungsten-spiral filament was used to produce atomic hydrogen. The filament was $\sim 5 \text{ cm}$ away from the Si(100) substrate and heated to $\sim 1800 \text{ K}$ when the chamber was backfilled for a period of time, about 12 min, with H_2 to a pressure P of about 1×10^{-7} torr. From the geometry of the filament and the samples, it was estimated that the incident angles of the H atoms was less than $\sim 25^\circ$ from the normal. The apparent H_2 exposure is presumably proportional to the actual dosage of hydrogen atoms on the surfaces.

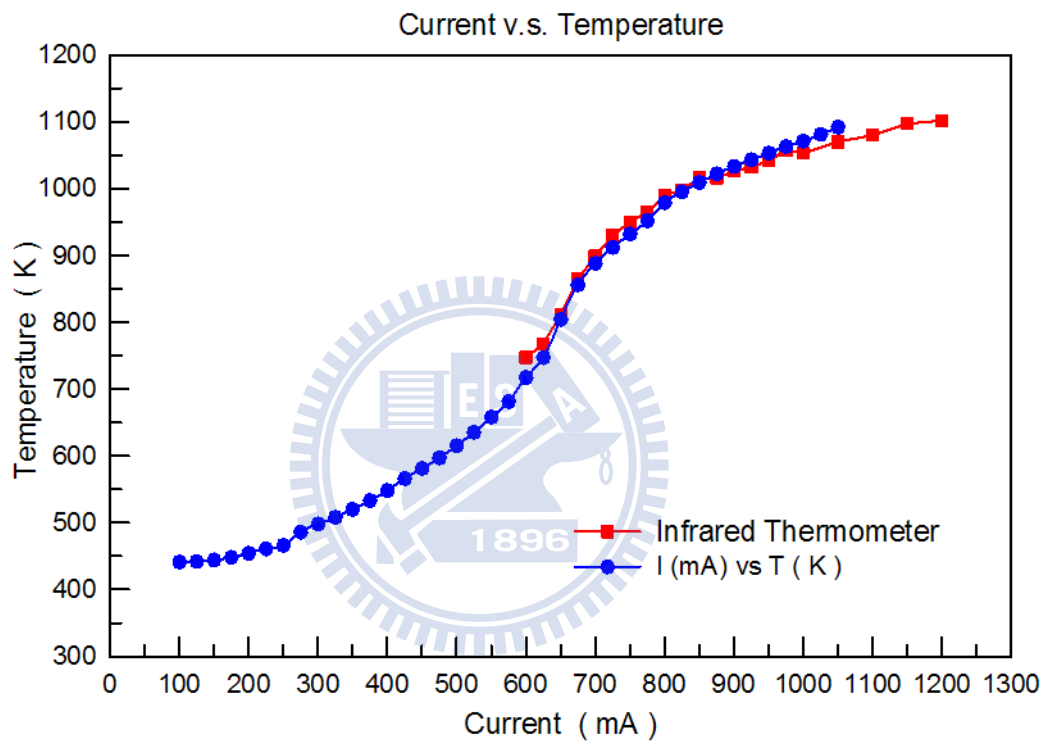
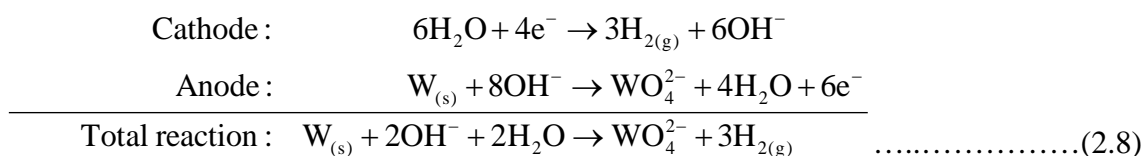


Figure 2.7 A chart of the sample current vs. corresponding temperature.

2.5 Tip Preparation

All STM tips are prepared with the traditional DC drop-off method, as shown in Fig. 2.8. The tips are typically made from cut-to-size tungsten (W) wire with diameters about 0.38 mm. The tungsten wire is electrochemically etched to produce the STM tips. It is an easy way to produce the tip. A piece of the tungsten wire and a cylindrical stainless steel are then inserted into a solution of 2M NaOH. The depth of the tungsten wire is about 1.5 ~ 2 mm below the solution level. A positive voltage about 7 V is applied to the tungsten wire. This wire acts as the anode while the cylindrical stainless steel acts as the cathode (shown in Fig. 2.8). At the anode and cathode the following reactions will take place:



The reaction etches the wire at the interface of air and the solution. This part then gets thinner and thinner, thereby forming a neck. The weight of the wire down below in the solution will eventually break the neck and causing the immersed portion of the tip to fall off. Therefore, a desired atomic tip is produced. Etching is usually stopped at this point by a feedback controller that senses the reduction in current. To remove the residual NaOH solution from the tip surface the tip are then been soaked in distilled water for 30 minutes and cleaned by pure methanol. The whole electrochemical etching process takes about 20 minutes.

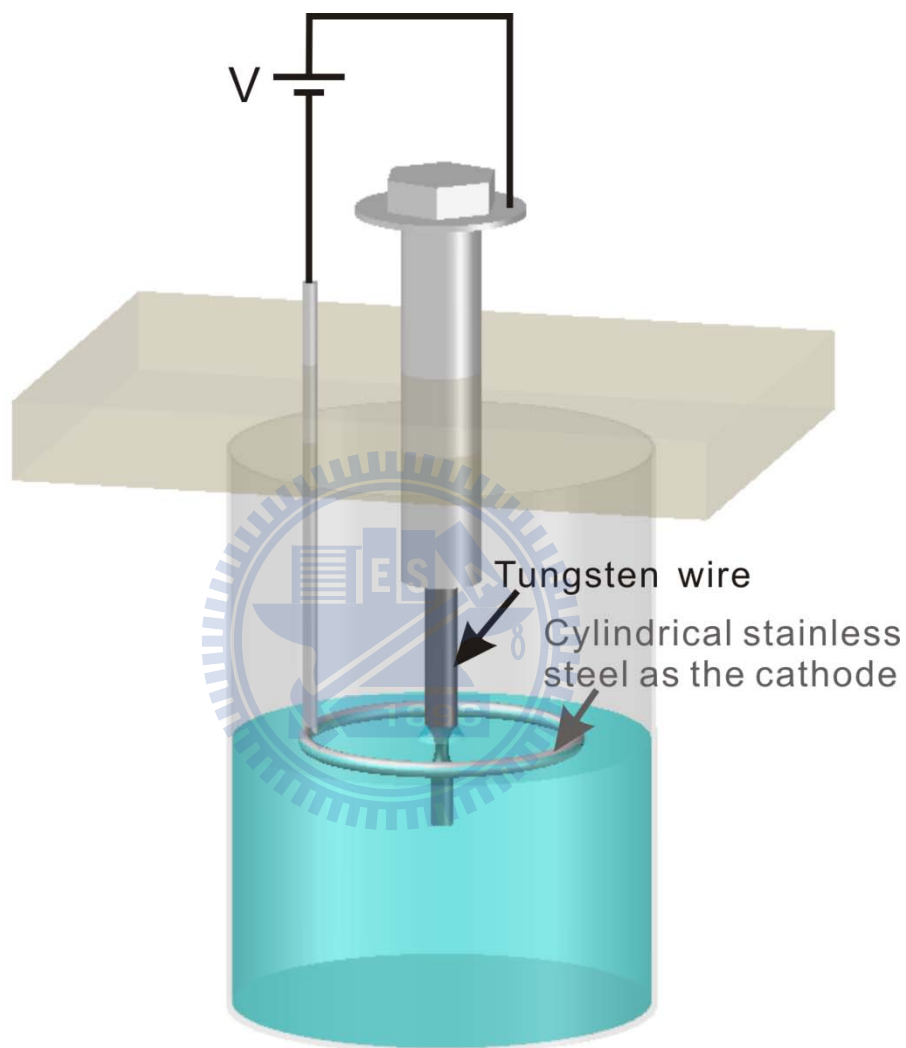


Figure 2.8 The sketch of the etching procedure for the tungsten tip. The tungsten wire is electrochemically etched to produce atomic tips. A tungsten wire is vertically inserted in a solution of NaOH as the anode. A cylindrical stainless steel is also inserted in this solution as the cathode. A positive bias is placed on the tungsten wire.

Chapter 3 Correlation of Reaction Sites during the Chlorine Extraction by Hydrogen Atom from Cl/Si(100)-2×1

The Cl abstraction by gas-phase H atoms from a Cl-terminated Si(100) surface was investigated by scanning tunneling microscopy (STM), high-resolution core level photoemission spectroscopy, and computer simulation. The core level measurements indicate that some additional reactions occur besides the removal of Cl. The STM images show that the Cl-extracted sites disperse randomly in the initial phase of the reaction, but form small clusters as more Cl is removed, indicating a correlation between Cl-extracted sites. These results suggest that the hot-atom process may occur during the atom-atom collision.

3.1 Introduction

The extraction of adsorbates on both metal and semiconductor surfaces by impinging hydrogen atoms has attracted attention as a model system for understanding the fundamental dynamics of gas-surface reactions.[15-19] One of the many model systems among these studies is the production of HCl gas species from a Cl-terminated Si(100) surface [Cl/Si(100)]. In this system, an incident H-atom flux reacts with Cl atoms adsorbed on the Si(100) surface and produces gaseous HCl molecules: $H_{(g)} + Cl_{(ad)}/Si(100) \rightarrow HCl_{(g)} + Si(100)$. This gas-surface reaction has practical applications for Cl reduction in Si atomic layer epitaxy at low temperature[1] and for the dry etching process in very large scale integration.

One of the main scientific issues behind these studies is to examine the role of three disparate surface reaction mechanisms at the gas/solid interfaces. In the idealized Langmuir-Hinshelwood (LH) mechanism, two reagents react after they have been chemisorbed and are in thermal equilibrium with the surface. Most surface reactions are believed to occur by this method. In the idealized Eley-Rideal (ER) mechanism, a direct, single gas-surface collision is responsible for the reaction between an incident gas-phase species and another adsorbed reagent. The occurrence of this pathway has been clearly demonstrated by Lykke and Kay[20] and by Rettner.[18] In the hot-atom (HA) mechanism, a trapped incident gas-phase species bounces a few times or diffuses for a short distance before reacting with another adsorbed reagent. This pathway falls between the two idealized pathways and has been shown to be the dominant reaction mechanism for the

production of both H₂ and HCl in the reaction of H atoms with H- and Cl-covered metal surfaces.[15, 21]

Halogen and hydrogen atoms form strong bonds on a semiconductor surface and barely diffuse at near room temperature.[9] Therefore, surface species are likely to retain their position after an extraction of halogen by an incident H atom.[22] Utilizing Auger electron spectroscopy and temperature-programmed desorption (TPD) mass spectroscopy, Cheng *et al.* found that the halogen removal rate by H_(g) is first order in both the Cl/Br surface coverage (θ_{Cl} , θ_{Br}) and in the H flux (F_{H}).[23] They also reported activation energy of 91 meV per Cl removed and concluded that the H-extraction process follows an Eley-Rideal reaction mechanism, where the surface reaction is mainly driven by the high internal energy of incident atomic hydrogen. Using time-of-flight scattering and recoiling spectroscopy to measure the real-time surface H and Br coverage, Koleske and Gates verified that the removal rate of Br on the Si(100) surfaces with H atom has a linear dependence on both θ_{Br} and F_{H} below 500 °C.[19] In addition to the linear dependence on θ_{Br} and F_{H} , the same reaction on the Si(111) surface also has a linear dependence on the hydrogen coverage θ_{H} , indicating a more complex kinetics. The linear dependence of the reaction rate on θ_{Br} is consistent with an ER pathway. However, the structure dependence of the reaction leads to the suggestion that the H atom may be partially accommodated at the surface in a mobile “hot precursor” state before the reaction with the adsorbed Br. From the theoretical aspect, Kim *et al.* studied the H_(g)+Cl_(ad)/Si(100) system using the classical trajectory approach and concluded that all reactive events occur through a localized ER mechanism.[24]

As mentioned earlier, previous experimental studies employed various spectroscopic techniques to measure the kinetics and dynamics of the gas-surface reaction. Hattori *et al.* first investigated the fact that atomic hydrogen extracts chlorine from Si(111)-7×7 using a scanning tunneling microscope (STM).[25] The authors showed that Cl atoms are extracted from the Cl-covered Si(111) surface by atomic H, and that the surface Si atoms, after H bombardment, are terminated with H atoms. The clean Si(100) surface after Cl termination at room temperature has a relatively simple structure: The silicon dimers retain their bonding and the surface layer consists of rows of Cl–Si–Si–Cl species.[26, 27] The surface species exhibit the same dimerized structure, namely, –Si–Si–Cl, –Si–Si–, H–Si–Si–, and H–Si–Si–H after immediate Cl extraction and further H adsorption.[27, 28] Taking

advantage of these facts, we utilized both the synchrotron radiation photoemission spectroscope and the STM to observe the Cl/Si(100) surface in atomic resolution after H-atom exposure. By comparing the results from the measurement with those from the computer simulation, it is evident that the reaction does not occur simply as the result of a single collision with unitary reaction probability between the gas atom and the adatom.



3.2 Experiment Details

The Si(100) samples were sliced from Boron-doped wafers with a dopant concentration of approximately $1.5 \times 10^{15} \text{ cm}^{-3}$. After outgassing at $\sim 900 \text{ K}$ for $\sim 12 \text{ h}$, a dimerized clean Si(100) surface was obtained by dc Joule heating to $\sim 1450 \text{ K}$ for a few seconds. After direct heating, chlorine molecules were introduced through a leak valve and a stainless-steel tube to the sample surface at room temperature to form the Cl-terminated Si(100)- 2×1 structure. A hot tungsten-spiral filament was used to produce atomic hydrogen. The filament was $\sim 5 \text{ cm}$ away from the Si(100) substrate and heated to $\sim 1800 \text{ K}$ when the chamber was backfilled for a period of time T with H_2 to a pressure P of about $2 \times 10^{-7} \text{ torr}$ without sensitivity correction. Maxwell's distribution expects the kinetic energy of the dissociated H atoms from the hot filament surface to be 0-230 meV. From the geometry of the filament and the samples, it was estimated that the incident angles of H atoms was less than $\sim 25^\circ$ from normal. The apparent H_2 exposure, i.e., $P \times T$, is presumably proportional to the actual dosage of hydrogen atoms on the surfaces. The atomic hydrogen flux was not measured directly in the present study. Instead, the apparent exposure in Langmuir ($1 \text{ L} = 10^{-6} \text{ torr s}$) is used as the relative measurement of H dosage on the Cl-Si(100) surface.

The photoemission spectra were observed at the Taiwan Light Source laboratory in Hsinchu, Taiwan. Synchrotron radiation from a 1.5 GeV storage ring was dispersed by a wide-range spherical grating monochromator. The photocurrent from a gold mesh positioned in the synchrotron beam path was monitored to calibrate the incident photon flux. Photoelectrons were collected 15° from the surface normal and analyzed by a 125 mm hemispherical analyzer in a metal shielded UHV system. The overall energy resolution was less than 120 meV. The STM measurement was performed in a separated UHV chamber.

3.3 Results

3.3.1 Photoemission results

High-resolution core level photoemission spectroscopy can be used to distinguish atoms at nonequivalent sites and in different chemical bonding configurations, according to shifts in their binding energy. Figures 3.1(a) and 3.1(b) show the respective surface-sensitive Cl $2p$ and Si $2p$ core level spectra (circles), and their decomposition into constituent components from the Cl–Si(100)- 2×1 surface before and after H bombardment at 325 K for various dosages. All fitting was least-squares fitting.[29] Each component that consists of a pair of spin-orbit split doublets is assumed to have the same Voigt line shape.

The Cl $2p$ spectra in Fig. 3.1(a) can be analyzed with a component that consists of a pair of split doublets separated by 1.60 eV. The binding energy of these Cl $2p$ spectra relative to that of the corresponding Si $2p$ remains at 99.60 eV, suggesting that the Cl atoms form similar Si–Cl bonds. Figure 2 plots the integrated intensities of the Cl $2p$ spectra (I_{Cl}), which are proportional to the surface Cl coverage. The integrated intensity of the bottom spectrum is normalized to be 1.0 because the chlorine coverage is nominally 1 ML for the Cl-saturated Si(100) surface prior to H-atom bombardment. I_{Cl} decreases linearly with the dosage of H atoms in the early stage, indicating that Cl atoms were removed by impinging H atoms. This result is consistent with a previous study.[23]

The bottom spectrum in Fig. 3.1(b) shows the Si $2p$ core level spectra for the Cl–Si(100)- 2×1 surface. This Si $2p$ spectrum consists of two components, B and Si⁺, separated by about 0.9 eV. The B component is responsible for emission from the bulk and the Si⁺ component from the surface Si–Cl species.[30] As the exposure of atomic hydrogen increases, both the intensities of the Si⁺ component and the Cl $2p$ spectra drop off. This occurrence suggests that H atoms reduce the surface Cl coverage, similar to the findings of a previous report.[23] After > 1000 L of apparent exposure, the line shape of Si $2p$ is similar to that [top spectrum in Fig. 3.1(b)] obtained by direct, high-dosage hydrogen exposure on the clean Si(100)- 2×1 surface at room temperature.[31] This observation indicates that hydrogen atoms terminate nearly all surface dangling bonds and form a mixture of dihydride and monohydride surface when most Cl atoms are extracted. It should

be noted that a small component labeled Si_{2+} emerges in Fig. 3.1(b) after H impingement. The chemical shift of Si^{2+} , around 1.78 eV on the higher bonding energy side of B, is consistent with a charged state of +2 for Si atoms and is responsible for SiCl_2 species.[26] Presumably, the SiCl_2 species were formed as a consequence of the highly exothermic uptake of halogens during the extraction. Although more study is needed, the emergence of the dichloride species implies that impinging H atoms induces other surface reactions besides extracting upon collision with a surface adatom.



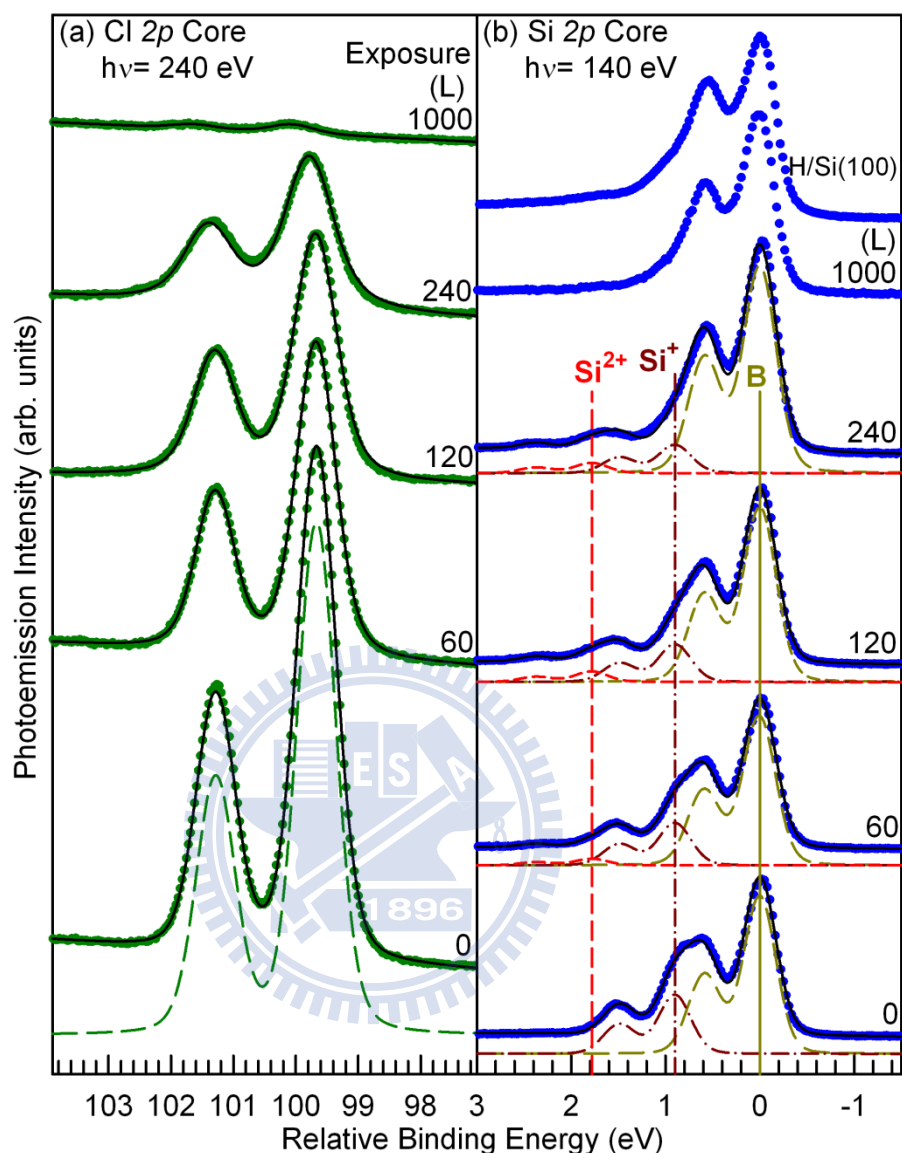


Figure 3.1 The (a) Cl $2p$ and (b) Si $2p$ core level photoemission spectra (circles) for the Cl-Si(100)- 2×1 surface and the same surface after various apparent H-atom dosages as labeled. The solid curves are fits to the spectra. The curves labeled B (long dashed curves), Si $^{2+}$ (dashed dot), and Si $^{+}$ (short dashed curves) are the results of decomposition of the Si $2p$ spectra into contributions from the bulk, Si-Cl, and Cl-Si-Cl species, respectively. The energy zero in (b) refers to the $2p_{3/2}$ bulk position for the Cl-Si(100)- 2×1 surface. To eliminate the band bending effect, the relative binding energy for the Cl $2p$ refers to the corresponding Si $2p_{3/2}$ line of the B component in (b).

3.3.2 STM results

The clean Si(100) surface consists of rows of dimers, where the two dangling bonds from the two atoms in a dimer form a weak π bond.[32] Cl adsorption on a clean Si(100) surface saturates the dimer dangling bonds while preserving the basic (2×1) dimer structure without buckling, as shown in Fig. 3.3(a).[9, 33] In Fig. 3.3(a), a handful of dark sites can be discerned, each occupying one side of a Cl–Si–Si–Cl species. As Figs. 3.3(b) and 3.3(c) show, the density of these dark sites increases with the H exposure. The dangling bonds generated during the Cl removal exhibit a higher apparent height due to enhanced tunneling near the Fermi level, and they are highly reactive to further H adsorption.[34] The dark sites in Fig. 3.3 are H-terminated sites. The initial H coverage on the Cl/Si(100) surface is less than 0.02 ML. The presence of some initial surface H is likely due to the residue in the cleaning process and/or the adsorption of impurity by the HCl molecules in the Cl₂ gas source. The remaining Cl coverage after H exposure can be obtained by directly counting its density in the STM images. The results are plotted in Fig. 3.2. Since the STM and photoemission measurements were performed in different chambers, the actual H dosages for the two measurements are different but proportional, as shown in Fig. 3.2.

When the substrate temperature is held at RT during H-atom exposure, a reaction site, where a Cl atom is removed by an H atom and an H atom is subsequently adsorbed, presumably undergoes no diffusion.[22, 35] The brightest humps in the images are likely weakly bonded terrace SiCl₂ moieties, as evident from the photoemission spectra and as discussed in the previous section. In addition, the remaining Cl-terminated sites and bright humps, and most of the reacted sites in Figs. 3(b) and 3(c), appear to be H terminated. At first glance, the H-terminated sites, or the Cl-extracted sites, appear to be randomly dispersed. However, as will be analyzed and discussed in the following section, the density and the sizes of the clusters grouped together in neighboring Cl-extracted sites are larger than those created by random extraction. At higher H-atom exposure, even twodimensional islands with a H/Si(100)-2×1 structure, as shown in Fig. 3.3(c), can be easily found. Figure 3.4 shows an STM image for the H_(g)+Cl_(ad)/Si(100) reaction at a substrate temperature of ~600 K. Similar isolated dark sites occupying one side of a dimer can be easily identified, since they are H-terminated sites after Cl extraction. The density of the Cl-extracted sites increases as the H-atom dosage and the clustering of reaction sites become evident at higher H-atom dosage. The results are similar to those obtained at near room temperature.

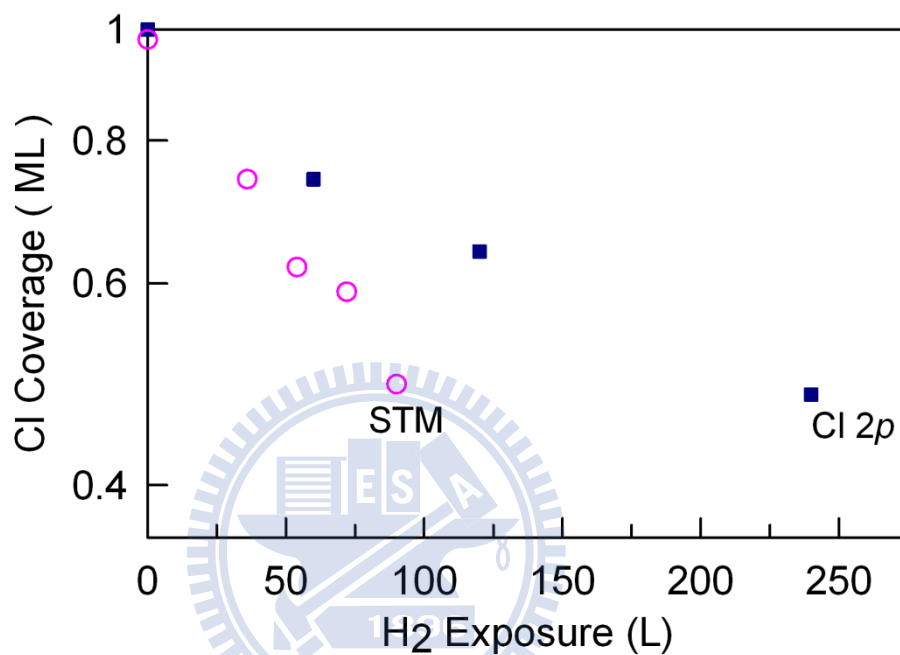


Figure 3.2 Cl coverage calculated from the integrated intensities of the Cl 2*p* core level spectra in Fig. 3.1(a) (solid squares) and from those counting from the STM images (open circles). The initial coverage is nominally 1.0 ML based on the STM result.

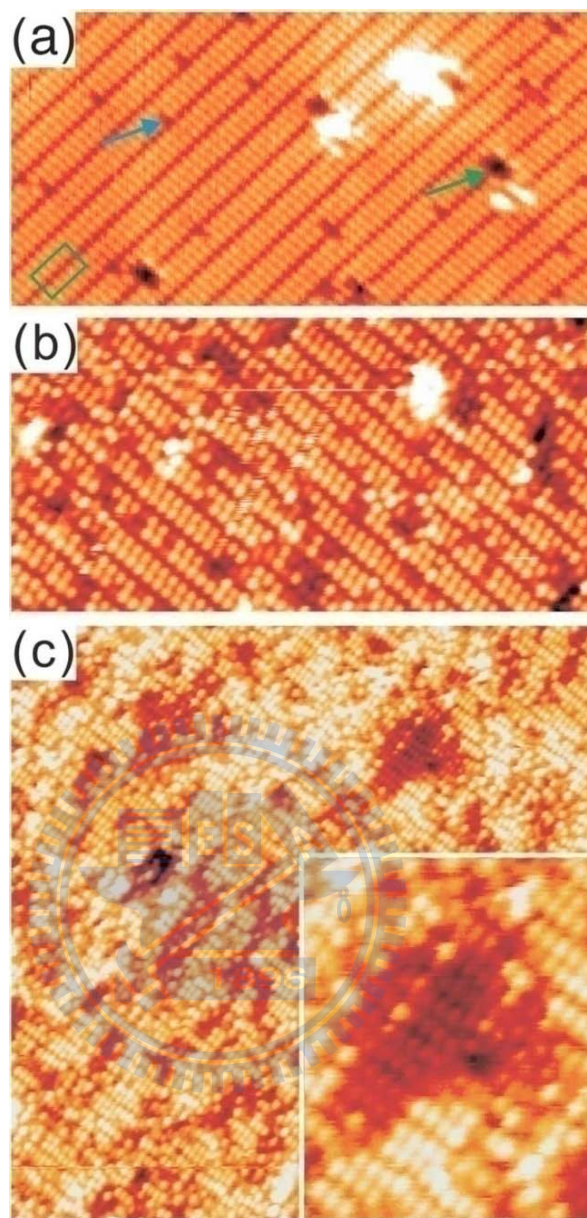


Figure 3.3 STM images of the Cl/Si(100)-2 \times 1 surface after (a) 0, (b) 36, and (c) 90 L apparent dosages of H atoms. The sample bias used was +2 V. In (a) the green rectangle box, running from the upper right to the lower left, encloses a row of five Cl–Si–Si–Cl (monochloride) species. A surface Cl atom appears as a bright protrusion and forms a narrow ellipse with another in the neighboring monochloride row in the image. Notably each of two nearest Cl adatoms in the empty state images are not from a single Cl–Si–Si–Cl species, but are a part of two adjacent Cl–Si–Si–Cl species. The green and blue arrows point to a missing dimer defect site and a H-termination site, respectively. The inset in (c) shows a 2 \times 1 area of nearly complete H termination after Cl extraction. The size of a 1 \times 1 unit cell in the image is 3.84 \times 3.84 Å².

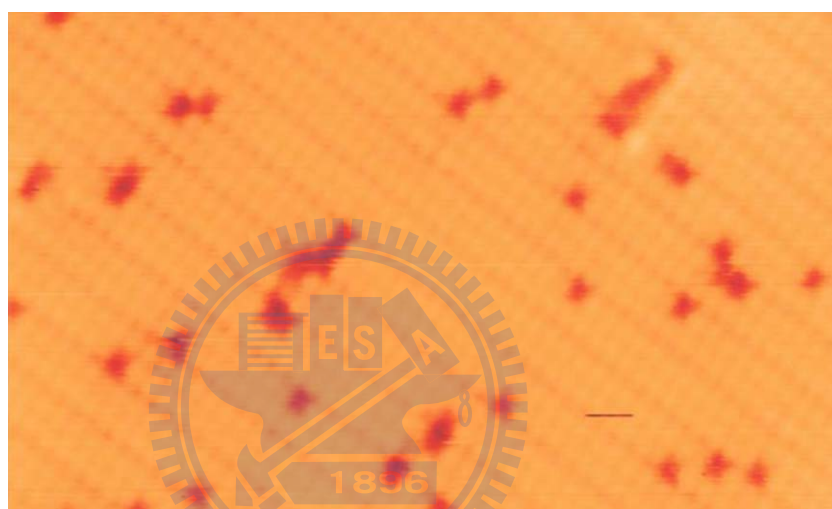


Figure 3.4 STM images of the Cl/Si(100)-2 \times 1 surface after 12 L apparent dosages of H atoms at a sample temperature of 600 K. The sample bias used was +2 V.

3.4 Discussion

In the ER mechanism, a Cl-extraction reaction occurs via a collision-induced reaction. The calculated cross section is smaller than a unit cell within a small proximity around the spot where an H atom strikes.[24] The gas-phase H atoms impinge on the surface in a random fashion. In this scenario, a new Cl-extracted site is generated no matter what neighboring chemical environment surrounds the site where an H atom strikes. In other words, the extraction probability upon collision with an H atom is not changed when a Cl-Si surface species is neighboring one or more dangling bond sites or monohydride sites. If this scenario is valid, then the distribution of the Cl-extracted sites by the random and sequential impingement of gas-phase H atoms will be completely random in the STM images.

Figures 3.5(a)–3.5(c) show the results of the impingement site distribution from the computer simulation based on this assumption. In the simulation, a reactive site is randomly generated since the impact parameter found in the classical trajectory approach is small.[24] In Fig. 3.5, the Cl-extracted sites are classified into eight categories, and are marked in different colored intensity scales (labeled 0–8), according to the degree of reaction-site clustering. A site in categories numbered $k = 0, 1, 2,$ and 3 is a Cl-extracted site with $0, 1, 2,$ and 3 of its four nearest neighboring Cl-extracted sites (labeled $s = 1–4$ in Fig. 3.6), respectively. If a Cl-extracted site with its four nearest neighboring Cl extracted is called a “surrounded site,” a site in category $4, 5, 6, 7,$ and 8 is a surrounded site and has $0, 1, 2, 3,$ and 4 nearest neighboring surrounded sites, respectively. In the classification scheme, the category number k of a Cl-extracted site indicates the number of other extraction reactions occurring in its immediate vicinity. Therefore, the larger the cluster formed by the Cl-extracted sites, the darker the cluster appears in the image.

Figure 3.6 displays the “unnormalized” pair distribution function (g') of Cl-extracted sites,

$$g'(j) = g(j)\theta = \frac{1}{N} \sum_{i=1}^N \frac{n_i(j)}{m(j)} \dots\dots\dots(3.1)$$

where $n_i(s)$ is the number of s th-nearest-neighbor Cl-extracted sites around the i th Cl-extracted site (labeled 0 in Fig. 3.6), θ denotes the coverage of the Cl-extracted sites, and

$m(s)$ denotes the number of s th-neighbor sites.[14] As expected, the pair distribution g' obtained from the simulated images is roughly equal to θ , independent of site index s . Figure 3.6 shows that g' calculated from simulation images such as Figs. 3.5(d)–3.5(f) is in agreement with those expected for a completely random distribution. In contrast, g' for nearest neighboring sites $s = 1–4$ obtained from STM images is boosted by about 20%. g' for next nearest neighboring sites $s = 5–10$ is also boosted at higher coverage. The deviation of g' from the mean coverage θ suggests the existence of correlation and interaction between Cl-extracted sites and, therefore, rules out the pure ER process with unitary reaction probability.

To further examine whether or not the cluster formation of Cl-extracted sites results from random H impingement, STM images taken after the reaction were digitized and are shown in Figs. 3.5(d)–3.5(f) in a similar fashion to those in Figs. 3.5(a)–3.5(c). A direct visual comparison between Figs. 3.5(b) and 3.5(e), and Figs. 3.5(c) and 3.5(f) suggests that the site population for categories with a greater k obtained from the STM measurement [$P_{\text{STM}}(k)$] is greater than that [$P_{\text{Sim}}(k)$] from the corresponding simulated images. Their ratios $P_{\text{STM}}(k) / P_{\text{Sim}}(k)$, plotted in Fig. 3.7, deviate significantly from 1.0, especially for $k > 4$. This finding also indicates that the simulation based on the assumption of a pure ER process deviates from the experimental results. The cluster formation of Cl-extracted sites can only be realized if an impinging H atom “senses” the chemical environment in a small (HA) or large (LH) range beyond the collision spot. The sizes of the clusters in Figs. 3.5(d)–3.5(f) are not large; the larger-than-expected pair correlation found in the small coverage of the extraction reaction sites is limited to the nearest neighboring sites ($s = 1–4$). These facts suggest that the reaction of Cl extraction likely follows that of the HA process.

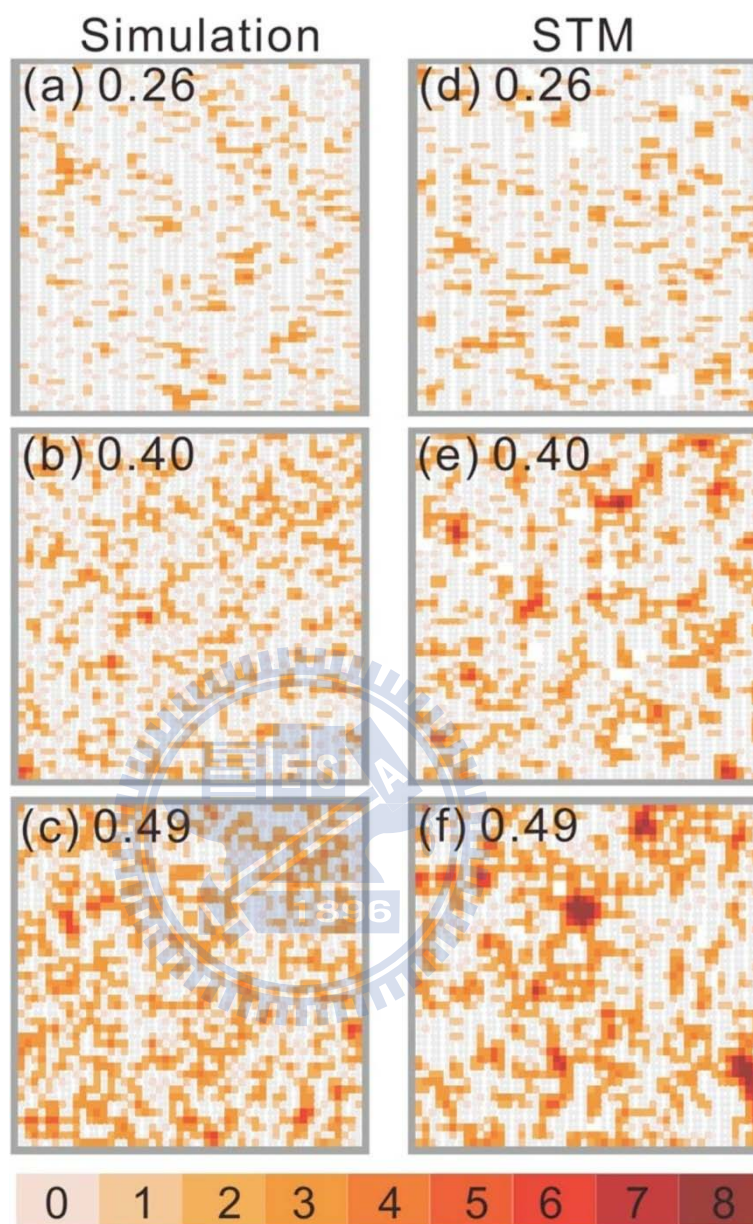


Figure 3.5 Distribution of Cl-extracted sites obtained from [(a)–(c)] simulation and [(e)–(f)] STM. The coverage of Cl-extracted sites in monolayer is labeled. The simulation starts on an area which initially consists of 50×50 Cl adatom sites. A Cl-extracted site is classified into eight categories and represented by a 1×1 cell of different colors as indicated. The “digitalized” STM images were obtained from parts of STM images typically about $30 \times 30 \text{ nm}^2$ in size.

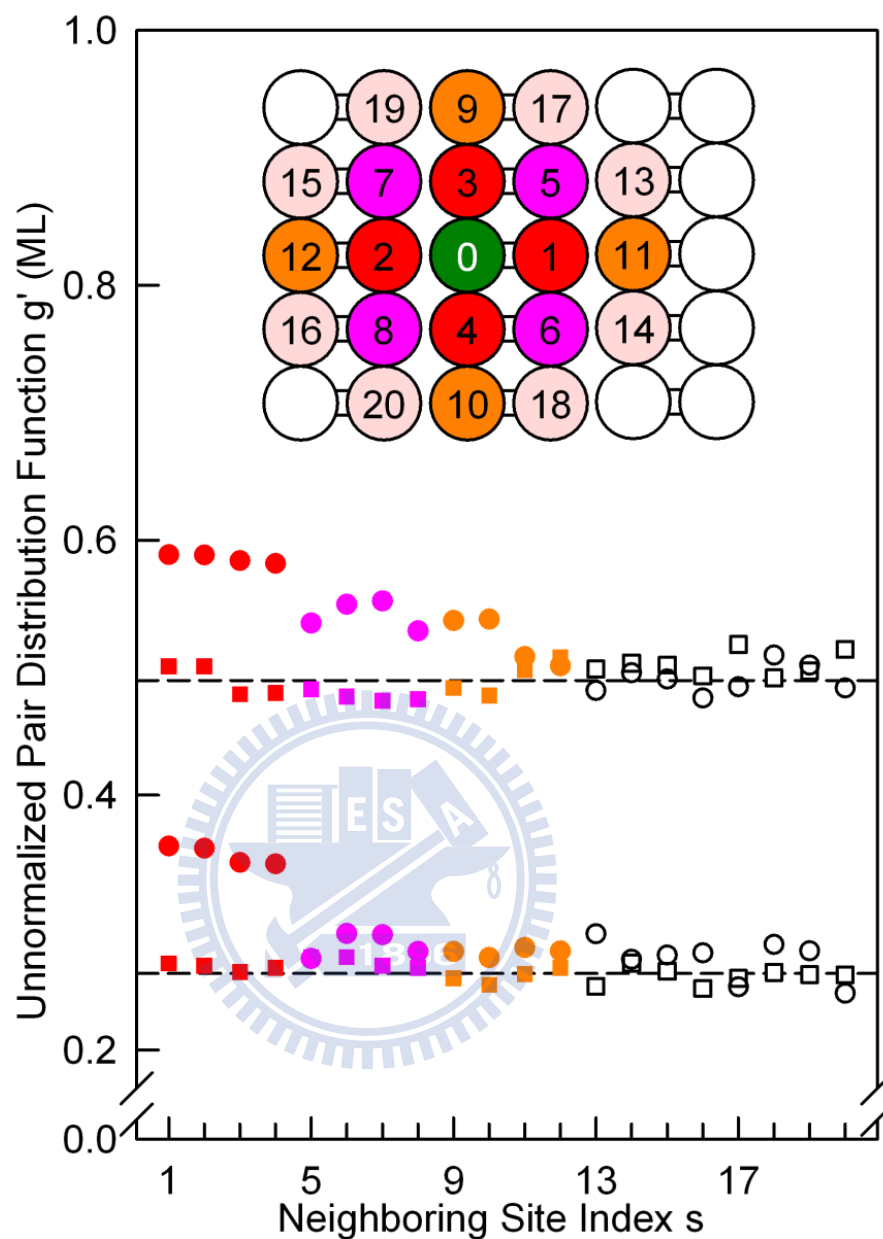


Figure 3.6 The Cl-terminated Cl-Si(100) surface and the unnormalized pair distribution function of Cl-extracted sites vs the neighboring site s obtained from a set of the STM images (circles) and the simulation (squares), and the completely random distribution calculation (dashed curves). The coverage of Cl-extracted sites in monolayer is labeled. The inset shows the Cl/Si(100)- 2×1 lattice; each circle corresponds to an initial Cl adatom site. Numbers mark the respective sites around a Cl-extracted site at the center position (labeled 0). The distribution functions obtained from several STM measurements and simulations vary slightly for each s , but their overall trends are the same.

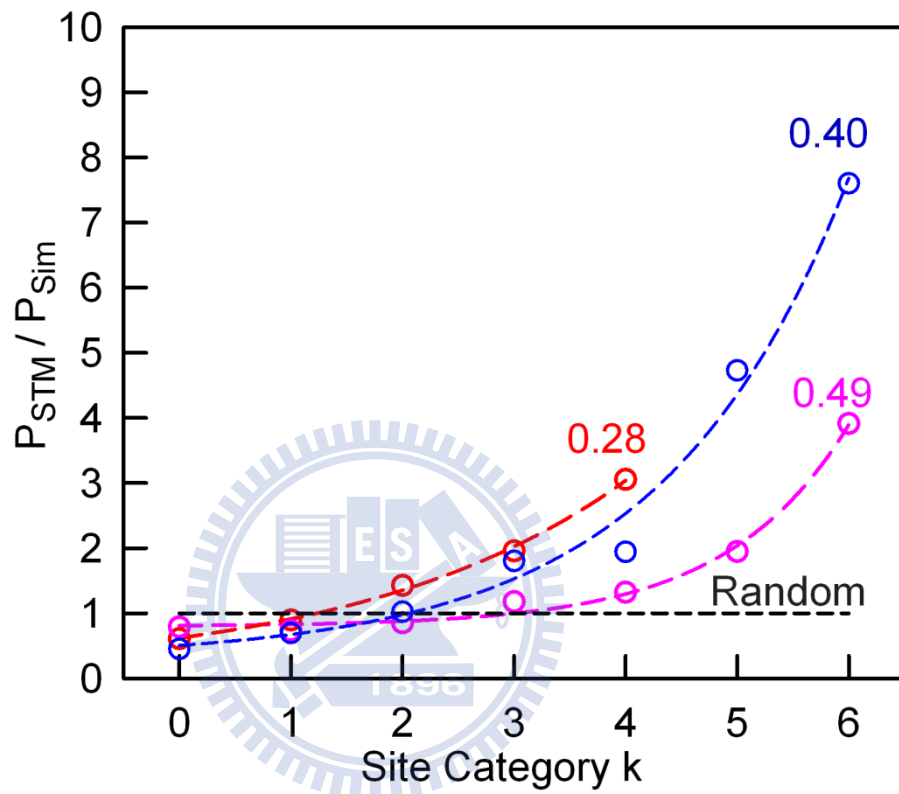
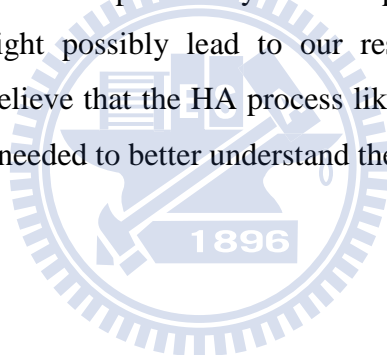


Figure 3.7 The ratio of the population density obtained from a set of STM images P_{STM} to that from simulated images P_{Sim} vs site category. The coverage of CI-extracted sites in monolayer for each curve is labeled. The ratios obtained from several STM measurements and simulations vary slightly for each category, but their overall trends are the same.

3.5 Conclusion

Distinguishing a detailed surface reaction mechanism has been an important but difficult issue. The $H_{(g)}+Cl_{(ad)}/Si(100)$ is an important prototypical system for the study of the ER, HA, and LH mechanisms. In our work, a combination of atomic resolved STM images, spectroscopic measurements of core level photoemission and computer simulations provide a detailed picture of the atomic processes involved in this seemingly simple gas-surface reaction. The core level measurement and STM images observed the formation of $SiCl_2$ surface species, indicating that “some” additional reactions occur beside the removal of Cl upon impingement of H atoms. Analysis of the STM and simulated images shows that the Cl-extracted sites are correlated to the neighboring Cl-extracted sites. These experimental results cannot be explained by the pure Eley-Rideal process with unitary reaction probability. We recognize that other mechanisms, for example, an Eley-Rideal abstraction process with a reaction probability which depends on the local surface coverage of Cl and maybe H, might possibly lead to our results. However, our findings and consideration lead us to believe that the HA process likely occurs during the atom-atom collision. Further study is needed to better understand the nature of the gas-solid reactions.



Chapter 4 Possibility of direct exchange diffusion of hydrogen on the Cl/Si(100)-2×1 surface

The diffusion behavior of hydrogen substitutional sites on the chlorine-terminated Si(100) surface was investigated at elevated temperatures using time-lapse scanning tunneling microscopy (STM). STM movies show that each hydrogen atom undergoes Brownian motion within a monochloride dimer row. The position of a hydrogen substitutional site is exchanged directly with that of an immediate neighboring chlorine atom in either the same dimer (intra-dimer diffusion) or in one of the two adjacent dimers in the same row (intra-row diffusion). Accordingly, conceptual direct exchange diffusion (DED) in a two-dimensional lattice was experimentally observed. Analysis of STM movies at various temperatures yielded rather low attempt frequencies and energy barriers, leading to the suggestion that the diffusion mechanism involves an intermediate low-energy molecular state. Density functional theory (DFT) calculations were also performed and provided partial support for the proposed diffusion mechanism.

4.1 Introduction

The diffusion of atoms, molecules and small clusters is one of the fundamental processes that occur on surfaces.[36-39] A thorough comprehensive understanding of the surface diffusion mechanisms at an atomic level is extremely important to the technological development of surface catalysis and several nanofabrication processes such as thin film growth and etching. An atom can diffuse by exchange of position with that of a neighbor, either directly or by rotation.[40] Such diffusion does not involve defects and commonly requires high energy, so the probability of its occurrence is expected to be very low and most diffusion processes discussed in the literature proceed by the exchange of an atom with a neighboring vacancy defect.

The typical description of vacancy-driven surface diffusion is that an adatom hops among adsorption sites on a surface lattice via transition sites at a rate that increases with temperature. Although this conventional model of adatom diffusion via nearest-neighboring jumps generally requires a minimum of an activation energy of diffusion E_a , various pathways for surface diffusion have been identified both theoretically and experimentally.[37, 41, 42] For example, hydrogen has been demonstrated to diffuse on clean metal surfaces by quantum tunneling, in a process that is called tunneling diffusion.[43]

Adatom displacements to the adsorption site of a non-nearest-neighbor, known as long jumps, have also been shown experimentally to proceed at temperatures as low as $0.1 T_m$ (melting temperature) and to dominate the diffusion process over single jumps at elevated temperatures in some cases.[37, 44] Another particularly interesting example of an unconventional mechanism is diffusion via atomic exchange.[37] This process involves exchange between an adatom and an adjacent atom in the surface lattice. Atomic exchange processes have been demonstrated take place in both hetero-diffusion and self-diffusion. In the three dimensional case, a similar exchange diffusion mechanism without defects has been occasionally proposed to explain some new diffusion phenomena in solids.[45] This exchange diffusion is commonly referred to as concerted exchange (CE). However, CE does not seem to occur in practice since the associated transition state requires a high input of energy for the simultaneous and cooperative motion of more than one atom at a time.

This work describes a newly observed diffusion phenomenon on the Cl-terminated Si(100) surface. Scanning tunneling microscopic movies reveal that hydrogen substitutional defects migrate within the top chlorine layer and that this process is thermally activated. Hydrogen substitutional sites diffuse at moderate temperature without the participation of vacancies. In the simplest model — direct exchange mechanism or DED, an H-site and a neighboring Cl-site in the surface lattice swap positions directly. This investigation proposes a model of this diffusion process and performs *ab initio* energy calculations. The success and discrepancy of this model and other alternative explanations are also discussed.

4.2 Experiment Details

The diffusion process was examined in real space and real time at atomic resolution by using a variable-temperature scanning tunneling microscope (STM) in a vacuum chamber with a base pressure of 1×10^{-10} torr. Samples of Si(100) were prepared from commercial wafers, outgassed in the vacuum chamber, and then heated by direct Joule heating to ~ 1400 K to generate clean and well-ordered surfaces with reconstructed dimers. After the clean Si(100) surface was cooled to almost room temperature, ultra-pure gaseous chlorine was introduced to the sample surface through a precision leak valve and a stainless-steel tube. The substrate was heated by passing a controlled dc current directly through the sample. The sample temperature that corresponds to each current was obtained using an infrared optical pyrometer and calibrated by gluing a tiny type-K thermocouple to the center of the sample following the final last STM run. The uncertainty in the temperature measurement was estimated to be approximately ± 5 K. All STM images were captured in constant current mode. Various bias voltages were applied to support the positive identification of the various different surface species with negligible tip-induced diffusion. However, all of the images presented below were taken at a sample bias of -2.2 V and a tunneling current of ~ 0.1 nA.

Calculations of diffusion barriers were conducted using density-functional theory (DFT) calculations within the local-density approximation in the Vienna *ab-initio* Simulation Package (VASP).[46] Briefly, the Ceperley-Alder exchange-correlation function,[47] as parameterized by Perdew and Zunger,[48] was utilized. A repeated-slab supercell model was also applied. Each slab comprised eight atomic layers of Si and adlayers of Cl and H on the top surface. The bottom two silicon layers were constrained to remain in bulk-like positions. H atoms were attached to the bottom-layer Si atoms to saturate their dangling bonds. The heights of the supercell in the [100] direction were fixed at 20 \AA , which was large enough to prevent coupling between the slabs, even when Cl and H were adsorbed on both Si surfaces. The wave functions were expanded using a plane-wave basis with an energy cutoff of 25.72 Ry (350 eV). The electron-ion interaction pseudopotentials that were supported by VASP were evaluated using the projector-augmented wave (PAW) method. A $(4 \times 4 \times 1)$ k Monkhorst-Pack grid, equivalent to eight irreducible \mathbf{k} points, was adopted to sample the surface Brillouin zone of a unit cell, which was two dimer rows wide with four

dimers in each row. The structure was optimized until the residual force that acted on each atom was less than 0.01 eV/\AA . Then, the nudged elastic band (NEB) method was used to determine minimum barrier energy diffusion paths between known initial and final geometries.[49]



4.3 Results and Discussion

The Si(100) surface has been well characterized because of its importance in fundamental science and technology. In a clean Si(100) surface, bulk truncated silicon surface atoms pair into dimers, eliminating one dangling bond per atom to reduce the surface free energy. Each surface Si atom has one dangling bond and the clean Si(100) surface.[32] The interactions of hydrogen and halogen with silicon surfaces have been extensively experimentally and theoretically examined because of fundamental interest in their importance to etching and growth processes.[32, 50-52] Many works have established that Cl atoms are singly bonded to dimer dangling bonds on Si(100) while the dimer structure is preserved without buckling, forming a (2×1) monochloride surface. A hydrogen atom also forms a similar single bond with a Si dangling bond and, therefore, readily replaces a Cl-terminated site without modifying the dimerized substrate structure, as displayed in Fig. 4.1(a).[23, 53]

4.3.1 STM results

Figure 4.1(b) shows that the initial Cl/Si(100)-2×1 surface is well ordered following saturated exposure to Cl₂ at room temperature, with a few randomly located “dark” sites that are substituted for a single Cl site. Most of these defects are isolated and have a typical density of < 2%. Similar dark-looking sites can also be formed by exposure to a beam of light H atoms on the Cl/Si(100)-2×1 surface. The “dark” sites generated either by an atomic H beam or by Cl₂ exposure show the same characteristics, as revealed by STM images obtained under various conditions and scanning tunneling spectra, suggesting that all these “dark” sites are hydrogen substitution sites, or H-sites.[53] These H-sites formed during the Cl₂ exposure are perhaps due in part to chemisorption during sample flash at high temperature.

Cl/Si(100)-2×1 surfaces with various amounts of H substitutional defects remain clean and stable for days under UHV conditions at room temperature. H-sites are static at room temperature and are observed to become mobile in STM images acquired at sample temperatures of above ~500 K. Figure 4.2 presents four representative and consecutive STM images from an STM movie of a (2×1) chlorine terminated Si(100) surface that was maintained at 560 K. In the images, H-sites usually move one atomic step at a time to occupy a Cl-site either on the opposite side of the same dimer (intra-dimer diffusion) or on the

neighboring dimers in the same dimer row (intra-row diffusion). After hydrogen has been displaced, the H-site does not become an isolated dangling bond, but appears as a Cl-site. A dangling bond is apparently higher than a Cl-site in the STM images, and so they can be easily distinguished.[11] Restated, an H-site appears to diffuse by the exchange of its position directly with that of a neighboring Cl-site. A displacement of two atomic steps can occasionally be observed between two consecutive images. The non-nearest-neighbor jumps occurred less frequently as the interval between two STM images were shortened, suggesting that most of them involved two single-jumps (two consecutive intra-row diffusion steps or a combination of an intra-row step and an intra-dimer step). The diffusion of H-sites to a neighboring dimer row is rarely observed.

Many STM movies were obtained and diffusion rates were calculated between 530 and 615 K. As the sample temperature increased, the H-sites diffused more frequently, suggesting that this process was thermally activated. Figure 4.3 plots the diffusion rates obtained from STM movies are plotted as a function of inverse temperature. The plots follow closely the Arrhenius law and yield an energy barrier of 1.29 eV and a prefactor of $1.31 \times 10^9 \text{ s}^{-1}$ for intra-row diffusion. Intra-dimer diffusion has a prefactor $6.64 \times 10^7 \text{ s}^{-1}$ and a slightly smaller energy barrier, of only around 1.17 eV. The values of the prefactors are orders of magnitude lower than the universal prefactor of $10^{13 \pm 1} \text{ s}^{-1}$, suggesting a more complex process than that of a vacancy-driven diffusion and/or considerable perturbation of the substrate during diffusion.[37, 38, 54] The activation energies obtained here are considerably lower than those of intra-row H atomic diffusion (1.7 eV),[35, 55] but higher than that (1.0 eV) of H intra-dimer diffusion and that (1.1 eV) of Cl diffusion on a clean Si(100) surface.[56, 57]

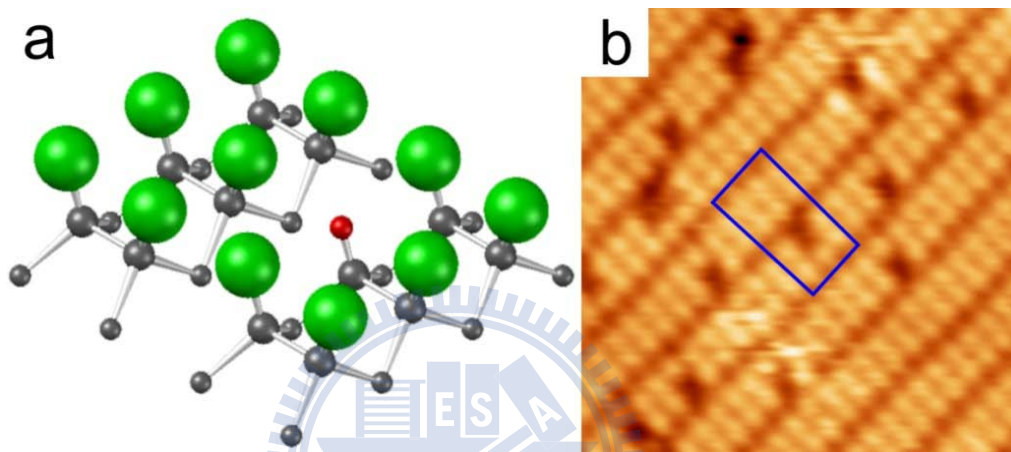


Figure 4.1 (a) Ball and stick model of Cl-terminated Si(100) surface. The top-layer Cl atoms are green and a substitute H atom is red. Cl atoms each terminate a dangling bond on the Si surface with dimer reconstruction. (b) STM image of Cl-terminated Si(100) surface taken at room temperature. The dark defects are H substitution sites. The blue rectangle delineates the area that is schematically presented in (a). $V_s = -2.2$ V; $I_t = 0.22$ nA. Image size $\sim 74 \times 74 \text{ \AA}^2$.

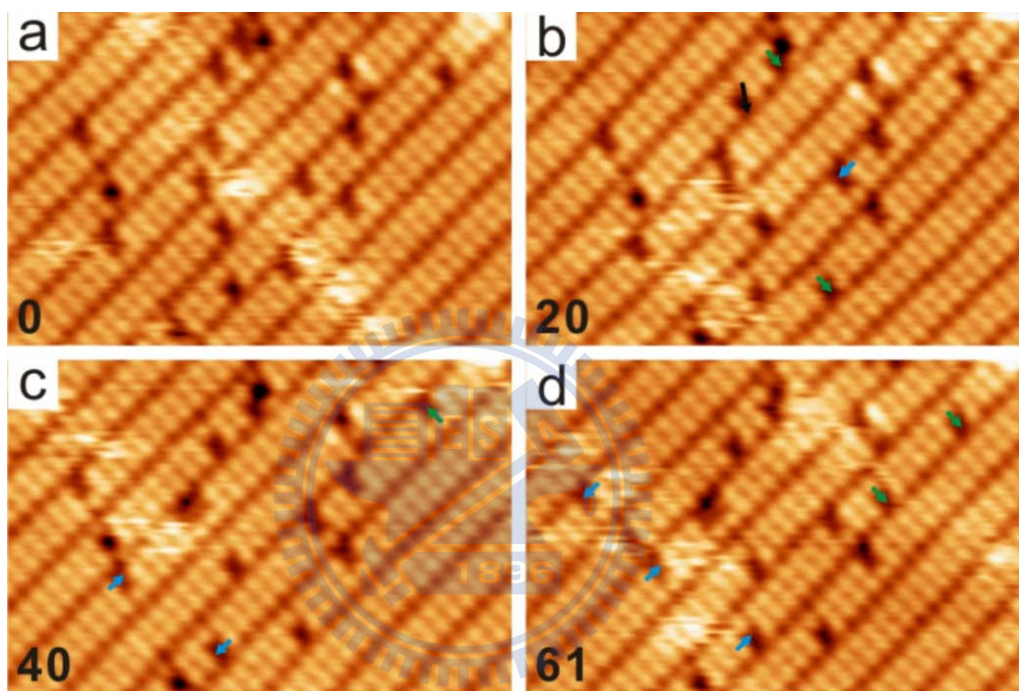


Figure 4.2 (a)-(d) Four consecutive STM images from movie (20 s/frame). The relative recording time of each image in seconds is indicated at the bottom left corner. The arrows indicate intrarow (blue) and intradimer (green) diffusion of an H site. The black arrow in (b) indicates the result of two jumps between the two frames. Image size $\sim 74 \times 49 \text{ \AA}^2$.

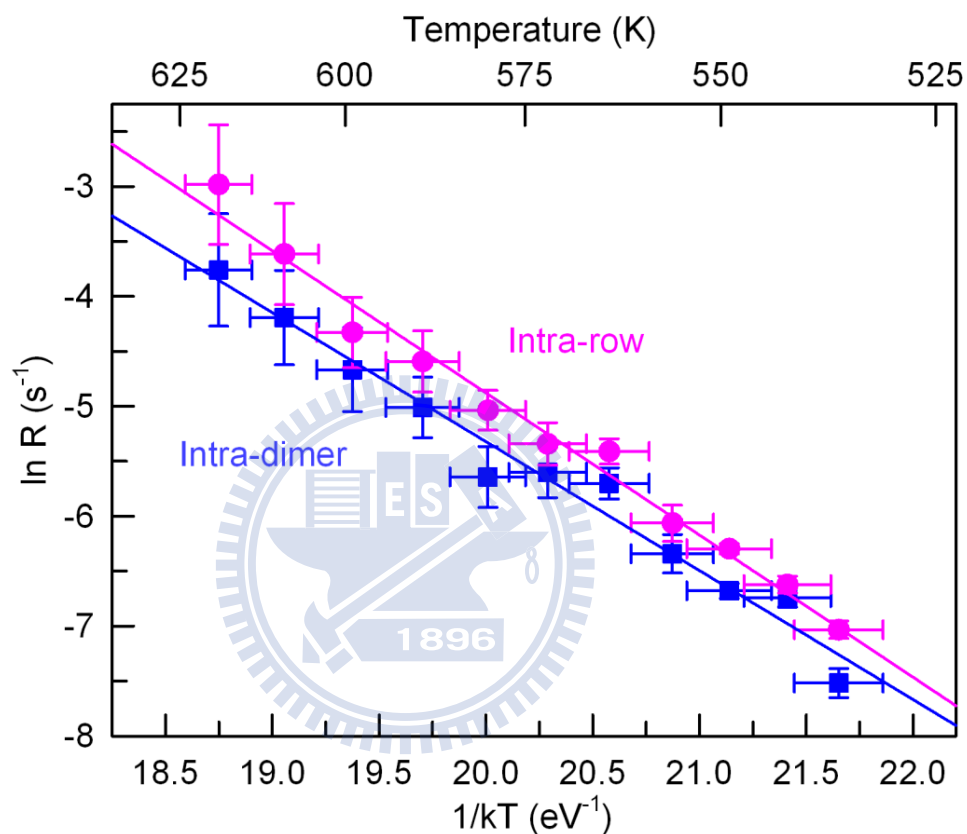


Figure 4.3 Arrhenius plots for intra-dimer and intra-row H-Cl exchange diffusion. The solid lines are fits. These lines yield an activation barrier E_a of 1.29 ± 0.05 eV and a pre-exponential factor ν_0 of $10^{9.1 \pm 0.5} \text{ s}^{-1}$ for intra-row diffusion in the dimer row direction and $E_a = 1.17 \pm 0.06$ eV; $\nu_0 = 10^{7.8 \pm 0.5} \text{ s}^{-1}$ for intra-dimer diffusion.

4.3.2 Model of DED mechanism and NEB calculations

As described above, the diffusion of hydrogen substitutional sites involves the concerted motion of H and nearest Cl atoms. Si-Cl and Si-H bonds have large bond energies of 3.956 eV and 3.301 eV, respectively. If the concerted motion of the H and Cl atoms involve the simultaneous breaking of Si-Cl and Si-H bonds, then much energy will be clearly required. However, the diffusion barrier is similar to those of simple H-adatom diffusion. Accordingly, a key question that is raised by the DED model is as follows: if two surface atoms with strong chemical bonds with a substrate are responsible for H diffusion, then how do they organize themselves into a low-energy state during the process? Notably H-Cl has a large bond energy of 4.444 eV. Hence, a natural conjecture is that two nearby intra-dimer or intra-row H and Cl atoms form an HCl-like molecular configuration as an intermediate product, and then switch positions during rebonding.

In an effort to confirm the existence of an HCl molecule as an intermediate state, the NEB method built in the VASP code was employed; the NEB technique has also been applied to determine activation energies of hopping and exchange-diffusion on surfaces. In this calculation, a “band” of intermediate states is produced by simple interpolation along an assumed reaction path that connects the initial state (with H and Cl on a single dimer or on a single side of two adjacent dimers in the same dimer row) with the final state (in which the positions of H and Cl are exchanged). Then, the atomic configurations in the different geometries are iteratively optimized using only ionic-force components that are perpendicular to the hypertangent.

Atomic configurations after NEB minimization, as presented partially in Fig. 4.4, show that H and Cl atoms move toward their final state positions approximately in the plane defined by $\langle 100 \rangle$ and along the line that connects initial H and Cl positions. During the transition, the relevant dimer bonds remain intact; no bridge-bonded state, such as that associated with Cl adatom diffusion, is obtained. In the image chain, the Cl atom appears to move along the outer circle, while H remains closer to the surface. The length of the bond between the H and Cl atoms is 1.32 Å, which is close to that (1.27 Å) in an HCl molecule.

The heights of the activation energy barriers obtained by comparing the initial and transition states are large (~ 2.860 eV) for both intra-dimer and intra-row DED, as presented in Fig. 4.4. This value is close to the energy (2.7 eV) required to remove the Cl and H atoms

away from the surface and to form a H-Cl bond, suggesting that both Si-Cl and Si-H bonds are completely broken and HCl molecules are present. Although the experimental value may be imprecise, the heights of the energy barriers (~ 2.8 eV) in the LDA-DFT calculations fall outside the range of experimental uncertainty. Other modeling approaches, such as generalized gradient approximation (GGA) with spin and tight binding, have been demonstrated to yield values of energy barriers that are closer to the experimental results. The interaction between atoms, molecules or surfaces at large separations is well known commonly to be incorrectly described in LDA or GGA, which exclude long-range interactions, such as van der Waals (vdW) forces.[58] Consider, for example, the physisorption of HCl on ice; the physisorption energy is around 0.3 – 0.5 eV.[59] These additional corrections and perhaps the use of more realistic image chains in NEB minimization can yield calculated values that are closer to experimental values.

Notably, sharp STM tips can yield electric fields that are sufficiently strong to break chemical bonds.[60] Additionally, as noted by Boland, at positive sample bias, the interaction of the Si-Cl dipole on Cl/Si(100) with the field effectively reduces the depth of the potential energy well at a dangling bond site, effectively reducing the barrier to Cl adatom diffusion on a clean Si(100) surface.[61] This decrease should be particularly important for sharper tips, which generate stronger fields and field gradients. Even though negative sample bias was applied during observation and small tunneling currents were used to eliminate the aforementioned complications, the possibility that a sharp STM tip may have a partial role in hydrogen diffusion cannot be excluded completely. In view of this possibility, an alternative explanation of the STM observations that is based on the assumption that the electric field (and current) is *not* strong enough to break the Si-H or Si-Cl bond, but is strong enough to lower the energy barriers of DED through intra- or inter-dimer channels should be considered.

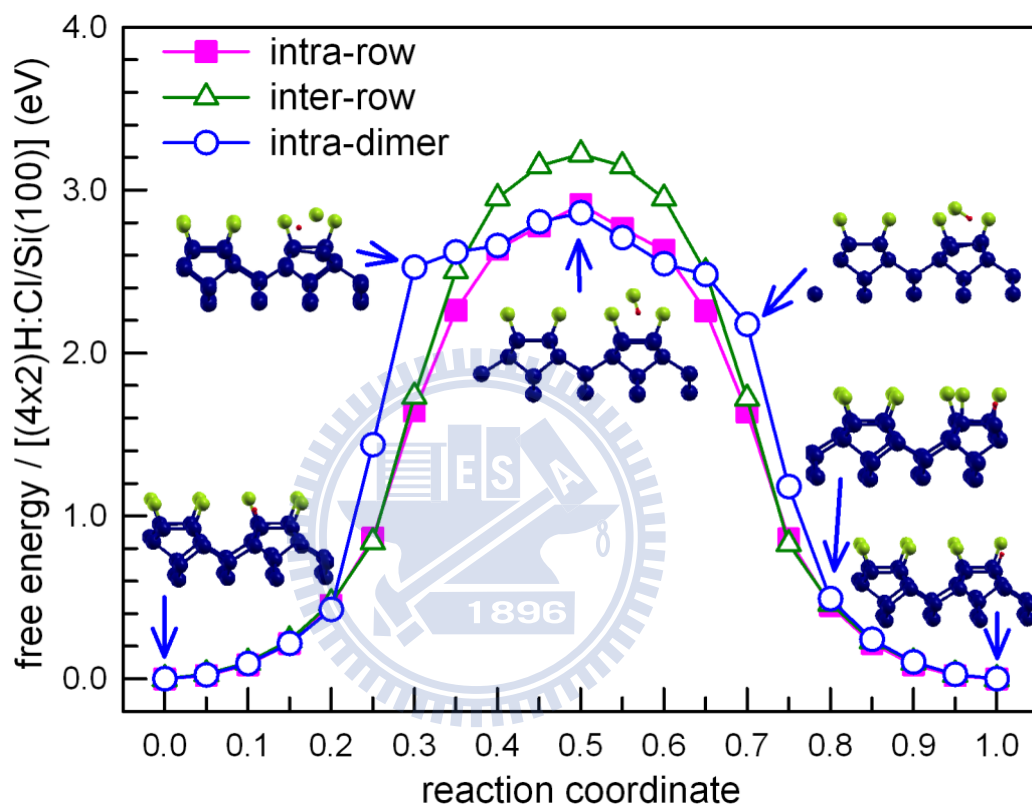


Figure 4.4 Calculated barriers of three direct exchange diffusion channels as labeled. Selective atomic geometries for intradimer diffusion show that the transition-state atomic configuration involves an HCl molecule. Silicon atoms are shown in navy blue; hydrogen atoms are shown in red; chlorine atoms are shown in green.

4.4 Conclusion

Although the concept of DED is known, DED has not experimentally observed to the best of the authors' knowledge. Herein, a detailed atomic view of the diffusion of hydrogen substitution sites within the top chlorine layer on a Cl/Si(100)- 2×1 surface was presented. Atomic-resolution STM images show that hydrogen diffusion occurs via direct positional exchange of an H-site and a neighboring Cl-site in the same row. Analysis of time-lapsed movies indicates a thermally activated process with a barrier of $E_a = 1.29$ eV and an apparent prefactor ν_0 of 1.31×10^9 s $^{-1}$ for intra-row diffusion and $E_a = 1.17$ eV; $\nu_0 = 6.64 \times 10^7$ s $^{-1}$ for intra-dimer diffusion. The energy barriers are substantially lower than expected, perhaps because the DED process involves an intermediate HCl molecular state. Energy calculations based on density functional theory verify the existence of this transition state molecule, but yield higher barriers of around 2.86 eV. The discrepancy in activation energy suggests that corrections such as dispersive forces are required in the calculation. Alternatively, a multiple-step process or the electric field under an STM tip may be involved in the exchange of positions. Our findings suggest the need for further study of the apparent DED process and open the way to further experimental investigations and theoretical calculations of the diffusion processes.

Chapter 5 Repulsive interactions of adsorbed Cl atoms in HCl dissociative adsorption of Si(100)-2×1

This study investigates the surface chemistry and the ordering characteristics of coadsorbed hydrogen and chlorine atoms, generated by the exposure of the Si(100) surface to gas-phase HCl molecules at various substrate temperatures, by scanning tunneling microscopy (STM), core-level photoemission spectroscopy, and simulation. Experimental results show that saturation exposure to HCl causes all surface dangling bonds to be terminated by the two fragment H and Cl atoms and that the number of H-termination sites exceeds that of Cl-termination ones by >10 %. This finding suggests that, in addition to the dominant dissociative chemisorption, many abstraction reactions occur. STM images reveal that Cl-termination sites form local 2×2 structure at 110 K and that the degree of ordering is reduced as the substrate temperature increases. Simulation results demonstrate the importance of including dissociative fragment-adsorbates interactions during the random adsorption of diatomic molecules. Comparing the Cl-termination sites identified from STM images and those predicted by simulation reveals two interaction potentials of 9 ± 1 and 4 ± 1 meV between a dissociative fragment Cl atom and a nearest neighboring Cl-adsorbates in the same dimer row and in the adjacent row, respectively.

5.1 Introduction

Adsorbate-substrate interactions (ASIs) and adsorbate-adsorbate interactions (AAIs) are of great importance in a large variety of fundamental and technical areas in surface science, thin film growth, heterogeneous catalysis, and chemical sensing.[62] When impinging on a surface, a molecule/an atom interacts with the substrate, and the interaction energy between the substrate and the molecule, or the adsorbate, determines the type of reactions that occur. Once adhered to the surface, the adsorbate can interact with another directly by electrostatic repulsion owing to their charges,[63] or indirectly mediated by substrate reconstruction,[64] lattice strain,[65] or surface states.[66, 67] AAIs are typically weaker than ASIs, but can lead to reconstructions or pattern formations on surfaces.[68] AAIs also change the sticking probabilities of molecules and the diffusivities of adsorbates.

Often omitted in discussions of a surface process is that the single term “adsorbate” in AAIs and ASIs can refer to several species. For example, multi-atomic molecules may dissociate into their constituent fragments when they impinge on a surface.[13] In a simple

case, the two separated fragments of a diatomic molecule, AB, react with the substrate and form two new bonds, A-Su and B-Su (where Su denotes the surface), in a reaction that is called dissociative chemisorption. Else, one of the dissociated fragments forms a single bond A-Su and the other B is ejected back to the gas phase; this reaction is called abstractive adsorption. Before A-Su or B-Su bonds are formed, fragment A or B can readily interact with not only the substrate but also other fragments and adsorbates, which are previously adsorbed fragments. When a chemisorption process is complete, the fragment-fragment or fragment-adsorbate interactions become AAIs. Strong effective repulsive forces have been found to exist between two dissociated fragments by observing the well-separated pair-wise adsorption of diatomic molecules and by examining the empirical “eight-site rule” that excludes the adsorption of the second atom of a dissociated molecule at the eight neighboring sites.[13] Since this effect is a transient, many-body effect, however, quantitative information on the fragment-fragment or fragment-adsorbate interactions is difficult to obtain.

This investigation examines the temperature-dependent ordering characteristics of mixed adsorbates and the energies of interaction between adsorbates and a dissociated fragment are determined experimentally for the first time, to the best of the authors' knowledge. Specifically, both synchrotron-radiation core-level photoemission spectroscopy and STM are used to observe mixed H- and Cl-terminated Si(100) surfaces that are saturated by gaseous HCl. The chemisorption and interaction Cl- and H- containing molecules on Group IV semiconductor surfaces are of great technological importance in the semiconductor industry.[69] HCl gas has been commonly applied in reduced-pressure chemical vapor deposition (CVD) to grow Si, Ge and GeSi alloys.[3] HCl chemistry is also important in the etching of silicon.[4] Both theoretical and experimental studies of the adsorption of HCl on Ge(100) and Si(100) surfaces have been performed.[70-73] HCl molecules are suggested to dissociate upon collision with the Si(100) surface. Each of the two dissociation fragments subsequently terminates one surface dangling bond. In this work, Cl-terminated sites are found to form local 2×2 structure and zigzag chains. The degree of Cl-adsorbate ordering increases as the substrate temperature declines, suggesting a kinetic origin of adsorption of fragment Cl atoms. Introducing repulsive interaction energies between the fragment Cl atoms and the nearest neighboring Cl-adsorbates in the simulation yields distributions of the adsorbed Cl and H atoms that resemble closely those obtained from STM images.

5.2 Experiment Details

A core-level photoemission experiment was performed at the Synchrotron Radiation Research Center in Taiwan. It involved a μ -metal-shielded ultrahigh vacuum (UHV) chamber with a base pressure of 1×10^{-10} torr. Light from the 1.5 GeV storage ring was dispersed by a spherical grating monochromator (SGM). The photocurrent from a gold mesh positioned in the synchrotron beam path was monitored to measure the relative incident photon beam flux. Photoelectrons were collected at 45° from the surface normal and analyzed using a 125 mm hemispherical analyzer. The overall energy resolution was better than 120 meV. In decompositions of core level spectra, all fittings were least-squares fittings and each component that consisted of a pair of spin-orbit split doublets, was assumed to have the same Voigt line shape. The STM experiments were conducted in another UHV chamber. All images were recorded in constant current mode at room temperature. Low tunneling currents (240 pA or less) were used.

The Si(100) samples were sliced from doped antimony with a resistance of about 0.01 Ω -cm. They were outgassed at ~ 800 K over 16 hours under UHV conditions. Clean Si(100) surfaces were prepared by direct Joule heating at ~ 1400 K. The substrate was heated by passing a controlled DC current directly through the sample. In the adsorption experiment at low temperature, the substrate was cooled to 110 K using liquid N₂. The substrate temperature T_s was measured post-facto using a type-K thermocouple that was attached using epoxy to the front of the sample; the results were reproducible to within 15 K. The Si(100)-2 \times 1:H monohydride surface was prepared by 600 K saturation exposure of the clean Si(100) surface to atomic H. Atomic hydrogen was produced by backfilling the chamber in the presence of a hot tungsten filament at ~ 5 cm away from the sample. The Si(100)-2 \times 1:Cl monochloride surface was prepared by 300 K saturation exposure of the clean Si(100) surface to Cl₂. Ultra-pure Cl₂ and HCl gases were introduced into the chamber through precession leak valves and stainless steel tubes that face the samples. During Cl₂ and HCl exposure, the chamber background pressure was about 5×10^{-9} torr. The typical dosing time was 60 s.

5.3 Results

The clean Si(100) surface consists of rows of dimers (-Si-Si-), in which each atom has a dangling bond. Saturation exposure of a clean Si(100) surface to Cl₂ and H atoms on at appropriate conditions is known to cause all dimer dangling bonds to become terminated by those atoms while preserving the backbone dimer structure, yielding a Si(100)-2×1:Cl monochloride surface and a Si(100)-2×1:H monohydride surface, respectively.[9, 32] The building blocks of the Si(100)-2×1:H surface and the Si(100)-2×1:Cl surface are a monohydride dimer (H-Si-Si-H) and a monochloride dimer (Cl-Si-Si-Cl), respectively, as shown in Fig. 1.14(a). Accordingly, the co-existence of H and Cl on the clean Si(100) surface, following either co-adsorption or sequential adsorption of the two atoms, can yield mixed H-Si-Si-Cl surface species, in addition to H-Si-Si-H and Cl-Si-Si-Cl.

5.3.1 Photoemission results

Figure 5.1(a) displays Cl 2*p* core level spectra (circles) of the Si(100)-2×1:Cl surface and the Si(00):HCl surface that are obtained by saturating the clean Si(100) surface with Cl₂ and HCl at $T_s = 300$ K. The two Cl 2*p* spectra each have only one component, consisting of a pair of 1.60-eV spin-orbit-split peaks, and are similar in energy and line shape but different in intensity. These observations suggest that each dissociated Cl atom from HCl reacts with a surface dangling bond, forming a Si-Cl bond and a Cl-terminated site (Cl-site).[30] The intensity ratio of the two Cl 2*p* spectra is 0.44. The Si(100)-2×1:Cl surface has nominally 1 ML of chlorine atoms (1 ML = 6.78×10^{14} cm⁻²). Therefore the Cl coverage of the 300 K Si(100):HCl surface is approximately 0.44 ML. This value is less 0.5 ML, which is expected if all HCl is dissociatively chemisorbed. H atoms terminate the remaining ~0.56 ML dangling bonds, as the Si 2*p* spectra and STM images (to be discussed in Sec. IIIB) show. Accordingly, a certain percentage of HCl appears to be abstractively chemisorbed on Si(100) during the passivation process and Cl is preferentially ejected back into the vacuum.

The Si 2*p* spectra and fits to constitutional components of the Si(100)-2×1:Cl surface, the Si(100):HCl surface, and the Si(100)-2×1:H surface are depicted in Fig. 5.1(b). The bottom Si 2*p* spectrum of Si(100)-2×1:Cl has two components, B and T_{Cl}, separated by about 0.92 eV. The B component is responsible for emission from the bulk and the T_{Cl} component is from the topmost 1 ML Si, each Si atom is terminated by Cl. Similarly, the top Si 2*p* spectrum of Si(100)-2×1:H consists of two components, B and T_H, separated by about 0.39 eV. The T_H

component also derives from the 1 ML outermost Si atoms that are now H-terminated and, therefore, the intensity ratio I_{T_H}/I_B of Si(100)-2 \times 1:H is very close to $I_{T_{Cl}}/I_B$ for Si(100)-2 \times 1:Cl. The Si2*p* spectrum of the 300 K Si(100):HCl surface can be analyzed in terms of three components, T_{Cl}, T_H and B. The intensity ratios I_{T_H}/I_B and $I_{T_{Cl}}/I_B$ suggest that the coverages of surface Cl and H are \sim 0.45 ML and \sim 0.55 ML, respectively, in close agreement with those determined from the Cl 2*p* spectra. Sec. IV will discuss the driven force that reduces Cl coverage.

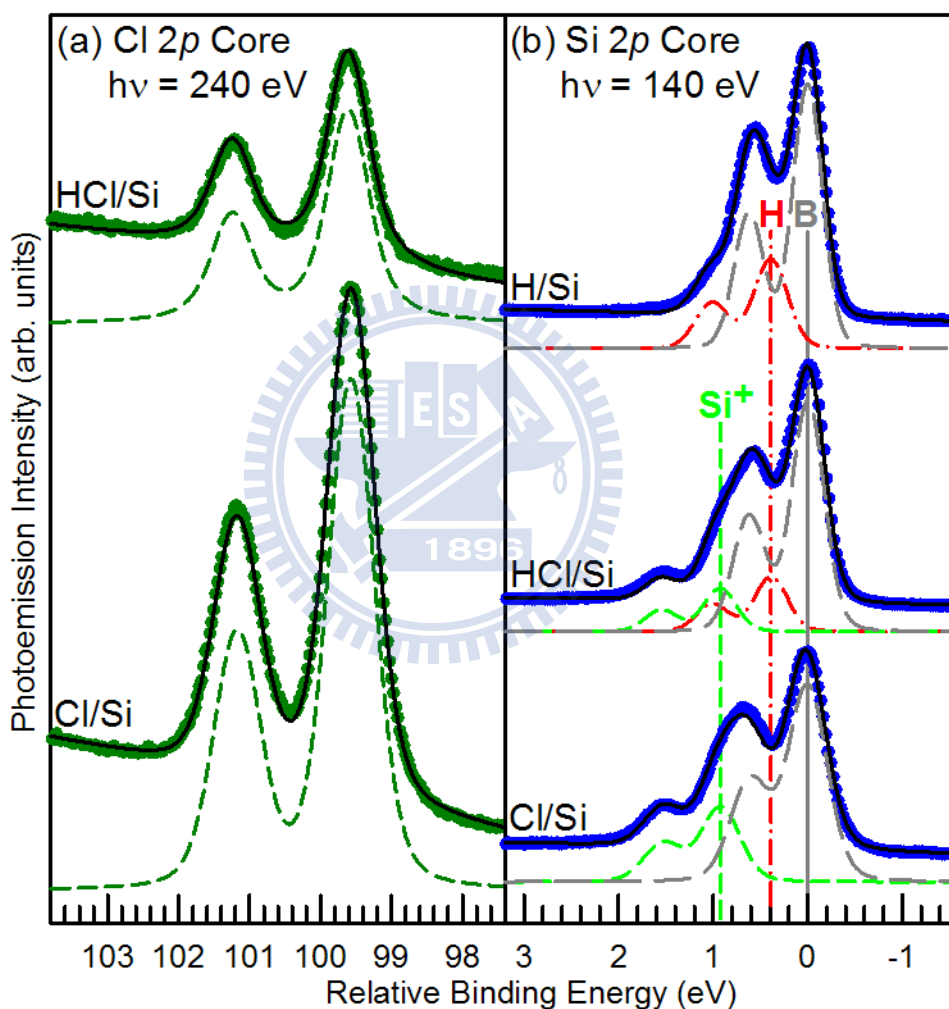


Figure 5.1 The (a) Cl 2*p* and (b) Si 2*p* core level photoemission spectra (circles) for the Cl, HCl and H passivated Si(100)-2 \times 1 surface. The solid curves are fits to the spectra. The curves in (b) labeled B (long dashed), Si⁺ (short dashed) and H (dashed dot) are the results of decompositions of the Si 2*p* spectra from the silicon bulk, Si-Cl and Si-H species respectively. The energy zero refers to the $2p_{3/2}$ bulk position for the Cl-Si(100)-2 \times 1 surface.

5.3.2 STM results

Upon co-adsorption of both H and Cl atoms on Si(100), Cl-terminated sites (Cl-Si species or Cl-sites) appear noticeably brighter than H-terminated sites (H-sites) in both filled and empty-state STM images, as shown in Fig. 1.10(b). In Fig. 1.10(b), the 0.18 ML Cl-sites were produced by exposing to Cl₂ a mostly H-terminated Si(100) surface, in which a portion of dangling bonds were created by mild thermal annealing of the Si(100)-2×1:H sample at ~715 K for 50 s.[11, 12] The adsorption of Cl₂ on an isolated dangling bond or a dangling bond pair of Si(100) has been demonstrated to be mostly abstractive and to be able to cause chain reactions:[11, 13] the Si dangling bond abstracts one atom of the incident Cl₂ molecule while the complementary Cl atom is scattered away from the initial abstraction site. The complementary fragment Cl atom may be captured by a second dangling bond and adsorbed there, or may react with a nearby H atom to form HCl that is scattered away from the surface, leaving a new dangling bond for subsequent Cl₂ adsorption. The complex adsorption processes of Cl₂ produces large amounts of mixed Cl-Si-Si-H species even though brief thermal annealing yields more paired dangling bonds (-Si-Si-) than unpaired dangling bonds (-Si-Si-H).

Figures 5.2(a-c) show the STM images of Si(100) after HCl has saturated the initially clean surfaces that were kept at 110 K, 300 K and 450 K, respectively. Many bright protrusions can be discerned in the images; they are Cl-sites. The H-sites are not well-resolved, but their termination of dangling bonds (DBs) between the Cl-sites is evident and clearly revealed by the Si 2*p* spectra as discussed in Sec. IIIA. The coverages of Cl-sites, 0.42, 0.46, and 0.40 ML associated with adsorption at 110, 300 and 450 K, respectively, vary slightly and are in reasonable agreement with those obtained from the photoemission measurements at RT, mentioned above. A previous study using Auger electron spectroscopy reports an even lower Cl-coverage (0.25 ML at $T_s = 100$ K) and suggests that a self-site-blocking effect causes some DBs inaccessible for HCl adsorption.[73] However, no residue DBs are observed in Figs. 5.3(a-c).

In Fig. 5.2(a), many Cl-sites collectively form zigzag chains and areas of well-ordered 2×2 structure. Since the ratio of the Cl to H coverage is roughly 1:1, a zigzag-structured chain is an ordered array of Cl-Si-Si-H mixed-hydrides dimers, in which H-sites and Cl-sites in neighboring dimers are anti-phase with each other. The 2×2 structure can be regarded as a

combination of more than two neighboring zigzag Cl-Si-Si-H chains with Cl-sites arranged in phase. Restated, each of the Cl-site in 2×2 areas is surrounded by four H-sites, suggesting that Cl-sites effectively repel each other. Figure 5.2(b) shows that the phase correlation of the zigzag structure both in a row and between rows is reduced upon adsorption at room temperature, yielding only short zigzag chains. At elevated substrate temperature, STM images such as Fig. 5.2(c) show no apparent ordering of Cl-sites. Sec. IV presents a detailed analysis of the correlation between adsorption sites.



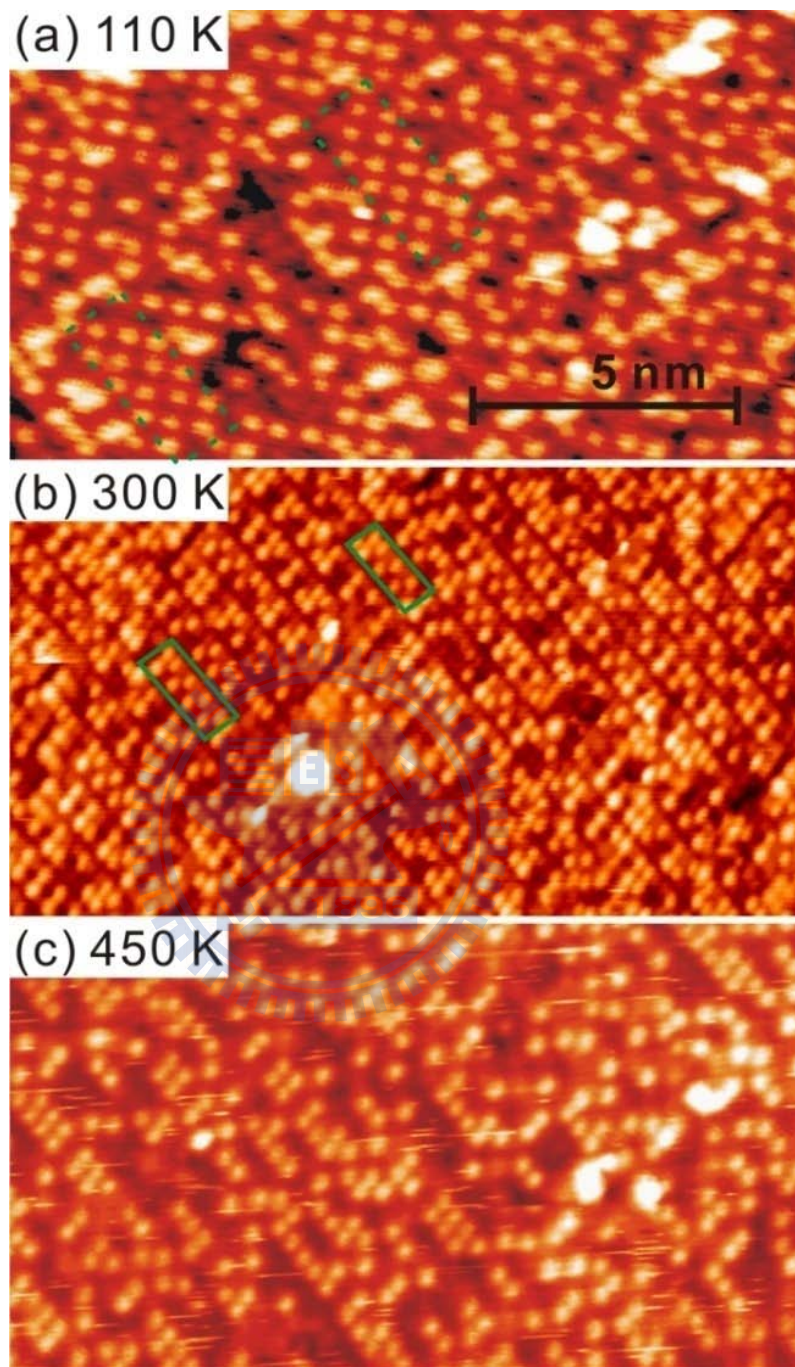


Figure 5.2 STM images of Si(100) after saturation dosage of HCl is applied at sample temperature of (a) 110 K, (b) 300 K and (c) 450 K. Dashed and solid boxes enclose selected areas with a 2×2 and a zig-zag structure, respectively. All images are obtained at room temperature with $I_t = 0.24$ nA and $V_s =$ (a) -2.46, (b) +2.27 and (c) +2.57 V. Image size: $15 \text{ nm} \times 8.5 \text{ nm}$.

5.4 Discussion

5.4.1 H-abstraction reaction

As mentioned in previous sections, both STM and photoemission data show that the DBs in the clean Si(100) surface are completely terminated by either H or Cl after HCl passivation adsorption and that the number of H-termination sites exceeds the number of Cl-termination sites. These findings can simply be explained by assuming an additional adsorption pathway of H surface abstraction beside the dissociative reaction. The relevant bond energies during HCl adsorption on the Si(100) surface are 3.81 eV for Si-Cl, 3.18 eV for Si-H, and 4.28 eV for H-Cl. Thus, the energy released during dissociative adsorption suffices to break the HCl bond ($3.81+3.18 > 4.28$) while that released by H-abstraction or Cl-abstraction does not ($3.18, 3.81 < 4.28$). Therefore, abstracted adsorption is not thermodynamically favorable to occur spontaneously and requires the external addition of energy from the surface.

When the total coverage of H- and Cl-sites is far from saturation of 1 ML, few isolated DBs are present on the surface; the dissociative mechanism can occur spontaneously and should predominate. The number of isolated DBs increases as the total H- and Cl-terminated sites cover more than ~ 0.7 ML because of random adsorption. Each isolated DBs has four neighboring H-sites or Cl-sites. When an HCl molecule comes near and interacts with an isolated DB, a precursor state that involves the DB, the HCl molecule and a neighboring H-site (or a Cl-site) may be formed. Upon thermal excitation, the HCl molecule in this precursor state dissociates with one of the two fragment atoms chemisorbed and the other desorbed into gas phase, completing the surface abstraction. In this suggested scenario, abstraction adsorption occurs via a two-step process and at high coverage. While the measurements in this work reveal the H-abstraction reaction, the details of the reaction process will be elucidated by further experimental and theoretical studies.

5.4.2 Correlation of Cl-occupancy between two adsorption sites

As described in Sec. IIIB, STM images show apparent local ordering of Cl-sites. Correlation functions for adsorption sites of one fragment are required to describe the partially ordered adsorbate layer[65, 74] because the HCl-saturated surfaces are formed by mixtures of adsorbed H and Cl atoms. Twenty sites that surround a centered adsorption site (labeled 0) on a Si(100) lattice with a dimerized structure are first indexed using an integer s ,

as shown in the inset in Fig. 5.3(a). Mirror symmetry sites, such as 2 and 3, 5 and 6, 7 and 8, are indexed in sequence. Consider an i th Cl-site on an STM image of the Si(100):HCl surface and label this site with the index 0. The site occupancy $n_i(s)$ is 1.0 if site s is also a Cl-site; otherwise $n_i(s) = 0$. The “unnormalized” pair correlation function $g'(s)$ of all Cl-sites is defined as

$$g'(s) = g(s)\theta = \frac{1}{N} \sum_{i=1}^N n_i(s) \dots\dots\dots(5.1)$$

where N is the total number of Cl-sites in the STM image and θ is the coverage of the Cl-sites, or the average Cl occupancy at any site in the image area. The use of g' here, instead of the normalized pair correlation function g , [14] is to preserve in the figures the total Cl-coverage θ , which is also an important parameter for understanding the adsorption process. From the definition, g at a certain site s can be interpreted as the ratio of two probabilities: it is the probability of finding a Cl-site, or the Cl occupancy, at site s divided by the average occupation probability θ . The unnormalized pair correlation function $g'(s)$ measures the correlation between occupancy at site s and that at the i th Cl-site ($s = 0$). If $g'(s)$ is equal to the mean occupancy θ , then no correlation exists between sites s and site 0. If $g'(s)$ is larger (smaller) than θ , then the i th Cl-site increases (reduces) the Cl occupancy at site s , which is positively (negatively) correlated with site 0. From STM images in Figs. 3(a-c), the g' for each s can be calculated using Eq. (1); Figs. 5.3(b)-5.3(d), respectively, plot the results. To clarify the correlation between the Cl-occupancies of the two neighboring sites, the pair correlation function g' for each site is also represented on a gray scale in the insets in Figs. 5.3(b)-5.3(d). As displayed in Fig. 5.3(b), the Cl occupancy of sites that are separated by more than two units of the lattice constant, such as $s = 15$ to 20, has a background value of 0.42, which is the mean Cl occupancy, θ . The occupancies for the three nearest neighboring sites, which are indexed 1, 2, and 3, are markedly lower than θ , but noticeably higher for $s = 5, 6, 9, 10$, which are all two single-lattice jumps away and in the same row as $s = 0$.

Figure 5.3(c) plots results concerning room-temperature adsorption. They reveal essentially the same trends: the g' values at sites within two units of the lattice constant ($s = 1$ to 12) deviate from the mean occupancy, but with a lower variation than those in Fig. 5.3(b). For the 450 K Si(100):HCl surface, the variations of g' are even smaller, except at $s = 1$, where the probability of finding a second Cl-site on the same dimer as the first Cl-site is less than 20% of its average value. Since the two sites $s = 0$ and 1 are located on the two sides of

a dimer, the negative correlation between Cl occupancy of the two sites at elevated temperature suggests that Cl-Si-Si-H thermodynamically favored over the monochloride and monohydride dimers.

Since Cl-sites on the 110 K Si(100)-2×1:HCl surface have a higher degree of ordering than those obtained at higher T_s , the following discussion focuses on low-temperature adsorption in the following discussion. In the inset in Figs. 5.3(b), the sites farther from a central Cl-site are moderately grey, corresponding to average occupancy. Sites 1, 2, and 3 are darker, indicating their statistically lower Cl occupancy probability and therefore higher H occupancy. The occupancy of the other immediate neighbor, site 4, is only slightly lower than the average, suggesting that the site correlation is weaker in the neighboring row than that in its row. The higher probability of H-termination at sites 1-3 indicates that, once the dangling bond at site 0 collects the Cl atom from HCl, the complimentary H atom prefers a nearest neighboring site in the same row and/or dissociated Cl atoms dissociated upon subsequent impingements of HCl on these three nearest neighboring sites are driven away. The second nearest neighbors in the same row, sites 5 and 6, have moderately higher occupancy; this result is consistent with the formation of short zigzag chains.

5.4.3 Simulations of ordered structure of adsorbates and fragment-adsorbate interactions

Saturation of Si(100) by HCl consists of a sequence of kinetic events. To analyze the pair correlation functions extracted from the STM images, random adsorption simulations were performed. In the simulations, on a Si(100)-2×1 lattice, a dangling bond that is hit by an HCl molecule, which dissociates, is randomly selected; one of the two separated atoms (referred to as the first atom “A”) is chemisorbed. If a randomly selected site at non-zero coverage already has a previously adsorbed H or Cl adatom, then no adsorption is allowed and a new site is chosen randomly. The second atom (referred to as “B”) is assumed to land with equal probability at one of three immediately neighboring vacant sites on the same dimer row, because the correlation of occupancy between sites in the same row is markedly stronger than that in adjacent row, as discussed in Sec. IVA. The simulation based on this assumption is referred to as Program I. Atom B arguably has a significant probability of reacting with a DB in the neighboring row (site 4). Program II thus randomly selects one vacant site among sites

$s = 1-4$. If the immediate neighboring sites are all occupied, then Program I (II) randomly selects one vacant site among the second nearest neighbors $s = 4-8$ (5-8). At high enough coverage, all eight sites ($s = 1-8$) can be occupied. In this case, both programs assume that an A-abstraction reaction occurs and B cannot be adsorbed. Without the abstraction reaction, ~10% of surface dangling bonds will be left unoccupied,[75] in contradiction with the STM and photoemission observations. Based on these assumptions, Programs I and II generate the arrangement of H- and Cl-sites, as displayed in Fig. 5.3(a). The corresponding g 's can thus be calculated from the simulated arrangement, and the results are as displayed in Fig. 5.3 (a).

Figure 5.3(a) shows that the final Cl coverage is 0.5, even though the simulation programs indicate that about 8.3% of adsorption reactions are abstractive, because the programs include no atomic selectivity for H and Cl. Program I (II) results in lower values of g ' for $s = 1-3$ (1-4), because the complementary fragment B atom (H) initially seeks dangling bonds that are immediate neighbors to A (Cl). The occupancy of all other sites is approximately 0.5, indicating no correlation between sites 0 and s . These results from the simulation clearly agree poorly with the experimental data.

Once formed, H- and Cl-sites on the silicon substrate are immobile at RT or below, because of large diffusion barriers. Thus, the correlation between Cl adsorption sites is established during the adsorption process and before the formation of Cl-Si bonds. Hence, a force is already present before the separated Cl atom is adsorbed. Based on the assumption of the fragment-adsorbate interactions are short-range, the forces between a fragmented Cl atom at sites 0 and a Cl-site at $s = 1-4$ can be described by positive interaction potentials, V_{01} , V_{02} , V_{03} , and V_{04} , respectively. Between Cl- and H-sites, the interaction energy is negligible. The effective substrate potential V_{eff} experienced by the cleaved Cl atom that arrives at a DB ($s = 0$) is the sum of the four energies V_{0i} ($i = 1-4$). When an HCl molecule impinges on site 0, the Cl occupation probabilities should be Boltzmann distributed according to

$$P_{Cl} = R_{Cl} \cdot e^{-\frac{V_{eff}}{kT}} = R_{Cl} \cdot e^{-\frac{V_{01}+V_{02}+V_{03}+V_{04}}{kT}} \dots\dots\dots(5.2)$$

where R_{Cl} indicates the initial probability of Cl adsorption on a DB and is 0.5, assuming no atomic selectivity. Equation (5.2) thus suggests a reduced probability from R_{Cl} of Cl abstraction at a dangling bond site which has one to four nearest neighboring Cl-sites and, therefore, a lower coverage θ and a lower Cl occupancy at $s = 1-3$.

Since the g 's for $s = 1-3$, which are located in the same dimer row, are similar, Program I equalizes the potentials $V_{intra} = V_{01} = V_{02} = V_{03}$ for simplicity, where V_{intra} denotes intra-row interaction. In the simulation, the reduced factor P_{Cl} is also applied to the adsorption of the complimentary B (Cl) atom if H-adsorption occurs initially. All simulations of HCl passivation processes were conducted on an area with 300×150 dimers (300×300 unit cells). In a quantitative analysis, the g 's obtained from the STM measurement is compared with that from the computer simulations, in terms of the standard deviation σ , which is defined as,

$$\sigma = \sqrt{\frac{1}{n} \sum_{s=1}^{20} (g'_{sim,s} - g'_{exp,s})^2} \dots\dots\dots(5.3)$$

where $g'_{sim,s}$ and $g'_{exp,s}$ are the g 's obtained by simulations and experiment, respectively, for site s and $n = 20$ is the total number of calculated sites. A smaller σ indicates a closer match with the simulation result and the corresponding experimental measurement. Figure 5.5 shows an intensity plot of standard deviation σ using a gray scale for 110 K adsorption, as functions of the repulsion energies V_{intra} and $V_{inter} = V_{04}$, where V_{inter} denotes inter-row interaction. The darker shades indicate lower σ and therefore a better fit. As Fig. 5.5 indicates, the repulsion energies of about $V_{intra} = 8.5 \pm 1$ meV and $V_{inter} = 3.5 \pm 1$ meV give the best fit. The intra-row energy of fragment-adsorption interaction is about 1/3 of that of adsorbate-adsorbate interaction,[76] perhaps because that the Cl fragment is a neutron radical and not yet negatively charged. Using these energies, the distributions of Cl- and H-sites are simulated for adsorption at 110 K, 300 K, and 450 K (not shown) and displayed in Figs. 5.4(b) and 5.4(c). Figures 5.3(a), 5.3(b) and 5.3(c) plot the corresponding g 's. As Figs. 5.3(b) and 5.3(c) show, simulations reproduce well the overall trends in the g 's. Despite the successful reproduction of g 's for $T_s < 300$ K, the simulation results for adsorption at elevated temperature do not agree with the experimental ones, as shown in Fig. 5.3(d). Since H-sites and Cl-sites can diffuse on Si(100) via a couple of pathways with rather low energy barriers and the simulation programs herein do not take into account the effect of diffusion, the simulated adsorbate distributions cannot be compared with the experimental ones. Therefore, the disagreement in g ' at 450 K does not exclude the suggested model that is used in the simulation and is accurate at $T_s < RT$.

Equation (5.2) reveals that the effective substrate potential V_{eff} can reduce the probability

P_{Cl} that a fragment Cl atoms bond with a DB. However, reducing R_{Cl} can lower P_{Cl} as well. As mentioned above, the simulation programs assume that H or Cl is adsorbed with equal probability on a DB that is randomly struck by a HCl molecule, such that $R_{Cl} = 0.5$. Simulations using various R_{Cl} and $V_{eff} = 0$ give rather featureless g 's and large θ , as shown in Fig. 5.6 and, therefore, fail to predict the measurements accurately. Giving the set of the repulsion energies found above, the simulation reproduces the unnormalized pair correlation function g' reasonably well over a large range of R_{Cl} . These findings further explain the presence of the repulsive forces between fragment atoms and adsorbates as well as the repulsion energies found above.



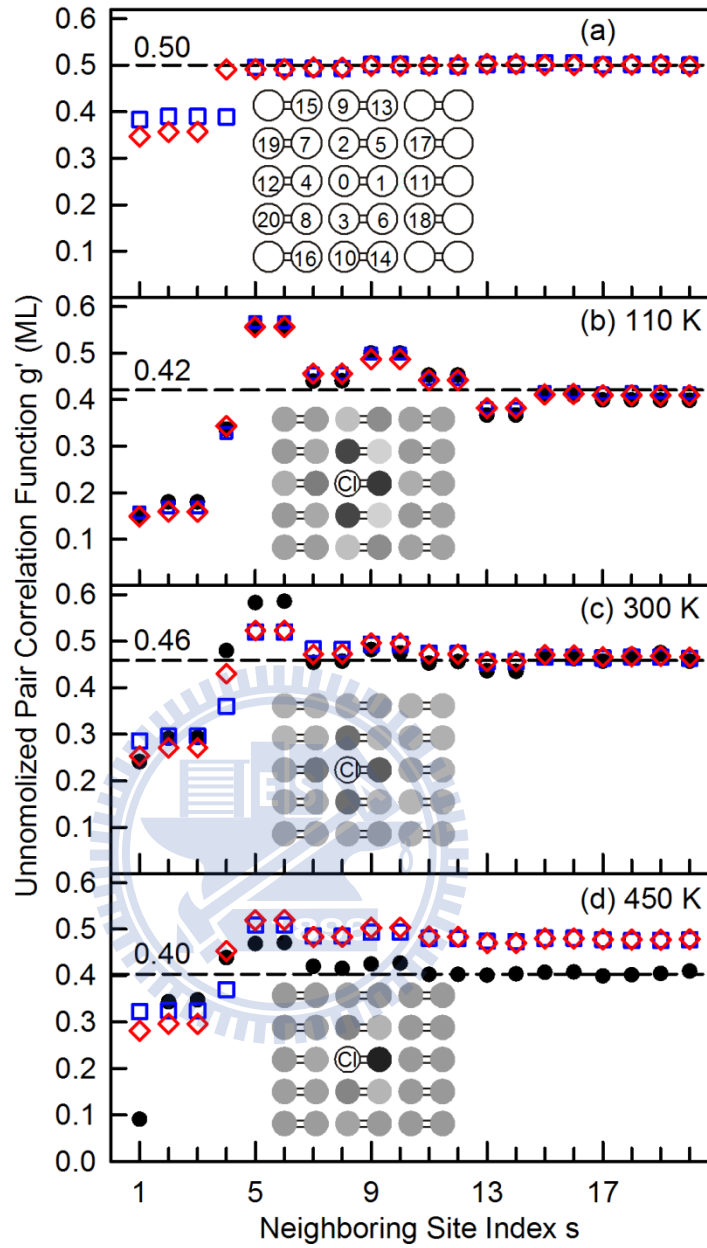


Figure 5.3 Unnormalized pair correlation function g' obtained from simulation (a) Program I (squares) and Program II (diamonds) with a zero fragment-adsorbate energy of interaction; (b-d) simulations with fragment-adsorbate energy of interaction and STM images (filled circles) of the samples in Figs. 5.2(a-c). The repulsive fragment-adsorbate energies used are $V_{intra} = 8.5$ meV and $V_{inter} = 3.5$ meV. The insets in (a) show the lattice of Si(100)-2x1:HCl; each circle corresponds to an H- or Cl-site. Numbers are site index s for sites that neighbor to the central adsorbed Cl atom ($s = 0$). Insets in (b-c) are grey-scale representations of g' .

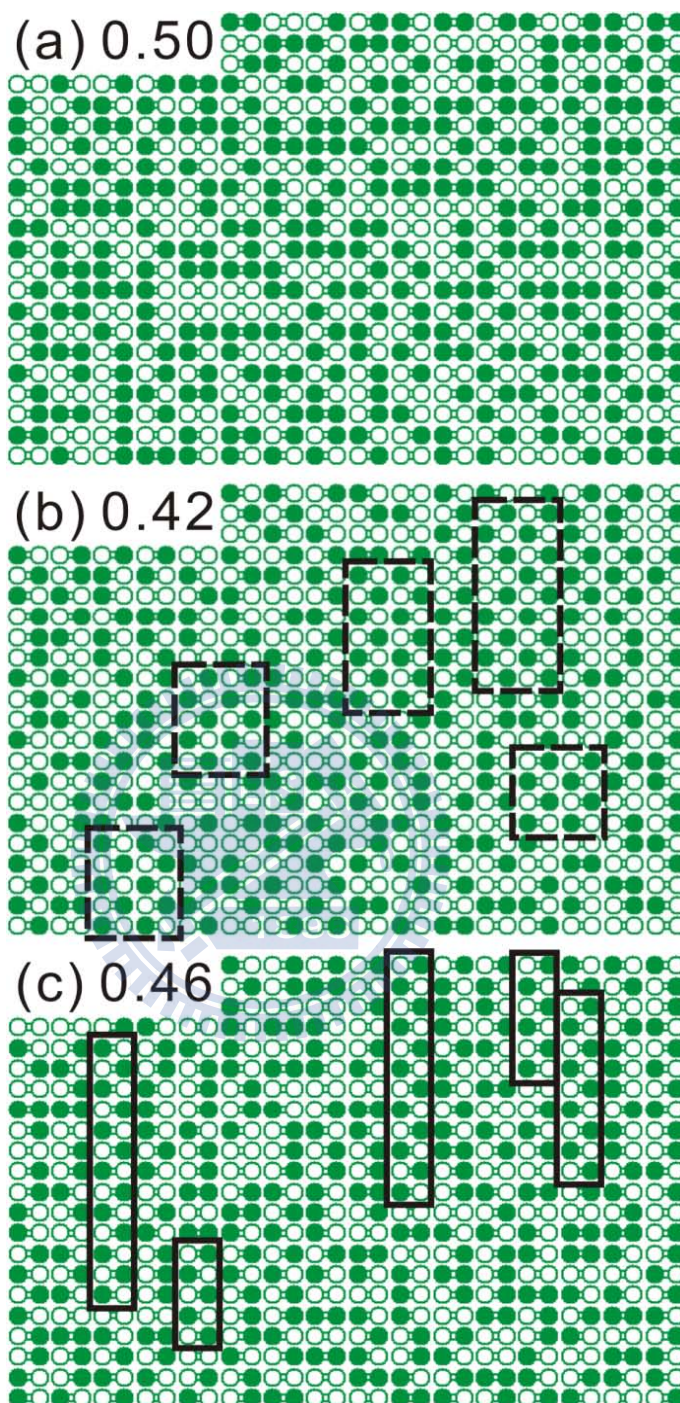


Figure 5.4 Simulated distributions of coadsorbed H (circles) and Cl (filled circles) sites on Si(100)-2 \times 1 at (a-b) 110 K and (c) 300 K. Coverages of Cl-adsorbed sites in monolayer are given. Arrows indicate selective patches of 2 \times 2 structure. In (a) all interaction energies are 0. In (b-c), the repulsive energies are $V_{intra} = 8.5$ meV and $V_{inter} = 3.5$ meV.

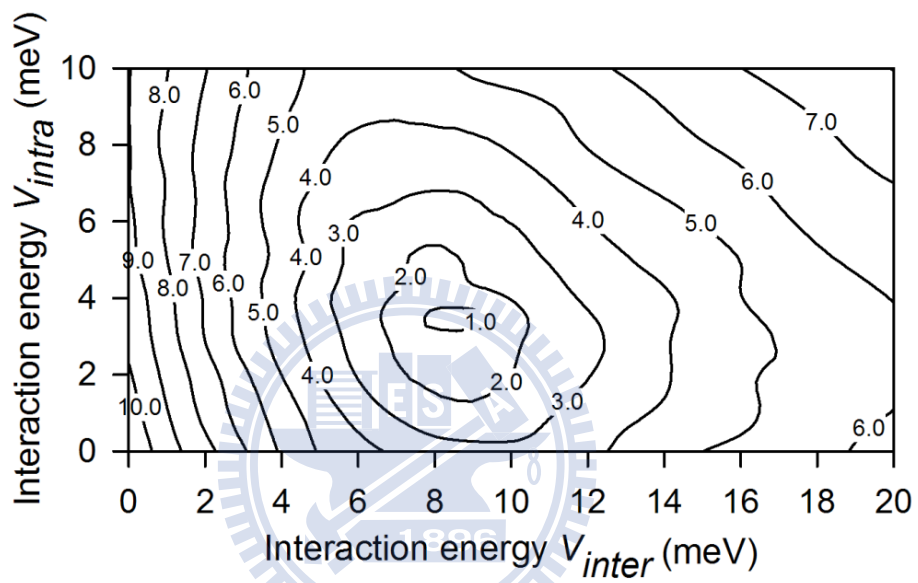


Figure 5.5 Contour representation of standard deviation σ between the simulation and STM result (110 K) as functions of repulsive interacting energies V_{intra} and V_{inter} . Simulated results more closely match STM measurements in darker areas where σ is smaller

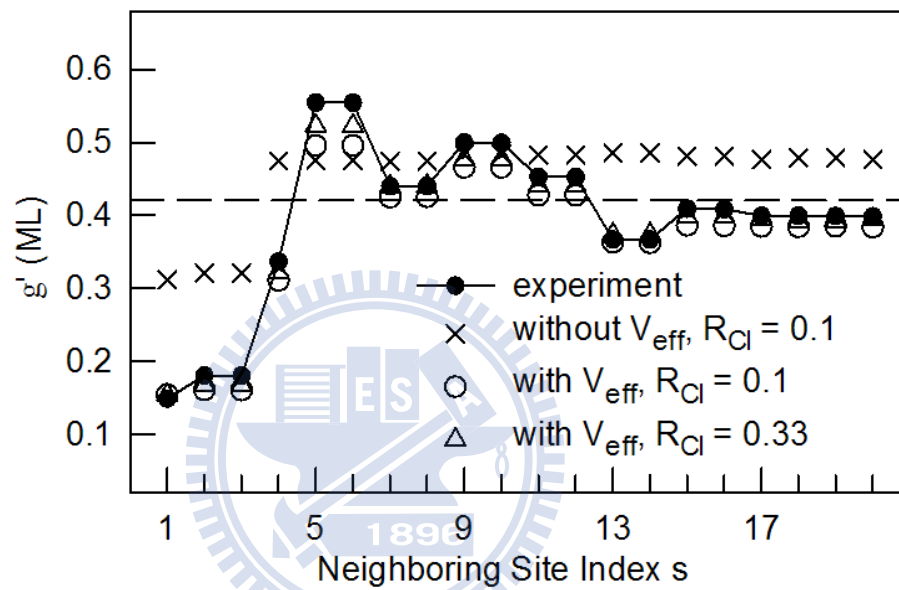


Figure 5.6 Unnormalized pair correlation function g' obtained by Program I, which uses different R_{Cl} values with and without effective substrate potential V_{eff} as labeled.

5.5 Conclusion

This work elucidates the kinetics of HCl adsorption on the Si(100)-2×1 surface by integrating a spectroscopic measurement of core-level photoemission, atomic resolved STM imaging, and computer simulations. Experimental results indicate that the adsorption proceeds by the combination of a dissociative mechanism and surface abstraction in favor of H fragments over Cl. During dissociative chemisorption on surfaces, the fragment-adsorbate interactions are present and change the ordered structure of the adsorbates. Reliable values of the fragment-adsorbates potentials can be extracted by comparing the simulated and measured occupancy pair correlation functions. If a Cl fragment is in same dimer row as another Cl adsorbate, then the energy of their interaction energy (8.5 meV) exceeds that (3.5 meV) when they are in adjacent rows.



Chapter 6 Conclusions

We have studied the interactions of hydrogen (H) and chlorine (Cl) on Si(100) surface by high-resolution core-level photoemission with synchrotron radiation, scanning tunneling microscopy, and computer simulations. The clean Si(100) surface consists of rows of dimers, where the two dangling bonds from the two Si atoms in a dimer form a weak π bond. When H (or Cl) atoms chemisorbed on a clean Si(100) surface, the surface will preserve the basic 2×1 dimer structure without buckling. We expose Si(100)- 2×1 surface to H, Cl and HCl respectively and focus on the interactions of H and Cl atoms on silicon surface in real time via atomic scale imaging by using STM and also in core-level photoemission and computer simulations. The purpose of our study is to gain a better understanding and further insight in the microscopic dynamical behavior of surface interactions.

The gas surface reaction $H_{(g)}+Cl_{(ad)}/Si(100)$ is an important exemplary system for the study of the ER, HA, and LH mechanisms. The core level measurement and STM images observed the formation of $SiCl_2$ surface species, indicating that some additional reactions occur beside the removal of Cl upon impingement of H atoms. Analysis of the STM and simulated images shows that the Cl-extracted sites are correlated to the neighboring Cl-extracted sites. These experimental results cannot be explained by the pure Eley-Rideal process with unitary reaction probability. We recognize that other mechanisms, for example, an Eley-Rideal abstraction process with a reaction probability which depends on the local surface coverage of Cl and maybe H, might possibly lead to our results. However, the experiment results indicate that the HA process likely occurs during the atom-atom collision.

A detailed atomic view of the diffusion of hydrogen substitution sites within the top chlorine layer on a Cl/Si(100)- 2×1 surface was presented to investigate the direct exchange diffusion (DED). Atomic-resolution STM images show that hydrogen diffusion occurs via direct positional exchange of an H-site and a neighboring Cl-site in the same row. Analysis of time-lapsed movies indicates a thermally activated process with a barrier of $E_a = 1.29$ eV and an apparent prefactor ν_0 of 1.31×10^9 s⁻¹ for intra-row diffusion and $E_a = 1.17$ eV; $\nu_0 = 6.64 \times 10^7$ s⁻¹ for intra-dimer diffusion. The energy barriers are substantially lower than expected, perhaps because the DED process involves an intermediate HCl molecular state. Energy calculations based on density functional theory verify the existence of this transition

state molecule, but yield higher barriers of around 2.86 eV. The discrepancy in activation energy suggests that corrections such as dispersive forces are required in the calculation. Alternatively, a multiple-step process or the electric field under an STM tip may be involved in the exchange of positions. Our findings suggest the need for further study of the apparent DED process and open the way to further experimental investigations and theoretical calculations of the diffusion processes

The fragment-adsorbate interactions are present and can alter in part types of reactions and lead to different ordered structure of adsorbates during dissociative chemisorption on surfaces. This work elucidates the kinetics of HCl adsorption on the Si(100)-2×1 surface by integrating a spectroscopic measurement of core-level photoemission, atomic resolved STM imaging, and computer simulations. Experimental results indicate that the adsorption proceeds by the combination of a dissociative mechanism and surface abstraction in favor of H fragments over Cl. During dissociative chemisorption on surfaces, the fragment-adsorbate interactions are present and change the ordered structure of the adsorbates. Reliable values of the fragment-adsorbates potentials can be extracted by comparing the simulated and measured occupancy pair correlation functions. If a Cl fragment is in same dimer row as another Cl adsorbate, then the energy of their interaction energy (8.5 meV) exceeds that (3.5 meV) when they are in adjacent rows.

The experimental works in this thesis produce much atomic-scale information of several surface reactions and processes during the coadsorption of two mixed adsorbates on the Si(100) surface. These findings shed new light on interactions of hydrogen and chlorine atoms on the Si(100) surface.

Appendix A Hard repulsive barrier in hot adatom motion after dissociative adsorption of oxygen on Ag(001)

Random pairing simulation and low temperature scanning tunneling microscopy are used to investigate the detailed O₂ dissociative adsorption processes at 200 K for various coverages. The distribution of oxygen adatoms shows a strong repulsion between the adsorbates with a radius of ~0.8 nm. The comparison between STM results and simulation reveals that two prominent pairing distances of 2 and 4 nm and their branching ratio is about 2:1. These findings shed new light on the origin of the large intra-pair distances found and on the process behind the empirical “eight-site rule”.

A.1 Introduction

The adsorption of oxygen on silver single-crystal surfaces has been widely studied in the past decades.[77-82] This interest arises because oxygen chemisorbs on silver systems in both atomic and molecular form and thus allows molecular dissociation to be studied at a fundamental level. Moreover, the silver oxygen interaction is of enormous industrial relevance: It is a familiar catalyst for epoxidation of ethylene to ethylene oxide (EO) ($C_2H_4 + O \rightarrow C_2H_4O$) and the partial oxidation of methanol to formaldehyde ($CH_3OH + O \rightarrow CH_2O + H_2O$).[83, 84] The microscopic understanding of oxygen adsorption and dissociation is a prerequisite to understand the catalytic cycle. Thereby, the distribution of the oxygen atoms as educts for further reactions is of particular relevance. The identification of the catalytically active oxygen species on silver surfaces was consequently the subject of numerous studies.[77, 85, 86] Finally, the oxidation process is interesting, because silver oxide nanoclusters were shown to be potential candidates for optical memories.[87]

Three oxygen adsorbed states of oxygen on Ag(001) were reported: (1) a physisorbed molecular species,[88, 89] (2) a chemisorbed molecular species[79] below 130 K that forms two-dimensional c(4×2) islands,[90] and (3) a dissociative (atomic) chemisorbed oxygen state above 130 K with a very low sticking coefficient S of 7.4×10^{-4} at $T=150$ K and 1.3×10^{-4} at $T=250$ K.[91] After oxygen exposure on the Ag(001) surface at 180 K, LEED measurement exhibited a c(2×2) pattern,[77] and heating from 180 K to room temperature led to a structural transition from c(2×2) to p(1×1). A combined STM, LEED and AES

study revealed the complete complex phase diagram with a variety of different structures depending on partial pressure and temperature.[86]

At very low coverage, Schintke *et al.*[80] first reported hot adatom motion on this surface as obvious from a pairing of O-adatoms over two distinct and large intrapair distances around 2 nm (± 0.4 nm) and 4 nm (± 0.4 nm) after exposing the Ag(001) surface to oxygen at 140 K. These distances correspond to 7 and 14 surface lattice constants (SLCs) of 0.289 nm on Ag(001). There is ample evidence that the oxygen transients are important in a wide range of catalytic surface reactions.[92] Previous STM studies on this topic focused on the pair distribution revealing average intrapair distances that range from ~ 2 to ~ 14 SLCs.[93-96] An effect of the adsorbate-adsorbate interaction on the transient ballistic motions of “hot” adatoms has not yet been investigated.

In this article, we investigate the dissociation of oxygen on Ag(001) at a higher sample temperature of 200 K and a larger coverage of $\sim 1.7\%$ ML, at which the average separation of the atoms is smaller than the pairing distances observed before at 140 K.[80] We compare the distribution of adatoms found in scanning tunneling microscopy images acquired at 5 K to simulations of random pair distributions. A hard repulsive interaction between the oxygen atoms is found to limit the nearest neighbor distance to 0.8 nm. The comparison of simulation and LT-STM results reveals pairing distances of ~ 2 nm and ~ 4 nm with a ration of 2:1. This result sheds new light on the large intra-pair distances found and on the process behind the empirical “eight-site rule”. This empirical rule excludes the adsorption of the second atom of a dissociated molecule at the eight neighboring sites of the first atom.[97]

A.2 Experiment Details

The experiments were performed with a custom-built low-temperature STM in a UHV system with a base pressure below 5×10^{-10} mbar.[98] The single crystal Ag(001) surface is cleaned by cycles of Ar⁺ sputtering (3.7 μ A, 0.55 keV, 25 min) and annealing (900 K, 3 min). We adsorb oxygen from the background pressure measured by a cold cathode gauge close to the gas inlet to 1×10^{-5} mbar and by a hot filament gauge in the main chamber to 2×10^{-6} mbar. The surface is thereby held at (200 ± 5) K. At this temperature adsorption is dissociative.[77] Exposure to 300 L and 900 L O₂ leads to an O coverage of 0.6 % ML and 1.7 % ML, respectively, as determined in the STM. A monolayer refers to the surface density of silver atoms in the (001) plane ($1 \text{ ML} = 1.2 \times 10^{15} \text{ atoms/cm}^{-2}$).

The sample is then transferred into the cold shields of the cryostat, where all STM measurements are performed at 5 K. For image calibration the standard method of atomic resolution of the native surface has been employed. STM images are measured in the constant-current mode at the parameters given in the figure captions. Apart from a plane subtraction and a low pass filter no further image processing has been employed. The conventional grey scale representation implies that depressions/protrusions in the STM image correspond to a reduced/enhanced local density-of-states (LDOS).

Based on comparison to atomic resolution images (see below) the precision of the distance between two atoms is better than 0.1 nm. In order to analyze the distance distributions extracted from the STM images, we performed random pairing (RP) simulations. On a rectangle of the size of the STM image, the program randomly places the number of atoms as determined from the STM images according to the following rules to include the origin of two atoms from one molecule and the repulsion between adatoms. If a randomly selected site for the first oxygen adatom from a pair is less than 0.8 nm away from a previously adsorbed adatom, no adsorption is allowed and a new site is chosen randomly. The previous report for dissociation at 140 K observed a distribution of ± 0.4 nm around the mean distances D . [80] We attribute this distribution mainly to the discrete nature of the adsorption site of the oxygen atom in a four-fold hollow site (see below), which have a maximum distance of $\sqrt{2} SLC = 0.4$ nm in $\langle 100 \rangle$ direction. The distance of the second oxygen adatom released from the O₂ molecule to the first one is thus chosen randomly

between $(D - 0.4)$ nm and $(D + 0.4)$ nm. The direction of the second oxygen adatom traveling away from the first one is also generated randomly. Again, if the second adatom would sit too close to an occupied site (distance less than 0.8 nm), both the distance and the direction for the second adatom are regenerated.

The standard deviation σ is used for a quantitative analysis comparing the results from the STM measurement with those from the computer simulations for variant hypothetical pairing distances. Each simulation data point used for the standard deviation is the average value of 50 simulation runs.



A.3 Results

After exposing the Ag(001) surface to O₂ at 200 K, isolated oxygen atoms are observed as circular depressions with a diameter of ~0.6 nm in the STM image [Fig. A.1(a, b and d)]. In agreement with earlier STM results and Green's function STM image calculations,[90] the depression reflects the reduced LDOS of the four surrounding Ag atoms induced by an oxygen atom adsorbed in a hollow site as compared to the LDOS of the unperturbed Ag atoms. Especially at low coverage, e.g. 0.6% ML in Fig. A.1(a), a pairing of the oxygen adsorbates is obvious. Two main intrapair distances distributed around 2.0 and 4.0 nm (corresponding to about 7 and 14 SLCs) are found, exemplified in Fig. A.1(a) and (b) as ellipse and dashed ellipse, respectively. This qualitative picture is quantitatively confirmed below. Such a pair of atoms originates from the dissociation of a single adsorbing molecule and the subsequent motion of the formed adatoms. Also this observation is in agreement with earlier work[80] performed at lower temperature (140 K) and over a variety of coverages (0.1% – 0.5% ML).

Results obtained by indirect means from high resolution electron energy loss spectroscopy (HREELS) showed an increase in dissociation probability on the stepped Ag(410) surface.[79] If this increase was based on an enhanced sticking probability at step edges, it would imply a larger density of oxygen atom pairs near step edges than on terraces. However, in our STM images, e.g. in Fig. A.1(b), the oxygen atom pairs are evenly distributed over the surface and no preference close to step edges is found. Thus, the higher dissociation probability can not be related to the fact that the oxygen dissociates on Ag(001) only if the molecules are bound to kink sites at step edges. We suggest that the change in electronic structure on small terraces is at the origin of the enhanced dissociation probability on Ag(410).[99]

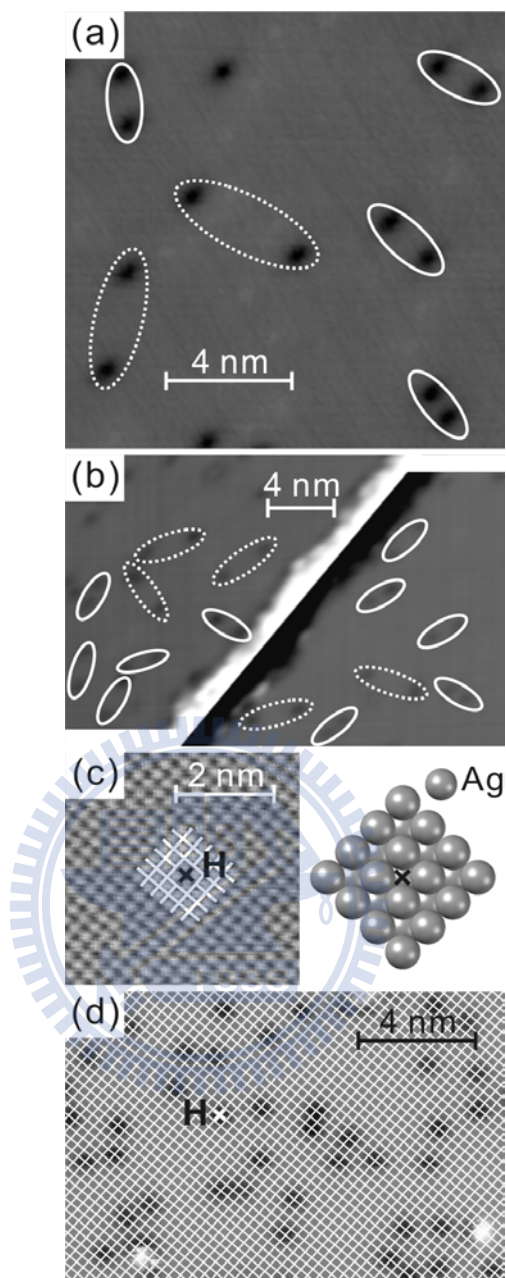


Figure A.1 STM images of Ag(001) surface (a,b) with an O coverage of 0.6 % ML; pairs are marked by ellipses ($V_{tunnel} = -100$ mV, $I_{tunnel} = 10$ pA); image in (b) is split close to the step edge and different contrasts are chosen for the two terraces in order to make the atoms visible on both sides of the step edge (c) native substrate in atomic resolution, ($V = -21$ mV, $I = 4.6$ nA) with ball model showing most stable adsorption site of an oxygen atom calculated in⁴; white lines show lattice intervals (d) STM image of surface with an O coverage of 1.7 % ML; superimposed atomic grid deduced from atomic resolution, ($V = -150$ mV, $I = 78$ pA); crosses in (c) and (d) indicate fourfold hollow site H. (We thank Carsten Sprodowski, Leibniz University of Hannover, for experimental support and for providing Fig. A.1(c))

The atomic resolution of the surface [Fig. A.1(c)] superimposed over an image with oxygen atoms at a larger coverage of ~ 1.7 % ML [Fig. A.1(d)] demonstrates that all atoms are adsorbed in equivalent adsorption sites. According to theory[80] this is the fourfold hollow site [Fig. A.1(c)]. In conclusion, Fig. A.1 demonstrates that at 200 K the oxygen atoms separate in a hot adatom motion after dissociation on the terrace and accommodate in the fourfold hollow site. Here, we investigate their non-thermal motion further at the higher coverage.

At this higher oxygen coverage [see also A.2(a)], the pairing of oxygen adatoms is not as easily revealed because pairs may overlap with others and the oxygen atoms seem to be randomly distributed over the Ag(001) surface. To analyze the oxygen atom pair distribution, we present a 2-D radial distribution plot as shown in Fig. A.2(e) for the STM image in Fig. A.2(a). For this plot we determine for each atom the direction and distance of each other atom within 3 nm. Such a pair is then represented by a dot at the distance from the center of the image in the observed direction. The same distance and direction can of course occur more than once and in the graph the density of a distance/direction pair is visualized by gray levels where darker areas reflect higher densities. Note that in this procedure each distance is counted twice and the pair distribution plot shows an inversion symmetry. The shortest distance of 0.6 nm (about 2 SLCs) is only observed for one pair, otherwise, the pair distances are larger than 0.8 nm (about $2\sqrt{2}$ SLCs), which is shown as a circle of radius 0.8 nm in Fig. A.2(e)-(h). The minimal distance corresponds to the nearest neighbor distance found in a STM study within small islands showing $p(2\times 2)$ superstructure after high dosage of O_2 ($\approx 10^{10}$ L) on the Ag(001) surface at 300 K.[86]

We now analyze the experimental 2-D radial distribution plot by comparing it to simulated distributions. Fig. A.2(b) displays a simulation for a totally random distribution of the same oxygen coverage as in Fig. A.2(a) on the same size of the STM image. Its 2-D radial distribution plot is shown in Fig. A.2(f). This distribution clearly disagrees with the experimental distribution. In particular, the repulsive ring is not reproduced. Therefore, we include a repulsion restricting the distance to 0.8 nm ($\sim 2\sqrt{2}$ SLCs) into the random simulation. The result is shown in Fig. A.2(c). Its radial distribution map in Fig. A.2(g) reproduces the STM result much better.

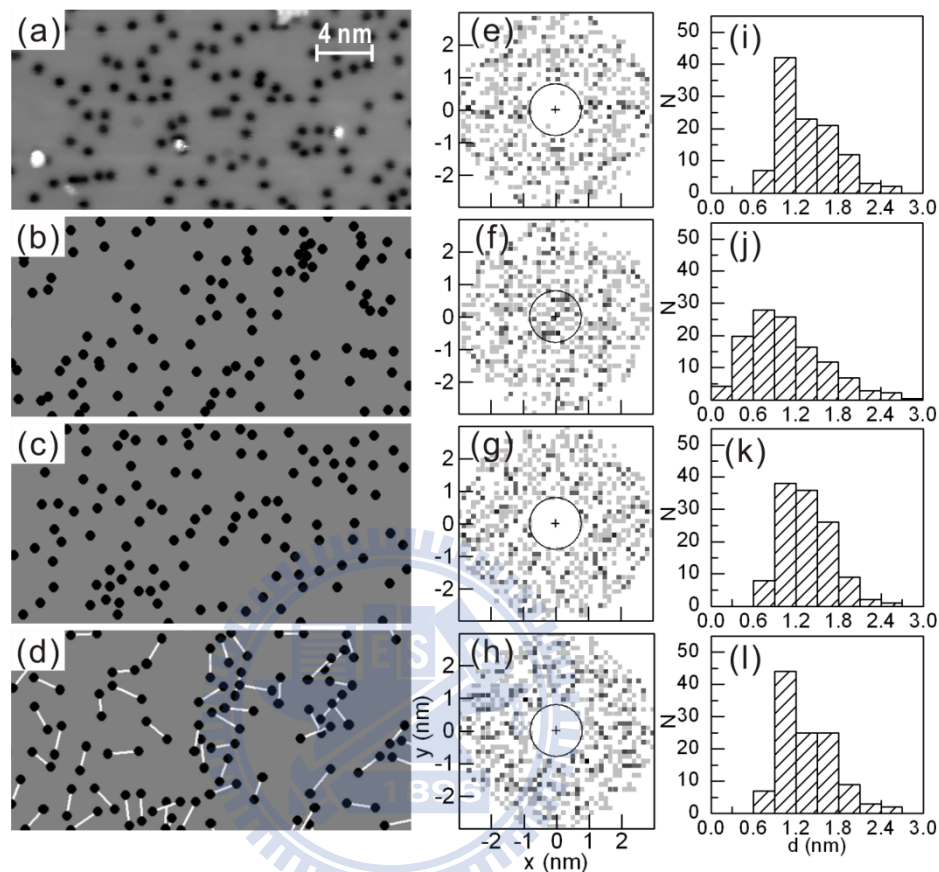


Figure A.2 (a) STM image of the Ag(001) surface with 1.7 % ML coverage ($V = -150$ mV, $I = 78$ pA). (b)-(d) Examples for the simulations with the same oxygen coverage as in (a). (b) Totally random simulation without repulsion. The black dots indicate oxygen atoms. (c) Random simulation including repulsion limiting the nearest neighbor distance to 0.8 nm. (d) Random pairing simulation for pairs with distances of (2.0 ± 0.4) nm with a minimum nearest neighbor distance of 0.8 nm. The white lines connect oxygen atom pairs. (e)-(h) Plot of the two-dimensional pair distribution function within a radius of 3 nm with respect to each atom from (a)-(d). The distance between two pixels is 0.15 nm, about half a SLC, and the radius of small circle is 0.8 nm. (i)-(l) Histograms of the nearest neighbor distance from (a) to (d).

We next discuss whether inclusion of the pairing of the O-adatoms as observed in Fig. A.1 into the simulation leads to an even better mimicking of the experiment. A random pairing simulation with pair distances of (2.0 ± 0.4) nm is shown in Fig. A.2(d), its 2-D radial distribution plot in Fig. A.2(h). It is not obvious, whether this distribution [Fig. A.2(h)] or the one presented in Fig. A.2(g) better reproduces the experimental distribution in Fig. A.2(e).

The directions of the pairs are random and thus we now concentrate on the distances only. Figures A.2(i) to (l) display histograms of the nearest neighbor distance for a measured area of $26 \text{ nm} \times 26 \text{ nm}$ for the experimental and the three simulated distributions shown in Figure A.2(a) to (d) and the same oxygen coverage of 1.7 % ML. Again, the simulation that does not take into account the repulsive ring [Fig. A.2(j)] does not reproduce the experiment [Fig. A.2(i)]. The distribution that considers the repulsive ring only [Fig. A.2(k)] resembles the experiment less well than the one that also considers pairing distances of (2.0 ± 0.4) nm [Fig. A.2(l)]. Therefore, despite the larger coverage the origin of two atoms from one molecule, i.e. the pairing, is still detectable.

For a quantitative analysis, we compare the results from the STM measurement with those from the computer simulations via the standard deviation σ defined as:

$$\sigma = \sqrt{\frac{1}{n} \sum_{i=1}^n (N_{Sim,i} - \overline{N_{STM,i}})^2}$$

where N indicates the number within an interval i for the nearest neighbor distance distribution of the oxygen atoms and n indicates the total number of intervals. The smaller σ the better the STM measurement is simulated. Variant pairing distances (1.0, 1.5, 1.8, 2.0, 2.2, 2.5, 3.0, 4.0, 6.0, 8.0 nm (± 0.4 nm)) and the random distribution are simulated and compared to the related STM data. Figure A.3(a) shows that for pairing distances above 4 nm the pairing distribution cannot be discriminated from a random distribution. Most importantly, the best fit of simulation to STM results is found for pairing distances of $2.0 (\pm 0.4)$ nm.

Finally, we include the larger pairing distance of 4 nm found in Fig. A.1 and also at 140 K into the simulation.[80] Thereby, we vary the ratio of 2 nm to 4 nm pairs. The percentages of 33, 50, 60, 67, 75 indicate that the ratios of 2 nm to 4 nm pairs are 1:2, 1:1, 3:2, 2:1, 3:1, and 100 % denotes only 2 nm pairs. We caution that with increasing coverage the probability increases that a molecule approaches an adsorption modified surface site and thus may follow a completely different dissociation path, possibly connected with yet another pairing

distance not included in our analysis. As one adsorbed molecule modifies the LDOS of four silver atoms,[80] we estimate this to be an effect of the order of 3 to 4 % for the coverage investigated here. Within this error margin, the comparison of experiment to simulation reveals that the pairing distance has a ratio of 2:1 for 2 nm to 4 nm pairs [Fig. A.3(b)].

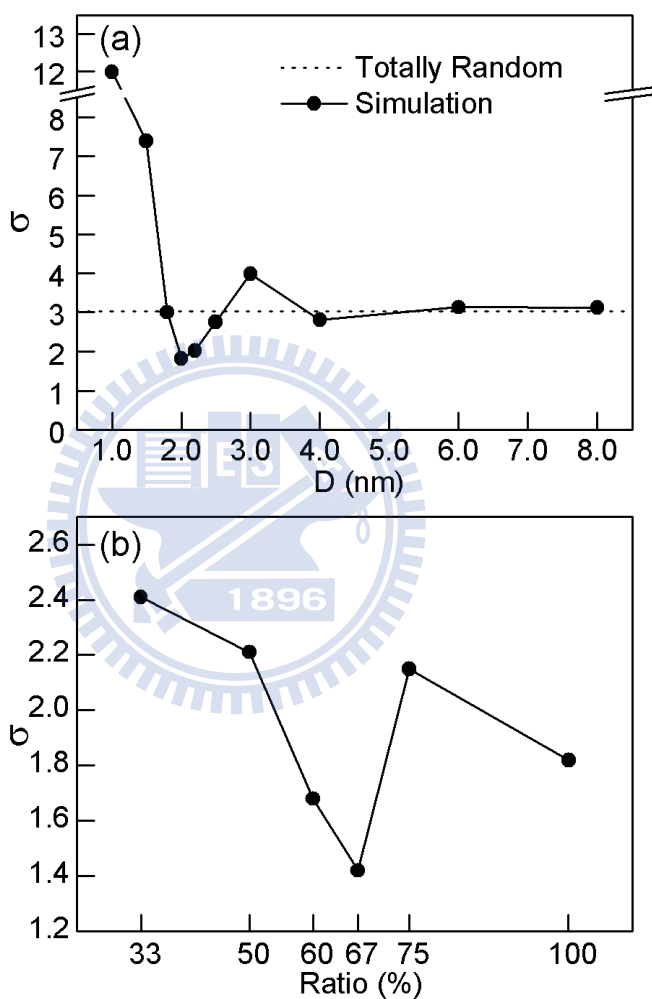


Figure A.3 Standard deviations σ of nearest-neighbor distances of RP simulation to STM results for different pairing distances: (a) for one pairing distance D (b) in dependence of ratio of 2 nm (± 0.4 nm) to 4 nm (± 0.4 nm) pairs.

A.4 Discussion

On a conceptual level, our study demonstrates that at a coverage, where atom pairs are no longer well separated, the origin of two atoms from one molecule, i.e. the pairing, is still detectable. This extends the possibility of STM to investigate the hot adatom motion beyond single or well separated pairs. Only at this larger coverage the depletion region around each adsorbed atom with no atoms closer than 0.6 nm (about 2 SLCs) and the nearest neighbor distances mostly larger than 0.8 nm (about $2\sqrt{2}$ SLCs) is detectable. Such a depletion region implies repulsion in the adatom interaction. Indeed, DFT calculation showed that a repulsive barrier leads to a saturation coverage of oxygen on silver of 0.24 ML only[100] consistent with $p(2\times 2)$ superstructure found experimentally on Ag(001) at higher coverage.[86] Most likely, such a repulsion results from a partial charge transfer from the surface to the adatoms. A recent DFT study calculated this charge transfer for oxygen molecules in dependence of the work function change upon adsorption for a variety of metals, but not silver.[101, 102] This study allows to estimate this charge transfer to be approximately 0.18 electrons for the molecule on Ag(111). A density functional calculation on Ag(110) suggests also a charge transfer from the metal to the adsorbed oxygen atom.[103] Based on these studies, it is reasonable to assume a partial charge transfer also to the oxygen atom on Ag(001). The origin of the depletion region is thus electrostatic interaction.

Furthermore, the depletion region might also be related to the so-called eight-site rule.[97] The eight-site rule is an empirical rule that excludes the adsorption of the second atom of a dissociated molecule at the eight neighboring sites. A physical explanation for this rule was not provided. Our results suggest that this depletion region is not the result of a separation of the atoms originating from the same molecule. Instead, one of the adatoms is already settled on the surface, the other one is still mobile and is not allowed to approach the adatom too closely because of electrostatic repulsion.

In addition, a repulsive barrier sheds new light on the process of hot adatom motion. The adatoms are during the dissociation process initially closer than this barrier and thus their initial motion either along the surface or in a cannon-ball like trajectory will be accelerated by the electrostatic repulsion, possibly even aiding or affording a cannon-ball-like dissociation.

Further implications of our study for the understanding of hot adatom motion result

from the temperature independence of the pairing distances and distance ratio. An adatom separation measured at one temperature only[80] could still have been explained by a thermal motion during deposition. However, the same separations at ~40 % higher temperature as observed here can not be explained by a thermal motion in view of the exponential temperature dependence of a thermally induced random motion of adparticles. The distances found thus reflect the dissociation process at or close to the Ag(001) surface. Furthermore, the temperature-independent distance ratio excludes one of the two possibilities discussed before for the two pairing distances.[80] The different distances thus may not result from either a molecule dissociating upon approach or equilibrating as a molecule. The latter should be negligible at 200 K and in any case the ratio of these processes is expected to be temperature dependent. Indeed, an independent annealing experiment of molecules adsorbed at 100 K, which desorb from defect-free terrace sites already between 130 K and 160 K, supports this conclusion. A nonadiabatic quantum dynamical calculation[104] for oxygen dissociation over Al(111) provides is distributed equally between the two adatoms (initial energy $E_A = E_{dis}/2$), while in the other one the dissociation energy is predominantly transferred to one of the two adatoms ($E_B = E_{dis}$). As the diffusion distance of an adatom increases with its initial energy E as $\sim E^{1.6}$ this could explain the two different distances.[105] Such a scenario should not be restricted to Al(111), though the branching ratio will depend on the exact potential energy surface and thus differ on Ag(100).

A.5 Conclusion

We investigate terrace dissociation of oxygen on Ag(001) at 200 K and at coverages up to 1.7% ML. The results generalize earlier reports for dissociation at 140 K and coverages below 0.5% ML. Through comparison with random pairing simulations we reveal pairing distances of 2 nm (± 0.4 nm) and 4 nm (± 0.4 nm) with a ratio of 2:1. This observation sheds new light on the origin of the unusually large adatom distances found between the oxygen atoms after oxygen dissociation on Ag(001).



References

- [1] S. M. Gates, *The Journal of Physical Chemistry* **96**, 10439 (1992).
- [2] T. I. Kamins, G. A. D. Briggs, and R. S. Williams, *Applied Physics Letters* **73**, 1862 (1998).
- [3] J. M. Hartmann, V. Loup, G. Rolland, and M. N. Semeria, *Journal of Vacuum Science & Technology B: Microelectronics and Nanometer Structures* **21**, 2524 (2003).
- [4] H. Habuka, T. Suzuki, S. Yamamoto, A. Nakamura, T. Takeuchi, and M. Aihara, *Thin Solid Films* **489**, 104 (2005).
- [5] C. Isheden, P. E. Hellstrom, H. H. Radamson, S. L. Zhang, and M. Ostling, *Physica Scripta* **T114**, 107 (2004).
- [6] J. J. Boland, *Phys. Rev. Lett.* **65**, 3325 (1990).
- [7] A. Kubo, Y. Ishii, and M. Kitajima, *J. Chem. Phys.* **117**, 11336 (2002).
- [8] A. Kutana, B. Makarenko, and J. W. Rabalais, *J. Chem. Phys.* **119**, 11906 (2003).
- [9] I. Lyubinetsky, Z. Dohnálek, W. J. Choyke, and J. T. Yates, *Phys. Rev. B* **58**, 7950 (1998).
- [10] Z. F. Liu, and S. P. Chan, *Chem. Phys. Lett.* **318**, 15 (2000).
- [11] S.-S. Ferng, S.-T. Wu, D.-S. Lin, and T. C. Chiang, *J. Chem. Phys.* **130**, 164706 (2009).
- [12] M. McEllistrem, M. Allgeier, and J. J. Boland, *Science* **279**, 545 (1998).
- [13] I. R. McNab, and J. C. Polanyi, *Chem. Rev.* **106**, 4321 (2006).
- [14] J. Trost, T. Zambelli, J. Winterlin, and G. Ertl, *Phys. Rev. B* **54**, 17850 (1996).
- [15] J. G. Quattrucci, and B. Jackson, *J. Chem. Phys.* **122**, 074705 (2005).
- [16] C. T. Rettner, and D. J. Auerbach, *Phys. Rev. Lett.* **74**, 4551 (1995).
- [17] S. A. Buntin, *J. Chem. Phys.* **108**, 1601 (1998).
- [18] C. T. Rettner, *J. Chem. Phys.* **101**, 1529 (1994).
- [19] D. D. Koleske, S. M. Gates, and J. A. Schultz, *J. Chem. Phys.* **99**, 5619 (1993).
- [20] K. R. Lykke, and B. D. Kay, in *Laser Photoionization and Desorption Surface*

- Analysis Techniques (SPIE, Los Angeles, CA, USA, 1990), pp. 18.
- [21] B. Jackson, X. Sha, and Z. B. Guvenc, *J. Chem. Phys.* **116**, 2599 (2002).
- [22] C. M. Aldao, and J. H. Weaver, *Progress in Surface Science* **68**, 189 (2001).
- [23] C. C. Cheng, S. R. Lucas, H. Gutleben, W. J. Choyke, and J. T. Yates, *Journal of the American Chemical Society* **114**, 1249 (1992).
- [24] Y. H. Kim, J. Ree, and H. K. Shin, *J. Chem. Phys.* **108**, 9821 (1998).
- [25] K. Hattori, K. Shudo, M. Ueta, T. Iimori, and F. Komori, *Surf. Sci.* **402-404**, 170 (1998).
- [26] M.-W. Wu, S.-Y. Pan, W.-H. Hung, and D.-S. Lin, *Surf. Sci.* **507-510**, 295 (2002).
- [27] H. N. Waltenburg, and J. T. Yates, *Chemical Reviews* **95**, 1589 (1995).
- [28] Q. Gao, C. C. Cheng, P. J. Chen, W. J. Choyke, and J. T. Yates Jr, *Thin Solid Films* **225**, 140 (1993).
- [29] T.-C. Chiang, *Critical Reviews in Solid State and Materials Sciences* **14**, 269 (1988).
- [30] D. S. Lin, J. L. Wu, S. Y. Pan, and T. C. Chiang, *Phys. Rev. Lett.* **90**, 046102 (2003).
- [31] K.-i. Yamamoto, and M. Hasegawa, in *The 40th National Symposium of the American Vacuum Society (AVS, Orlando, Florida (USA), 1994)*, pp. 2493.
- [32] J. J. Boland, *Advances in Physics* **42**, 129 (1993).
- [33] G. J. Xu, K. S. Nakayama, B. R. Trenhaile, C. M. Aldao, and J. H. Weaver, *Phys. Rev. B* **67**, 125321 (2003).
- [34] B. R. Trenhaile, V. N. Antonov, G. J. Xu, A. Agrawal, A. W. Signor, R. E. Butera, K. S. Nakayama, and J. H. Weaver, *Phys. Rev. B* **73**, 125318 (2006).
- [35] J. H. G. Owen, D. R. Bowler, C. M. Goringe, K. Miki, and G. A. D. Briggs, *Phys. Rev. B* **54**, 14153 (1996).
- [36] A. Zangwill, *Physics at Surfaces* (Cambridge University Press, Cambridge, 1988).
- [37] G. Antczak, and G. Ehrlich, *Surf. Sci. Rep.* **62**, 39 (2007).
- [38] R. Gomer, *Rep. Prog. Phys.* **53**, 917 (1990).
- [39] G. L. Kellogg, *Surf. Sci. Rep.* **21**, 1 (1994).

- [40] K. N. Tu, J. W. Mayer, and L. C. Feldman, *Electronic Thin Film Science* (Macmillan Publishing Company, New York, 1992).
- [41] E. Bussmann, S. Bockenhauer, F. J. Himpsel, and B. S. Swartzentruber, *Phys. Rev. Lett.* **101**, 266101 (2008).
- [42] R. van Gastel, E. Somfai, S. B. van Albada, W. van Saarloos, and J. W. M. Frenken, *Phys. Rev. Lett.* **86**, 1562 (2001).
- [43] G. X. Cao, E. Nabighian, and X. D. Zhu, *Phys. Rev. Lett.* **79**, 3696 (1997).
- [44] T. R. Linderoth, S. Horch, E. Lægsgaard, I. Stensgaard, and F. Besenbacher, *Phys. Rev. Lett.* **78**, 4978 (1997).
- [45] K. C. Pandey, *Phys. Rev. Lett.* **57**, 2287 (1986).
- [46] J. Hafner, *Comput. Phys. Commun.* **177**, 6 (2007).
- [47] D. M. Ceperley, and B. J. Alder, *Phys. Rev. Lett.* **45**, 566 (1980).
- [48] J. P. Perdew, and A. Zunger, *Phys. Rev. B* **23**, 5048 (1981).
- [49] G. Mills, H. Jónsson, and G. K. Schenter, *Surf. Sci.* **324**, 305 (1995).
- [50] H. C. Flaum, D. J. D. Sullivan, and A. C. Kummel, *J. Phys. Chem.* **98**, 1719 (1994).
- [51] H. Neergaard Waltenburg, and J. T. Yates, *Chem. Rev.* **95**, 1589 (1995).
- [52] M. Dürr, and U. Höfer, *Surf. Sci. Rep.* **61**, 465 (2006).
- [53] M.-F. Hsieh, J.-Y. Chung, D.-S. Lin, and S.-F. Tsay, *J. Chem. Phys.* **127**, 034708 (2007).
- [54] S. Ovesson, A. Bogicevic, G. Wahnström, and B. I. Lundqvist, *Phys. Rev. B* **64**, 125423 (2001).
- [55] E. Hill, B. Freelon, and E. Ganz, *Phys. Rev. B* **60**, 15896 (1999).
- [56] G. J. Xu, A. W. Signor, A. Agrawal, K. S. Nakayama, B. R. Trenhaile, and J. H. Weaver, *Surf. Sci.* **577**, 77 (2005).
- [57] G. A. de Wijs, and A. Selloni, *Phys. Rev. Lett.* **77**, 881 (1996).
- [58] F. Ortmann, W. G. Schmidt, and F. Bechstedt, *Phys. Rev. Lett.* **95**, 186101 (2005).
- [59] J. D. Graham, and J. T. Roberts, *J. Chem. Phys.* **98**, 5974 (1994).

- [60] T.-C. Shen, C. Wang, G. C. Abeln, J. R. Tucker, J. W. Lyding, P. Avouris, and R. E. Walkup, *Science* **268**, 1590 (1995).
- [61] J. J. Boland, *Science* **262**, 1703 (1993).
- [62] G. A. Somorjai, *Introduction to Surface Chemistry and Catalysis* (John Wiley & Sons, New York, 1994), p. 667.
- [63] T. J. Rockey, M. Yang, and H.-L. Dai, *J. Phys. Chem. B* **110**, 19973 (2006).
- [64] I. Brihuega, A. Cano, M. M. Ugeda, J. J. Saenz, A. P. Levanyuk, and J. M. Gomez-Rodriguez, *Phys. Rev. Lett.* **98**, 156102 (2007).
- [65] L. Österlund, M. Pedersen, I. Stensgaard, E. Lægsgaard, and F. Besenbacher, *Phys. Rev. Lett.* **83**, 4812 (1999).
- [66] A. Bogicevic, S. Ovesson, P. Hyldgaard, B. I. Lundqvist, H. Brune, and D. R. Jennison, *Phys. Rev. Lett.* **85**, 1910 (2000).
- [67] P. Hyldgaard, and M. Persson, *J. Phys.: Condens. Matter* **12**, L13 (2000).
- [68] V. P. Zhdanov, *Langmuir* **17**, 1793 (2001).
- [69] J. G. E. Gardeniers, and L. J. Giling, *J. Cryst. Growth* **115**, 542 (1991).
- [70] A. Sánchez-Castillo, G. H. Coccoletzi, and N. Takeuchi, *Surf. Sci.* **521**, 95 (2002).
- [71] M. P. D'Evelyn, Y. L. Yang, and S. M. Cohen, *J. Chem. Phys.* **101**, 2463 (1994).
- [72] B. I. Craig, and P. V. Smith, *Surf. Sci.* **262**, 235 (1992).
- [73] Q. Gao, C. C. Cheng, P. J. Chen, W. J. Choyke, and J. T. Yates Jr, *Thin Solid Films* **225**, 140 (1993).
- [74] G. Wiatrowski, J. C. Le Bosse, J. Lopez, and I. Zasada, *Surf. Sci.* **265**, 229 (1992).
- [75] R. S. Nord, and J. W. Evans, *J. Chem. Phys.* **82**, 2795 (1985).
- [76] D. Chen, and J. J. Boland, *Phys. Rev. Lett.* **92**, 096103 (2004).
- [77] C. S. A. Fang, *Surf. Sci.* **235**, L291 (1990).
- [78] P. A. Grivil, D. M. Bird, and J. A. White, *Phys. Rev. Lett.* **77**, 3933 (1996).
- [79] F. B. de Mongeot, A. Cupolillo, U. Valbusa, and M. Rocca, *Chem. Phys. Lett.* **270**, 345 (1997).

- [80] S. Schintke, S. Messerli, K. Morgenstern, J. Nieminen, and W.-D. Schneider, *J. Chem. Phys.* **114**, 4206 (2001).
- [81] J. R. Hahn, and W. Ho, *J. Chem. Phys.* **123**, 214702 (2005).
- [82] M. Alducin, H. F. Busnengo, and R. D. Muino, *J. Chem. Phys.* **129**, 224702 (2008).
- [83] V. I. Bukhtiyarov, V. V. Kaichev, E. A. Podgornov, and I. P. Prosvirin, *Catal. Lett.* **57**, 233 (1999).
- [84] R. J. Beuhler, R. M. Rao, J. Hrbek, and M. G. White, *J. Phys. Chem. B* **105**, 5950 (2001).
- [85] G. Cipriani, D. Loffreda, A. Dal Corso, S. de Gironcoli, and S. Baroni, *Surf. Sci.* **501**, 182 (2002).
- [86] I. Costina, M. Schmid, H. Schiechl, M. Gajdos, A. Stierle, S. Kumaragurubaran, J. Hafner, H. Dosch, and P. Varga, *Surf. Sci.* **600**, 617 (2006).
- [87] L. A. Peyser, A. E. Vinson, A. P. Bartko, and R. M. Dickson, *Science* **291**, 103 (2001).
- [88] O. Citri, R. Baer, and R. Kosloff, *Surf. Sci.* **351**, 24 (1996).
- [89] M. Schmidt, A. Masson, and C. Brechignac, *Phys. Rev. Lett.* **91**, 243401 (2003).
- [90] S. Messerli, S. Schintke, K. Morgenstern, J. Nieminen, and W.-D. Schneider, *Chem. Phys. Lett.* **328**, 330 (2000).
- [91] M. Rocca, L. Savio, L. Vattuone, U. Burghaus, V. Palomba, N. Novelli, F. Buatier de Mongeot, U. Valbusa, R. Gunnella, G. Comelli, A. Baraldi, S. Lizzit, and G. Paolucci, *Phys. Rev. B* **61**, 213 (2000).
- [92] A. F. Carley, P. R. Davies, and M. W. Roberts, *Catal. Lett.* **80**, 25 (2002).
- [93] J. Wintterlin, R. Schuster, and G. Ertl, *Phys. Rev. Lett.* **77**, 123 (1996).
- [94] U. Diebold, W. Hebenstreit, G. Leonardelli, M. Schmid, and P. Varga, *Phys. Rev. Lett.* **81**, 405 (1998).
- [95] M. K. Rose, A. Borg, J. C. Dunphy, T. Mitsui, D. F. Ogletree, and M. Salmeron, *Surf. Sci.* **561**, 69 (2004).
- [96] T. Zambelli, J. V. Barth, J. Wintterlin, and G. Ertl, *Nature* **390**, 495 (1997).

- [97] C. R. Brundle, J. Behm, and J. A. Barker, *J. Vac. Sci. Technol. A* **2**, 1038 (1984).
- [98] M. Mehlhorn, H. Gawronski, L. Nedelmann, A. Grujic, and K. Morgenstern, *Rev. Sci. Instrum.* **78**, 033905 (2007).
- [99] K. Morgenstern, K.-F. Braun, and K.-H. Rieder, *Phys. Rev. Lett.* **89**, 226801 (2002).
- [100] M. Todorova, W. X. Li, M. V. Ganduglia-Pirovano, C. Stampfl, K. Reuter, and M. Scheffler, *Phys. Rev. Lett.* **89**, 096103 (2002).
- [101] L. Qi, X. Qian, and J. Li, *Phys. Rev. Lett.* **101**, 146101 (2008).
- [102] C. Q. Sun, *Applied Surf. Sci.* **246**, 6 (2005).
- [103] F. E. Olsson, N. Lorente, and M. Persson, *Surf. Sci.* **522**, L27 (2003).
- [104] G. Katz, R. Kosloff, and Y. Zeiri, *J. Chem. Phys.* **120**, 3931 (2004).
- [105] Y. Zeiri, *J. Chem. Phys.* **112**, 3408 (2000).



Curriculum vitae

謝明峰

Ming-Feng Hsieh

minfoon@gmail.com



■ NATIONALITY

- Taiwan (R.O.C.)

■ PERSONAL DETAILS

- Date of Birth: 20 June 1977.

■ SKILLS

- Ultra-High-Vacuum Scanning Tunneling Microscopy (UHV- STM)
- Ultra-High-Vacuum Atomic Force Microscopy (AFM)
- X-ray Photoelectron Spectroscopy (XPS)

■ EXPERIENCE

- Assistant researcher in the Photo Chemical Physics Laboratory in Institute of Atomic and Molecular Sciences Academia Sinica, Taipei, Taiwan (2001/05~2002/08).
- Research in surface science and interested in adsorbates/semiconductor system.
- Study synchrotron radiation research at National Synchrotron Radiation Research Center (SRRC).
- Semiconductor processing technology at National Nano Device laboratories (NDL).
- Operate Air AFM at Center for Nano Science & Technology.
- Exchange student in Leibniz University of Hannover, Germany (2007/09~2008/08).

■ EDUCATION

National Central University (NCU) 1896 Zhongli City
- undergraduate degree in department of physics
- 1995/09~1999/06

National Chiao Tung University (NCTU) Hsinchu City
- Master degree in institute of physics
- 2002/09~2004/06

National Chiao Tung University (NCTU) Hsinchu City
- Ph. D. degree in institute of physics
- 2004/09~2009/06

■ PUBLICATIONS LIST

1. M. F. Hsieh, J. Y. Chung, D. S. Lin, and S. F. Tsay, *Possibility of Direct Exchange Diffusion of Hydrogen on the Cl/Si(100)-2x1 Surface*, Phys. Rev. B **80**, 045804 (2009).
2. M. F. Hsieh, J. Y. Chung, D. S. Lin, and S. F. Tsay, *Correlation of Reaction Sites during the Chlorine Extraction by Hydrogen-atom from Cl/Si(100)-2x1*, J. Chem. Phys. **127**, 034708 (2007).
3. S. S. Ferng, T. H. Yang, Guangli Luo, K. M. Yang, M. F. Hsieh and D. S. Lin, Nanotechnology **17**, 5207 (2006).
4. S. S. Ferng, C. T. Lin, K. M. Yang, M. F. Hsieh, and D. S. Lin, Jpn. J. Appl. Phys. **45**, 2197 (2006).
5. K. M. Yang, J. Y. Chung, M. F. Hsieh, S. S. Ferng, D. S. Lin, and T. C. Chiang, Phys. Rev. B **74**, 193313 (2006).
6. 謝明峰, 林登松, 鑑別染色原理在掃描探針顯微技術上的應用, 科儀新知 **146**, 18-24 (2005).